Modelling the spatial ecology of cancer

Swansea University
Prifysgol Abertawe

Department of Mathematics
Swansea University
Amy Milne

Submitted to Swansea University in fulfilment of the requirements for the degree of
Doctor of Philosophy

2025

Abstract

A major disadvantage in molecularly targeted therapies for cancer is the development of de novo resistance. While much focus is on cell-based mechanisms, it is known that the microenvironment also plays a crucial role. Protected by microenvironmental mechanisms, disease persists during targeted therapy allowing for the accumulation of genetic and epigenetic modifications, eventually leading to permanent resistance and treatment failure. This thesis examines interactions between cancer cells and cancer associated fibroblasts (CAFs) to understand the local crosstalk facilitating residual disease driven by microenvironmental mechanisms, namely environmentally mediated drug resistance. Using a hybrid-discrete-continuum model, we explore how treatment-induced stress responses can elicit CAF responses and how breaks in treatment allow microenvironment normalisation as the stress response subsides. We investigate how fluctuating environmental conditions shape the local crosstalk and ultimately drive residual disease. Our experimentally calibrated model identifies environmental and treatment conditions that allow tumour eradication and those that enable survival. We find two very distinct mechanisms of resistance underpinning residual disease formed by environmental mechanisms. Finally, when we introduce cell-based mechanisms of resistance on top of environmental-driven mechanisms, we find that environmental conditions shape the phenotypic variation of residual and relapsing disease. This work provides a better understanding of the mechanisms that drive the creation of localised residual disease and disease relapse to molecularly targeted therapies.

Acknowledgements

I wish to express my deepest gratitude to my supervisor Dr. Noemi Picco for her unwavering patience, exceptional support, and dedicated mentorship during the past four years. Her guidance has been instrumental to the completion of this thesis.

I am sincerly thankful to Professor Gibin Powathil for his encouragement and valuable advice throughout my PhD. My thanks also extend to Professor Alexander Anderson for his valuable insight and guidance, and Professor Philip Maini whose expertise and knowledge proved invaluable to this research.

A special acknowledgement is due to Dr. Andriy Marusyk for generously providing the experimental data and for the engaging discussions on the underlying biology of targeted therapy for non-small cell lung cancer.

I am grateful to the Engineering and Physical Sciences Research Council (EPSRC) for fully funding my research and to all the staff and colleagues at Swansea University who provided support over the course of my doctoral studies.

Finally, to my wonderful family, thank you for your unconditional love, support and profound understanding of my unconventional ways. Your selflessness has been a constant source of strength. Last, but certainly not least, I thank my dog, Ruby, whose constant companionship, unwavering loyalty and many cuddles kept me grounded throughout this process.

Authorship Statement

Work undertaken as part of this thesis has been published [1]. This work is located in Chapters 4 - 6.

Milne, A., Marusyk, A., Maini, P.K., Anderson, A.R.A. & Picco, N. The role of environmentally mediated drug resistance in facilitating the spatial distribution of residual disease. *Commun Biol* **8(1)**, 1189 (2025).

Declarations and Statements

This work has not previously been accepted in substance for any degree and is not being concurrently submitted in candidature for any degree.

Signed .....[redacted].....

Date 15 / 02 / 2026

This thesis is the result of my own investigations, except where otherwise stated. Other sources are acknowledged by footnotes giving explicit references. A bibliography is appended.

Signed .....[redacted].....

Date 15 / 02 / 2026

I hereby give consent for my thesis, if accepted, to be available for electronic sharing

Signed .....[redacted].....

Date 15 / 02 / 2026

The University's ethical procedures have been followed and, where appropriate, that ethical approval has been granted.

Signed .....[redacted].....

Date 15 / 02 / 2026

Contents

List of Figures

List of Tables

List of Abbreviations

- ABC - Approximate Bayesian Computation
- ALK - anaplastic lymphoma kinase
- CAF - cancer associated fibroblast
- CML - chronic myeloid leukemia
- DNA - deoxyribonucleic acid
- DTP - drug-tolerant persister
- ECM - extracellular matrix
- EGFR - epidermal growth factor receptor
- EMDR - environmentally mediated drug resistance
- FTCS - forward time centred space
- HAL - Hybrid Automata Library
- HDC - hybrid-discrete-continuum
- HGF - hepatocyte growth factor
- KPP - Kolmogorov-Petrovsky-Piskunov
- MAPK - mitogen-activated protein kinase
- NSCLC - non-small cell lung cancer
- ODE - ordinary differential equation

- PDE - partial differential equation
- PPF - poor perfusion failure
- RTK - tyrosine kinase receptor
- TKI - tyrosine kinase inhibitor
- TME - tumour microenvironment

Chapter 1

Introduction

Cancer is a group of diseases characterised by uncontrolled proliferation driven by evolutionary processes [2]. It is incredibly difficult to treat successfully, and permanently cure due to its evolutionary nature. For each mode of therapy, cancer cells can evade eradication and eventually evolve resistance. Cancers ability to continually develop evasion and resistance mechanisms necessitates a coordinated multi-model and combination attack. Treatment plans are often personalised, including carefully considered combinations and timings of therapies, aimed at suppressing evasion and resistance mechanisms and prolonging the time to disease progression.

Molecularly targeted therapy is among the arsenal of treatments for cancer. These drugs act by inhibiting pathways that facilitate tumour growth and progression at the molecular level. Inhibitor targeted therapies are preferable to less tumour-specific cytotoxic chemotherapeutic agents because of their reduced toxicity due to the selective targeting of a specific mutation [3, 4, 5]. While initially molecularly targeted therapies offer good response, over time resistance develops and eventually treatment fails [5, 6]. Although our understanding of the mechanisms that drive resistance to targeted inhibitors is developing, how these mechanisms come together and facilitate disease progression *in-vivo* are not fully understood [4, 5, 7]. Cell-based mechanisms of resistance, whereby cancer cells undergo genetic and epigenetic changes that allow proliferation to

resume, can explain why treatment fails. However, they are only one facet of the complexity of drug resistance [8, 9].

Interactions between the tumour and the tumour microenvironment (TME) are implicated in the development of a type of resistance dependent on environmental conditions that we call environmentally mediated drug resistance (EMDR) [7, 8]. It is known that TME-secreted paracrine and juxtacrine factors can rescue otherwise drug-sensitive cancer cells [8, 10, 11]. Residual disease that occurs from EMDR creates conditions where in response to the selective pressure of therapy permanent cell-based resistance can develop.

In this thesis we aim to investigate interactions between the tumour and the TME that contribute to the emergence of drug resistance while undergoing molecularly targeted therapy using mathematical modelling. First, we discuss molecularly targeted therapies within the context of broader cancer treatment options. We explain how these therapies work, and how TME-mediated resistance can develop, providing necessary insights into the biological processes that will inform our mathematical modelling. Next, we review a selection of mathematical models that have been applied to cancer modelling, culminating in state-of-the-art hybrid modelling techniques.

We propose a hybrid-discrete-continuum (HDC) modelling framework to investigate how interactions at the cellular level affect tumour growth when undergoing treatment with a molecularly targeted drug. We present two models with different mechanisms of TME-mediated resistance and a third that includes cell-based mechanisms of resistance. The first of our models assumes a process of therapy-triggered activation as the mechanism that drives EMDR. In our second model EMDR is driven by a proximity-dependent mechanisms. In our third model we investigate how cell-based and TME-mediated mechanisms of resistance can come together to facilitate disease progression and treatment failure. We do this by introducing a phenotypic landscape for cancer cells. Movement in this landscape modulates how sensitive a cancer cell is to the effects of the drug. The parameters in our models are rigorously calibrated using *in-vitro* and *in-vivo* experimental data.

Using our first two models we explore the potential of harnessing the transient and reversible nature of drug-induced changes in the TME by introducing treatment holidays to reduce the incidence of EMDR. Furthermore, we investigate the resulting residual disease, characterising its spatial features at the tissue and cell scale. We identify distinct patterns of residual disease and show that local drug diffusion dynamics play a crucial rule in tumour-TME crosstalk. Our third model shows that therapy-driven selective pressures result in persistent drug-tolerant phenotypes and eventually disease resurgence as drug-resistant phenotypes emerge. We highlight the crucial role local drug diffusion dynamics play therapy-triggered phenotypic variation.

Modelling the emergence of resistance to molecularly targeted therapies is complex, involving interactions and dynamics that operate across different spatial and temporal scales. The spatial and temporal scales of cell-to-cell interactions and processes, drug diffusion and treatment scheduling all come together to modulate resistance. With our multiscale HDC models we capture and analyse how these different scales coalesce and form the residual disease that eventually leads to treatment failure.

Chapter 2

Background Biology

Cancer has been described as the group of diseases where driven by evolutionary processes, transformed cells undergo uncontrolled proliferation [2]. In multicellular organisms there are many cells that differ in form and function. For the organism to exist, survive and reproduce the cells must cooperate [12, 13]. The breakdown of this carefully orchestrated cooperation can result in aberrant cells that continue to proliferate to the detriment of the organism.

Although cancer is a disease of all multicellular organisms the pathogenesis of disease varies. For example, in plants uncontrolled proliferation of transformed cells occurs but is less likely than in animals. When tumours do form, they are contained by the immobile nature of plant cells and do not pose much of a threat to the individual plant [14].

In animals, cancer is common and can have much more devastating effects on the individual. There is a huge diversity of cancer disease in animals, some cancers form solid tumours that are capable of invasion and spread via metastasis and some, like blood cancers, do not form solid tumours but circulate throughout the organism as systemic disease. There are even rare directly transmissible cancers such as canine transmissible venereal tumour and devil facial tumour diseases [15]. The diversity of cancer as a disease reflects the abundant variety of both: cells with the potential to undergo tumourigenesis; and the ecological and evolutionary

pressures on animals as complex multicellular organisms.

2.1 Cancer therapies

Evidence of human cancer has been discovered in the remains of prehistoric fossils [16, 17] and, although not named as such, appears to be referred to in some of the earliest written texts [18]. The term cancer is the Latin translation of the Greek term καρκινος, that was used by Hippocrates to describe tumours he observed on the surface of the body. These early texts offered few options for treatment (cauterization and surgery - both treatments posing significant risks) and suggested palliative care as the best course of action [18, 19]. Technological and cultural barriers limited further progress in the understanding of cancer as a disease, and the development of treatments [19]. Over time these barriers have shifted as the body of knowledge increases, and therapeutic innovations provide gains in the fight against cancer disease.

2.1.1 Early developments

Surgery became a viable option in the middle of the nineteenth century due to the introduction of anaesthesiology and of antiseptic surgery. This prompted an explosion of surgeries attempting to cure cancers by removing solid tumours [19, 20]. Surgical removal of tumours provided relief from disease and in some cases full and extended remission. In others, despite increasingly extreme surgery, disease resurged and progressed. The reasons for this were not well understood. Although there was progress in surgical therapy, the types of cancer that could be treated and the success of those that could, was limited [20]. Surgery remains an important component of the cancer treatment arsenal; however it is only an option for solid, localised tumours in operable parts of the body.

Contemporaneously, experimentation with immunotherapy for cancer treatment began. Inspired by the association between tumour regression and infection with the bacterial strain *Streptococcus pyogenes*, physicians treated cancer patients by inoculation and achieved some success [21]. While some success was achieved, overall the treatment was not suitable due to the high toxicity associated with

the bacterial infection and interest in immunotherapy as a treatment for cancer dwindled [22].

The first uncontested use of radiation to treat cancer was by Victor Despeignes in 1896 [23, 24]. He treated an abdominal tumour and while the patient did not survive for long following the therapy, there was a 50% reduction in the size of the tumour. Other successful attempts to treat cancer using radiotherapy spurred further research to develop its use as a therapy for cancer [25, 26]. As with the development of surgery as a treatment for cancer, progress was made despite understanding the biology of cancer and was effective in treating localised solid tumours only. Cancer that does not form a solid tumour or has metastasized evaded both surgical and radiation therapeutic developments.

Systemic treatments were needed to treat systemic disease such as blood cancers and metastatic tumours. The term chemotherapy, meaning the treatment of disease via the use of chemicals, was coined by Paul Ehrlich. Ehrlich is credited with, among many things, the development of the first antibiotic used to treat syphilis and the concept of each disease having a *magic bullet* therapy. While he was not successful in discovering a *magic bullet* treatment for cancer, his ideas paved the way for future researchers to find success [19, 27].

Following the use of mustard gas as a weapon in the early twentieth century its effects on survivors were described by the Krumbhaars in 1919 [28]. They noted that white blood cells and bone marrow were depleted in those exposed. Their research inspired Louis Goodman and Alfred Gilman in 1942 to test the concept that a nitrogen mustard (mustard gas) could be utilised to treat lymphoma; a cancer where abnormal lymphocytes (a type of white blood cell) proliferate uncontrollably [29]. After successful animal studies an experiment was conducted treating a lymphoma patient with a nitrogen mustard. The treatment resulted in temporary remission [19, 27]. Their research was kept secret until it was published in 1946 [19]. Coincidently, following an air raid on Bari, Italy that occurred in 1943, one of the damaged ships released the mustard gas it was carrying. The depletion of white blood cells and bone marrow was noticed in those exposed and generated interest in investigating the possible uses of similar compounds to treat

cancer [19, 27].

Sidney Farber, a pathologist turned clinician, was working on discovering a chemotherapy to treat acute lymphoblastic leukemia (an aggressive blood cancer that afflicts mostly young people). Early experiments demonstrated that folic acid accelerated the production of white blood cells and progressed disease. This prompted Farber to search for an antagonist to folic acid that would halt the production of white blood cells [19, 30, 31]. An antagonist would be able to bind to the folic acid receptor but not activate it. In late 1947 one of Farber's patients treated with the folic acid antagonist Aminopterin went into remission. Although the remission was short lived, it was remarkable. This chemotherapy provided a treatment option for cancers that until then had none.

Advancements in the understanding of the immunology since 1945 sparked interest in its application to treating cancer again. Research into immune based therapies has been ongoing with particular success in the development of monoclonal antibodies, cancer vaccines and immune checkpoint anti-cancer therapies [22].

Necessity in treatment options for systemic cancer disease drove the development of chemotherapies. However, their use is not limited to only this type of cancer disease. The first successful chemotherapy used in a solid tumour is attributed to Jane Wright who developed methotrexate, another antifolate drug, in 1951 [32].

These early successes provided amazing and unprecedented remissions for patients with otherwise poor prognoses. Unfortunately, resistance and disease relapse remained a problem. However, the proof of concept, that cancers could be treated chemically, heralded a new era in cancer research. More drugs were developed, and combinations of surgery, radiotherapy and drugs were extensively tested [19, 27, 32, 33]. Some patients experienced full remissions, perhaps cures. For others, the increasingly invasive treatment protocols resulted in relapses with progressively more aggressive disease [19, 27].

The broad definition of chemotherapy, as the chemical treatment of disease, narrowed, becoming synonymous with cancer drug treatments. In particular, with cytotoxic drugs that not only affect cancer cells but also normal cells.

Nitrogen mustards work by damaging DNA by alkylation [34]. Aminopterin and methotrexate are enzyme inhibitors that cause a downstream inhibition of DNA replication [35]. The newer cytotoxic drug cisplatin binds with DNA, creating crosslinks that impair both DNA replication and repair, causing apoptosis (cell death) to be triggered [36]. Since these chemotherapies act on all dividing cells, they have very high levels of toxicity and result in severe side effects. There was a need for more precise therapies to be developed, ones that target cancer cells specifically, much as Ehrlich envisioned with his *magic bullet* [5, 19].

2.1.2 Molecularly targeted therapies

Discoveries in the biology of cancer provided new targets for drug development. Drugs that can specifically target the aberrant processes that result in uncontrolled proliferation and enhanced survival. These processes involve complex pathways of molecular signalling cascades that, in healthy cells, are tightly regulated to maintain tissue homeostasis, repair and reproduction. In cancer, oncogenes drive the aberrant activation of these pathways leading to the characteristic *hallmarks* of cancer [37].

In cells, kinases are enzymes that catalyse phosphorylation, triggering signalling cascades that regulate proliferation and apoptosis [38]. Once the kinase PI3K is activated, it catalyses the phosphorylation of PIP_2 into PIP_3 and leads to the binding of Akt to the cell membrane and triggers the subsequent downstream effects that lead to enhanced survival, increased proliferation and accelerated cell growth. Conversely, a phosphatase is an enzyme that catalyses dephosphorylation. PTEN is a phosphatase of PIP_3 that regulates the PI3K/Akt pathway [39]. Aberrant activation of the PI3K/Akt pathway, due to increased activation of PI3K or PTEN inhibition, is implicated in the development of many types of cancers [39, 40]. Hence, the PI3K/Akt pathway is an important target for therapy (Fig. 2.1).

Another important pathway that is a target for therapy is the MAPK/ERK cascade (Fig. 2.1). When a signalling molecule binds with a tyrosine kinase receptor (RTK) on the cell surface RAS becomes activated. When activated,

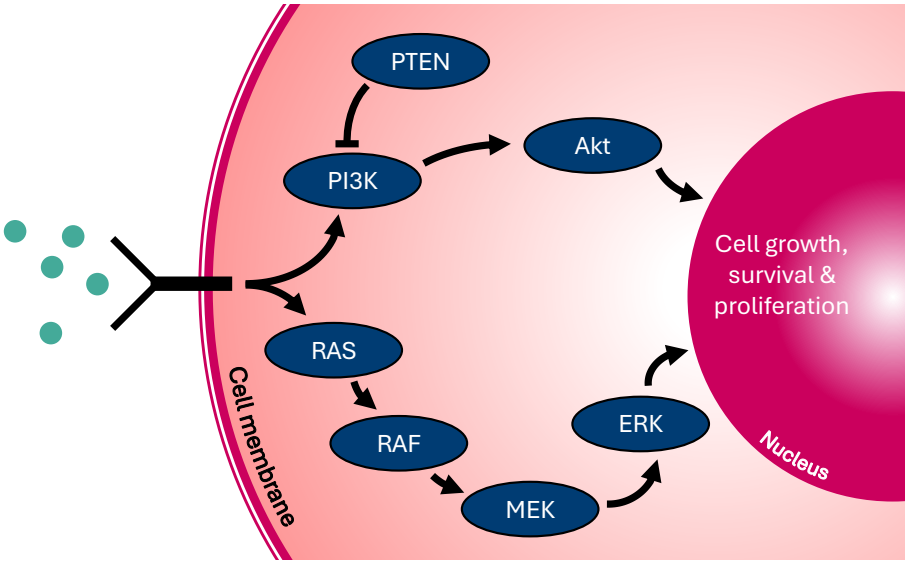

Figure 2.1: Key pathways associated with cancer. Two key pathways that result in cell growth, survival and proliferation are shown, the PI3K/Akt pathway and the MAPK pathway. Activated PI3K binds with Akt, through phosphorylation of PIP_2 into PIP_3, triggering downstream effects that enhance cell growth, survival and proliferation. PTEN regulates the PI3K/Akt pathway by dephosphorylation of PIP_3. Similarly activation of the MAPK pathway leads to enhanced cell growth, survival and proliferation. Activation at the cell membrane triggers the signalling cascade RAS $\rightarrow$ RAF $\rightarrow$ MEK $\rightarrow$ ERK. Uncontrolled proliferation, a defining characteristic of cancer, can result from aberrant activation of these pathways.

RAS activates the first kinase in the MAPK cascade, RAF (of which there are three known isoforms: ARAF, BRAF & CRAF [41, 42]). Activated RAF then phosphorylates MEK and MEK phosphorylates ERK, the final kinase in the MAPK cascade [43, 44, 45]. Downstream targets of ERK are involved with regulating many cell processes including cell growth, survival and proliferation [45]. More details regarding these and other signalling pathways involved in cancer development are available in this textbook [46].

Oncogenes are involved with the processes of uncontrolled cell growth, survival and proliferation, that are characteristic of cancer cells. The oncogene *neu* (now named HER-2), discovered in 1982, presented a possible target for therapy [47, 48]. HER-2 (*neu*) amplification results in accelerated cell growth and proliferation

via the constitutive activation of the PI3K/Akt pathway [49, 50]. Unlike other oncogenes known at the time, HER-2 is attached to the cell membrane and has a receptor. This presented an accessible target for drugs [19, 48].

The first purposely designed drug to target an oncogene, Trastuzumab, was developed to treat HER-2 positive breast cancer [5, 19]. Following a series of clinical trials, Trastuzumab, a monoclonal antibody that binds to HER-2 on the cell surface, was approved in 1998 [5, 51]. Typically, treatment initially provides relief followed by the development of resistance [49, 51].

Concurrently another class of targeted therapies, Tyrosine kinase inhibitors (TKIs), were in development. TKIs inhibit kinase function through different mechanisms [5, 52]. Imatinib was the first TKI to be approved in 2001 for the treatment of chronic myeloid leukemia (CML) [5]. It works by binding to the kinase domain of the tyrosine kinase oncoprotein BCR-ABL1 and reduces overall phosphorylation activity in the cytoplasm of the cell [53]. While Imatinib remains a very successful drug in managing CML, resistance and residual disease pose problems [54, 55, 56].

After the success of Imatinib many other TKIs were and continue to be developed that target different tyrosine kinases in different types of cancer. For example, epidermal growth factor receptor (EGFR) inhibitors for several different types of cancer including lung, breast and colon cancers; BRAF inhibitors for melanomas; and anaplastic lymphoma kinase (ALK) inhibitors for lung cancer [5]. As with the other treatments discussed, resistance is an issue. Resistance can be evident from the onset of treatment, whereby there is no response to the drug, or resistance can develop over the course of treatment.

2.2 Resistance to molecularly targeted therapies in solid tumours

Resistance to treatment is an overarching theme in all therapies for cancer disease, particularly for targeted therapies. How cancer resists therapy is complex and multifaceted, involving evolutionary and ecological processes.

Understanding this complexity is at the forefront of cancer research. Genetic and epigenetic mutations in cancer cells are the focus of many studies and are understood to be a large component of resistance. Another recognised component of resistance involves the interactions between the tumour and the TME [8, 11, 57].

2.2.1 The tumour microenvironment

Many types of cells (including fibroblasts, endothelial cells and immune cells), the extracellular matrix (ECM) and signalling molecules comprise the TME. In solid tumours interactions between the tumour and the TME can both inhibit [58, 59], or promote [60, 61, 62], tumour growth. Specifically, cancer associated fibroblasts (CAFs), as the main producer of ECM and signalling molecules, are implicated in resistance [7, 10, 57].

There is heterogeneity in both phenotype and function of CAF populations, the extent of which is an active field of research [63, 64]. There are CAF phenotypes that promote tumour growth and others that inhibit tumour growth [63]. CAF phenotypes are spatially clustered where some phenotypes are located proximal to cancer cells and others at locations further away from cancer cells [63, 64, 65, 66]. CAFs can experience morphological and functional changes in the presence of cancer and display phenotypic plasticity, where they can switch between phenotypes under specific conditions [67, 68]. Removal of the extracellular cues that drive these phenotypic changes has been shown to reverse them [66, 69, 70].

2.2.2 The role of the tumour microenvironment in resistance

Treatment with targeted therapies does not fully eradicate disease, some cancer cells survive treatment [7, 71, 72]. Environmental conditions can affect the interactions between the tumour and the TME and allow for cancer cells to persist, giving rise to EMDR. EMDR is transient in fluctuating environmental conditions [8]. The surviving cancer cells are referred to as drug-tolerant

persister cells (DTP) [73]. When treatment is stopped the DTPs begin to proliferate again and a disease flare is often observed [72, 74]. DTPs can develop permanent resistance that results in uncontrolled proliferation and treatment failure [8, 7].

Re-sensitisation to targeted therapies has been observed *in-vivo* following a break in treatment [72]. While properties of cancer cells have been shown to produce reversible resistance to targeted therapies [73, 74], they do not fully explain the development and complexity of the resistance observed [7, 71, 72]. Crucially, the location of residual disease in both *in-vitro* and *in-vivo* experiments of cancer cells undergoing targeted therapy is associated with locations with high stromal content [7, 10, 71].

The emergence of CAF-driven EMDR in response to molecularly targeted therapy has been observed experimentally [7, 10]. BRAF-mutant melanoma cells co-cultured with CAFs are treated with an BRAF inhibitor drug and ERK activity is monitored throughout the experiment [10]. Initially there is a decrease in ERK activity indicating a response to the drug. However, after 12 hours ERK activity resumed at levels commensurate with those prior to treatment. BRAF inhibition was effective in cultures of the same cell line without CAFs. Treatment is shown to affect CAF function, leading to ECM remodelling and elevated signalling that induces BRAF-independent ERK activation.

CAF-driven EMDR is observed in a series of *in-vitro* and *in-vivo* experiments of ALK positive non-small cell lung cancer (NSCLC) cells treated with an ALK inhibitor in a recent study by Desai *et al.* [7]. ALK positive NSCLC cells contain the fusion oncogene EML4-ALK [75, 76]. ALK is a RTK located on the cell surface that is directly activated by the oncogene EML4-ALK. Activated ALK in turn activates the downstream MAPK and STAT3/mTOR pathways [76]. While *in-vitro* experiments results of the study by Desai *et al.* confirmed that resistance is explained by the activation of cMET through CAF-secreted HGF (consistent with previous results [77]), the *in-vivo* results suggest more complexity is involved. The results show that disease persists proximal to stroma and that there are HGF-independent mechanisms at play. The study reveals that mechanisms of EMDR,

like cell-based mechanisms of resistance, are multifactorial and targeting these individually will not be sufficient to mitigate cancer cell survival and proliferation.

2.2.3 Treatment strategies for cell-intrinsic and acquired mechanisms of resistance

Populations of cancer cells that are resistant to a molecularly targeted therapy, whether they are present from the onset (intrinsic) or evolve during (acquired), present a significant impediment to treatment success. The processes by which a cancer cell develops resistance are not fully understood, however, evolutionary pressures are thought to play a role [46, 78].

Since the existence of resistant cancer cell populations is almost always inevitable, there has been considerable effort in developing evolutionary-guided therapies. These patient-specific therapies aim to control tumour burden, maintaining it at low levels, by exploiting the competition between sensitive and resistant cancer cell populations. This strategy relies on the fitness advantage sensitive cancer cells have in a drug-free environment over resistant cancer cells that have paid a cost for their resistance. The competition between sensitive and resistant cancer cell populations is modulated through drug composition, dosage and timing [79, 80, 81, 82].

Resistance is a common feature of all molecularly targeted therapies for cancer and presented a challenge since their inception. Strategies such as combining therapies, evolutionary-guided therapies, and optimal treatment scheduling have been investigated to delay the emergence of resistance and disease relapse. The results of these studies inform clinical treatment protocols [7, 32, 72, 83]. The evolving understanding of cancer biology and the development of ever more sophisticated and precise treatment strategies have had a major impact on survival and quality of life [33].

2.3 Discussion

In this chapter we provided a brief introduction to cancer and the development of treatments. We identified resistance as an ongoing barrier to treatment success for all therapy types. In this thesis we focus specifically on a solid tumour undergoing therapy with a generic molecularly targeted drug that is delivered via the bloodstream. Using mathematical modelling we will investigate the interactions between the tumour and its microenvironment in response to therapy and endeavour to make sense of the mechanisms that drive the emergence of resistance that leads to treatment failure. In Chapter 3 we describe mathematical modelling techniques used to model cancer.

Chapter 3

Background Mathematical Models

Mathematical models are used to describe biological systems, allowing for quantitative analysis of these complex systems. Examples include applying the Fibonacci series to describe population growth and structural composition [84, 85, 86, 87], geometric models and their variants for population growth [88, 89, 90, 91, 92], ordinary differential equations (ODEs) for pharmacokinetics/pharmacodynamics modelling [93, 94, 95], Lotka-Volterra equations for the interactions between species [96, 97, 98, 99, 100, 101, 102], and reaction-diffusion models for pattern formation (Turing patterns) [103, 104, 105, 106, 107].

In the context of cancer, an early investigation by Mayneord applied mathematical modelling to attempt to explain the *in-vivo* experimental observations of later stages of tumour growth that follow a linear relationship [108, 109]. He proposed that only cancer cells located on the periphery of the tumour could proliferate, that is the rate of change of the volume of a tumour is proportional to its surface area. Although the model captures the observed linear tumour growth dynamics, Mayneord points out that his model is only one of many that can do so [108]. An alternative model, presented by Laird, uses a Gompertz equation to capture the same phenomena [91, 109]. Another alternative, presented by Greenspan, explains limiting growth in later stages by the reduction of nutrient supply and waste disposal that is feasible through diffusion only [110].

Despite these early mathematical models capturing the dynamics of tumour growth, their scope is limited by the necessary simplification of the observed system, the small number of input parameters, and the homogenous nature of the model. In the first half of the twentieth century a full understanding of the underlying biological mechanisms and the capacity to collect large sets of quality experimental data was constrained by the available technology. Furthermore, implementing large mathematical models of complex biological systems was limited by the computational power available [111, 112, 113, 114].

Advances in technology have allowed for greater insight into the mechanisms of biological processes, the accumulation of large sophisticated experimental data, and increased processing capacity for computation and analysis. It is now feasible to implement and validate large multiscale mathematical models of complex biological systems. These models can be used for quantitative analysis, hypothesis testing, and prediction purposes [111, 112, 114, 115].

There is an overwhelming abundance of mathematical models in the literature that have been used for modelling cancer. We do not attempt to provide a complete review but rather a brief discussion of the development of modelling techniques, including examples, that are relevant to this thesis. More comprehensive reviews and further information on other modelling frameworks that are not directly discussed in this thesis are available in the literature [81, 115, 116, 117, 118, 119, 120, 121].

We start with deterministic modelling, where we consider models describing temporal dynamics from the simplest of models to large complex systems. We consider modelling techniques that do not include spatial features and those that do, both implicitly and explicitly. Next, we discuss stochastic models describing temporal dynamics, again we consider models that are not spatial explicit and those that are. We then consider a combination of deterministic and stochastic modelling techniques, in the form of hybrid modelling, that allows us to model complex biological systems at multiple scales.

3.1 Deterministic models

A deterministic model will always produce the same outcome for a given initial condition and parameter values. These models rely on a set of predefined mathematical equations or rules and input parameters and do not account for any variability. Deterministic models are often simple to implement and efficient to solve, either analytically or numerically, with the advantage of a large range of well-known analytical techniques. The choice of a deterministic model can be beneficial for systems with large well-mixed populations of individuals whereby random variations do not affect the dynamics of interest. Ordinary and partial differential equations are used for deterministic modelling. We will discuss each in the context of cancer.

3.1.1 Ordinary differential equations

ODEs are extensively used to model tumour growth, tumour heterogeneity, tumour-TME interactions and response to therapy [113, 122, 123, 124, 125, 126]. These equations have one independent variable, which for the systems relevant to this thesis, is time. The simplest model of tumour growth assumes exponential population growth. Consider the tumour volume, V, as a function of time, t, that is increasing at a constant rate, k, proportional to its current volume. We write the following ODE that governs this behaviour as:

$$\frac{dV}{dt} = kV. \tag{3.1}$$

The solution is $V(t) = V_0 e^{kt}$, where V_0 is the tumour volume at time $t = 0$. This model recapitulates constant unconstrained growth. While this behaviour is not consistent with experimental observations of later stages of tumour growth, when the tumour is subject to competition for space and other resources, it can be used to capture early tumour growth before these factors come into play [91, 127].

A variant is based on the extended exponential growth equation, first applied to modelling cancer by Mayneord [108]. It is given by the equation:

$$\frac{dV}{dt} = kV^r, \tag{3.2}$$

where $r = \frac{2}{3}$. With this model growth is assumed to be proportional to the surface area, i.e. growth on the periphery of the tumour. Introducing a death rate, d, that is proportional to the volume of the tumour, results in what is known as the von Bertalanffy growth model, that has the equation:

$$\frac{dV}{dt} = kV^{\frac{2}{3}} - dV. \tag{3.3}$$

Other extensions of the exponential growth equation that incorporate spatial and resource competition are the logistic and Gompertz models. Both models include a carrying capacity that the volume tends to asymptotically. These models can be used to model tumour growth where space and resource constraints are factors [91, 126, 127, 128, 129]. The logistic model has the equation:

$$\frac{dV}{dt} = kV(1 - \frac{V}{K}), \tag{3.4}$$

and the Gompertz model has the equation:

$$\frac{dV}{dt} = kV \ln(\frac{K}{V}). \tag{3.5}$$

Solutions to the exponential, extended exponential, von Bertalanffy, logistic and Gompertz models are shown in Figure 3.1**a**.

These models assume the tumour is comprised of a homogenous population of cancer cells that do not interact with the TME whereas, in fact, the heterogeneous populations of cancer cells in tumours are constantly interacting with the TME. Multi-compartment models can be used to describe the growth dynamics of tumours, incorporating intratumoural heterogeneity and tumour-TME crosstalk. The addition of a therapeutic drug compartment and the inclusion of a drug-induced death term in cancer cell compartments allow for the administration of therapy to be modelled within this framework. We

focus on only one example that is directly related to this thesis. Examples of other models can be found in these reviews [130, 131, 132].

A minimal ODE model is presented by Picco *et al.* [126] that describes the dynamics between two cancer cell compartments (sensitive and resistant) and two stroma compartments (fibroblasts and CAFs) while undergoing a combination of tumour and stroma targeted therapies. Both *in-vitro* and *in-vivo* experimental data is integrated into the model to quantify the contribution of the stroma (CAFs) to resistance in a tumour undergoing molecularly targeted therapy. Significant heterogeneity of TME-related properties is observed in the *in-vivo* experiments. This indicates the role of specific environmental factors in therapy resistance. Spatial constraints within the tissue, stromal support from the TME, or some combination of the two are proposed as possible explanations of the observed variation.

3.1.2 Partial differential equations

Although some of the models described above incorporate spatial features, they do so assuming spatial uniformity. An independent spatial variable can be introduced that allows for tumour growth dynamics to be modelled in space and time using partial differential equations (PDEs).

When space is introduced as an independent variable a PDE framework is required. Let a vector $\mathbf{x}$ define a location in a domain that is an open subset of an n-dimensional space ($n = 1, 2, 3$). We can then describe tumour cell density $u(\mathbf{x}, t)$ as a function of both space and time. The inclusion of the space variable in the PDE framework comes with additional computational cost compared with the ODE framework. Reaction-diffusion equations are extensively used to model tumour growth [133, 134, 135, 136, 137, 138]. One of the simplest and well known is the Fisher-KPP equation. This equation results from the addition of a diffusion term to the logistic equation (Eq. 3.4). The Fisher-KPP equation is given by:

$$\frac{\partial u}{\partial t} = D\nabla^2 u + kV(1 - \frac{V}{K}), \tag{3.6}$$

where D is the diffusion coefficient. The solution is a travelling wave with constant speed [139, 140, 141]. Equations of the Fisher-KPP type (i.e. those with travelling wave solutions) can capture the dynamics of a population diffusing as it grows. Fisher-KPP type and other PDE equations have been extensively applied to modelling tumour growth, heterogeneity, interactions with the TME and resistance to therapy [133, 135, 137, 138, 142, 143, 144, 145, 146, 147, 148].

We discuss a particular example that examines the role of the TME in tumour growth and invasion by Martin *et al.* [147]. Competitive and cooperative interactions between tumour and stroma cells are incorporated into an earlier acid-invasion model [135]. Interactions at the tumour-TME boundary are explored and the model predicts a nonlinear relationship between acidity and invasion. While these results are counterintuitive (i.e. a more aggressive tumour is less invasive), the model can capture the phenomena of encapsulated tumours. Tumour acidity regulation is suggested as a possible treatment strategy.

The models discussed in this section are deterministic and do not allow for the inherent randomness that features in biological systems. In the next section we discuss stochastic models that incorporate random variation into the modelling process.

3.2 Stochastic models

Biological systems, of which tumours and their TME are an example, are innately random. Deterministic models can capture the behaviour of these systems, but they do not account for this inherent randomness that, in certain scenarios, can significantly affect outcomes. Each realisation of a stochastic model can produce a different output for a given initial condition. Within this modelling framework, many realisations for each given initial condition are required to build a probability distribution output, considerably increasing the computation cost when compared to deterministic modelling.

The vast majority of stochastic models of tumour growth, tumour heterogeneity,

tumour-TME interactions and response to therapy involve systems of individual agents (cells) evolving through time. Agents can be assigned a species (i.e. cell type, state, or phenotype) and their behaviour is determined by a stochastic process defined on a probability space. Many different types of stochastic processes exist and are used to model tumour-TME interactions. In the following sections we will discuss Markov chain models only, stochastic processes where the next state in a system depends only on the state that it is currently in. A variety of algorithms are used to simulate stochastic processes including exact approaches based on Poisson processes, such as the Gillespie algorithm, or approximate procedures that use discrete time increments (Fig. 3.1**b - f**) [149, 150, 151].

3.2.1 Non-spatial and spatially implicit birth-death models

In simple stochastic models, spatial interactions between individuals are either ignored (non-spatial) or are applied globally to some or all individuals (spatially implicit). Branching processes are stochastic processes that are used to model population dynamics. Each time increment the individuals can reproduce according to a defined probability distribution. An early example of a non-spatial branching process model is the birth-death process [152]. It was introduced to capture Lotka-Volterra population dynamics using a stochastic model. To do this, the Kolmogorov forward equations (master equations) are derived from the birth and death processes and explicitly solved. There is agreement between these solutions and the solutions of the deterministic Lotka-Volterra model [153].

Although, in this work, the birth-death process is not applied to tumour growth, it did provide the foundations for modelling cancer. An example of an early model in the context of cancer is a spatially implicit version of a birth-death process with proliferation constrained to the tumour periphery, while death can occur throughout the tumour (i.e. capturing the same dynamics as the von Bertalanffy model, see Fig. 3.1**d**) [154]. These early branching process models are concerned with simple systems of tumour growth. With greater understanding of underlying biological mechanisms and the

increase in availability of experimental data, branching process models are used to model systems with more complexity. They are used extensively to model tumour initiation and growth, tumour heterogeneity and evolution, tumour-TME interactions, and response to therapy [154, 155, 156, 157, 158, 159, 160, 161, 162, 163].

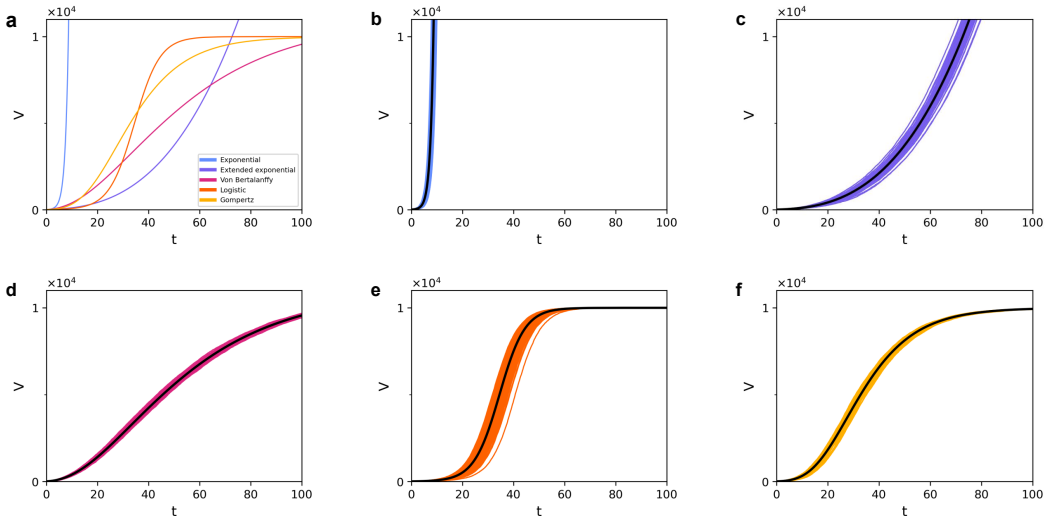

Figure 3.1: Deterministic and stochastic models of tumour growth. a: ODE solutions for five different models of tumour growth for $t \in [0, 100]$. Exponential ($\frac{dV}{dt} = 0.8V$), extended exponential ($\frac{dV}{dt} = 0.8V^{\frac{2}{3}}$), von Bertalanffy ($\frac{dV}{dt} = 2V^{\frac{2}{3}} - 0.09V$), logistic ($\frac{dV}{dt} = 0.2V(1 - \frac{V}{10^4})$) and Gompertz ($\frac{dV}{dt} = 0.07V\ln(\frac{10^4}{V})$). **b:** ODE solution (*black*) is compared to stochastic solutions (*blue*) for the exponential model. **c:** ODE solution (*black*) is compared to stochastic solutions (*purple*) for the extended exponential model. **d:** ODE solution (*black*) is compared to stochastic solutions (*pink*) for the von Bertalanffy model. **e:** ODE solution (*black*) is compared to stochastic solutions (*orange*) for the logistic model. **f:** ODE solution (*black*) is compared to stochastic solutions (*yellow*) for the Gompertz model. Stochastic results are of 100 realisations of the stochastic model using a τ-leaping algorithm ($\tau = 0.02$).

3.2.2 Spatially explicit agent-based models

Spatially explicit stochastic models include information of the location of each individual agent on the domain, allowing for heterogeneous local conditions. Interactions at the cellular scale can reveal patterns at the domain level that are not possible in non-spatial or spatially implicit stochastic models where a

well-mixed homogeneous population is assumed. An early example of a spatially explicit stochastic model uses a cellular automaton to model tumour growth and interactions with the immune system, capturing Gompertzian growth dynamics [164]. Cellular automaton models have been used more recently to describe tumour growth and heterogeneity [165, 166, 167, 168, 169, 170].

A 2D cellular automaton model is used to investigate the development of resistance to targeted therapy under continuous and adaptive therapy strategies, with and without CAFs [166]. Using different spatial configurations of sensitive and resistant cells this model reveals that the advantages of adaptive therapy regimes can be limited by local competition that is determined by spatial factors. CAFs are introduced into the model by occupying a set area of the lattice, the effect of their position relative to the resistant cancer cell population is explored using five different cases. The tumour dynamics in each of the cases is compared to a case without CAFs. The results suggest that the positioning of CAFs relative to the resistant cancer cells can impact cancer cell growth and the onset of drug resistance. Spatial competition between resistant cancer cells limits the CAF driven benefits when the resistant cancer cell population and CAFs are co-located. CAFs that are co-located with sensitive cancer cells provide a beneficial niche for resistant cancer cells to proliferate into as the sensitive cancer cells die during therapy. This study highlights the importance of including spatial features when modelling a tumours response to therapy.

Another model used for modelling cancer is the Eden growth model [171]. These spatially explicit stochastic models describe proliferation on the periphery of the tumour. A 3D Eden growth model is used to model tumour evolution and resistance to therapy [172]. Intratumour heterogeneity is explained by cell turnover and dispersion, and selective advantage is shown to result in a selective sweep that can account for the development of resistance in treated tumours. Another application of an Eden growth model is a 2D version used to investigate the relationship between spatially dependent growth dynamics and genetic patterns [173].

Spatially explicit Moran processes are used to model tumour heterogeneity and

evolution. Moran models assume a constant population of individual agents and are mainly used to model evolutionary dynamics [116]. They can be used exclusively when growth dynamics are ignored, or as a component of a multiscale model that includes growth [174, 175, 176, 177, 178, 179].

The intrinsically random nature of biological systems is well captured by stochastic models. However, these models are computationally more expensive than their deterministic counterparts. Many techniques have been developed to produce deterministic approximations of stochastic processes, reducing computational complexity while still capturing the dynamics of interest [180, 181, 182, 183, 184, 185, 186, 187, 188, 189, 190, 191, 192, 193]. Another class of model has been developed that integrates both stochastic and deterministic modelling principles. This hybrid modelling framework allows for complex biological systems to be described at multiple scales.

3.3 Hybrid models

The term hybrid model can be applied to a variety of different complex modelling techniques [119, 194]. In this thesis we are interested in the HDC modelling framework introduced by Anderson *et al.* [195]. It was first used to model nematode movement and chemotaxis; however, it is predominantly known for the study by Anderson and Chaplain where it is applied to modelling tumour-induced angiogenesis [196]. This technique allows for biological systems to be modelled at different scales. For example, the stochastic dynamics of individual agents (cells) interact with continuous fields of molecular scale dynamics (concentrations of growth factors or drugs). Anderson and Chaplain model the dynamics of endothelial cell migration during angiogenesis using both deterministic and hybrid modelling. The hybrid modelling technique couples stochastic dynamics of individual agents (the endothelial cells) with continuous processes, including diffusion, chemotaxis (in response to gradients of tumour angiogenic factors), and haptotaxis (in response to fibronectin gradients) [196]. This technique is used extensively in modelling tumour growth, migration, heterogeneity and evolution and response to therapy

[196, 197, 198, 199, 200, 201, 202, 203, 204, 205, 206]. The modelling framework has been the subject of many reviews that provide further information on the applications and variants [111, 112, 114, 115, 130, 194, 207, 208, 209].

Recently, the role of EMDR in the emergence of resistance to targeted therapies has been explored using an experimentally parametrised, HDC model of multiple myeloma (a blood cancer located in the bone marrow) [206]. In normal conditions, the model captures bone homeostasis through trabecular bone remodelling (a process responsible for the maintenance of trabecular bone). A single cancer cell is introduced into the system near a bone remodelling site. This cancer cell recruits the stroma (specifically, osteoclasts) that can promote cancer cell survival and growth by releasing stored cytokines through destruction of the bone matrix. Once treated with a targeted therapy, tumour burden is significantly reduced. When no EMDR effects are considered, the tumour is eradicated. Only small, stable residual populations of cancer cells persist when EMDR effects are considered, suggesting the disease resurgence observed in *in-vivo* experimental data cannot be explained by EMDR only. A resistant cancer cell type is integrated into the model. At cell division, new cells have a probability of developing resistance. The number of times resistance is initiated is tracked for three scenarios, no treatment, treatment without EMDR effects, and treatment with EMDR effects. When EMDR effects are included, resistance is initiated more times, resulting in greater intratumoural heterogeneity. These results indicate the importance of considering the TME when modelling response to treatment and the development of drug resistance.

3.4 Discussion

A large diversity of mathematical models exists that have been used in cancer modelling. We did not attempt to cover all these techniques but chose to discuss models that contribute to the development of the HDC modelling technique that is the focus of this thesis. We started with simple ODE models that describe the temporal evolution of cancer systems. While spatial attributes can be embedded into these models, this is done at a global level, assuming the

system domain is homogeneous and well-mixed. Next, we discussed spatially explicit deterministic models that use a PDE framework. This framework allows for the spatial-temporal modelling of cancer systems. A drawback of deterministic models is that they do not allow for any stochasticity within the system. Given the random nature of biological systems, stochastic modelling techniques can be a more appropriate choice. We discussed non-spatial and spatially implicit stochastic models followed by spatially explicit models. Although stochastic modelling techniques allow for the inclusion of randomness, interactions within the system are restricted to one scale. Underlying biological processes that drive Tumour-TME interactions operate at different spatial and temporal scales. With the HDC modelling framework, that combines deterministic and stochastic modelling techniques, complex biological systems can be modelled at multiple scales, allowing us to capture and analyse how these scales come together to modulate the system.

We discussed three examples of models that investigate tumour-stroma interactions and the role they play in EMDR to molecularly targeted therapies. The first was the experimentally calibrated ODE model of EMDR in response to targeted therapy [126]. This minimal model could not capture the heterogeneous *in-vivo* experimental results. The heterogeneity is attributed to specific TME properties factoring into the response to treatment, highlighting the need for spatial attributes to be included when modelling the emergence of EMDR to targeted therapies. Two spatial models of EMDR, in response to targeted therapy, were then discussed [166, 206]. Both models demonstrate that local microenvironmental conditions drive treatment response and the emergence of resistance. The first of these models was a 2D cellular automata that does not attempt to model the TME but rather investigate a much-simplified system as a proof of concept. The second model, however, builds the TME starting with a biologically parameterised model of the bone microenvironment in normal conditions, followed by tumour initiation (metastatic event), growth, and interaction with the TME. A targeted therapy is introduced that directly affects the cells and does not include any drug diffusion dynamics. In both these models, cancer cells are either sensitive or

resistant to the therapy despite experimental data suggesting that resistance, to targeted therapies, occurs gradually along a resistance continuum [72, 210, 211].

In the Chapter 4 we present a HDC model for the emergence of EMDR in a solid tumour treated with a molecularly targeted drug. Our biologically parameterised model captures tumour growth within a vascularised heterogeneous tissue and the emergence of EMDR once treatment commences. Our model incorporates drug diffusion dynamics from the vasculature. While we initially focus on the emergence of EMDR and neglect cell-based mechanisms of resistance, later in Chapter 8 we present a variant of the model that incorporates these mechanisms of resistance that act along a continuum.

Chapter 4

A Model of Stroma Activation-Driven Environmentally Mediated Drug Resistance

We model the temporal and spatial dynamics of a solid tumour growing in a pre-existing homeostatic non-cancerous tissue and responding to therapy with a generic inhibitor drug that is delivered via the tissue's vascular system. The aberrant activation of some signalling pathways in tumour progression and how inhibitor drugs target these at a molecular level is discussed in Section 2.1.2. We adopt a HDC model to describe the stochastic dynamics of cells acting as individual agents, coupled with the reaction-diffusion dynamics of drug and concentrations of signalling molecules that mediate EMDR (Fig. 4.1). Most of the material in this chapter is based on the work undertaken for this thesis that has been published [1].

Central to our model is the *proliferation signal* which represents the local net accumulation of pro-growth versus pro-apoptotic molecular signalling within the tissue [7]. A cancer cell will determine its viability and proliferative status dependent on the local *proliferation signal* intensity it senses.

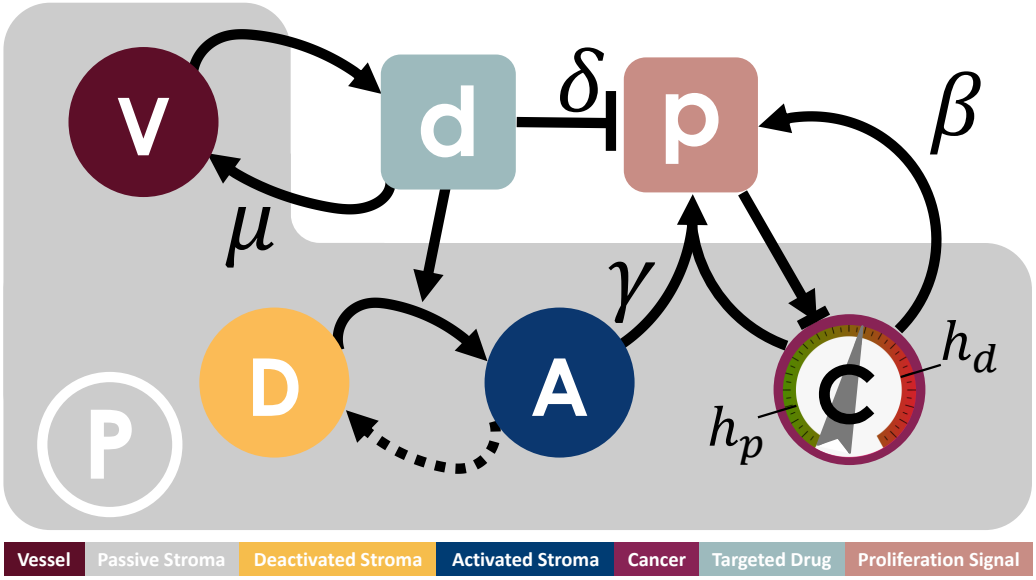

Figure 4.1: Key interactions between cancer cells and the TME assumed in the model. Cancer cell, C, behaviour is dependent on the local concentration of the *proliferation signal*, p, with thresholds for death, h_d, and proliferation, h_p. Cancer cells provide autocrine promotion of local *proliferation signal* at rate β. TME comprises both passive, P, and reactive stroma. Reactive stroma can be in either an activated, A, or deactivated, D, state. A targeted inhibitor drug, d, depletes *proliferation signal* at rate δ and is removed from the system through vessel sites V at rate μ. Local concentration of targeted drug above threshold h_r triggers activation of reactive stroma cells adjacent to a cancer cell, in turn providing paracrine promotion of the *proliferation signal* at rate γ. Activated reactive stroma reverts to a deactivated state if the drug concentration falls below h_r.

The *proliferation signal* is modulated by the cancer cells, the inhibitor drug, and subsets of non-cancer cells in the TME that can engage in crosstalk with the cancer cells. In our model we refer to all non-cancer cells in the TME as stroma. We consider a simple case of the model with only one subset of stroma population that engages in crosstalk with the cancer cells. We designate this subset, that through cell-to-cell contact can interact with the cancer cells, as reactive. The experimental counterpart of these cells are CAFs that display some level of differentiation when drug-naive, and a rescue capability to cancer cells in close proximity upon delivery of the drug [10]. The remaining stroma can be

partitioned further to represent other cell types that interact with cancer cells, but in our representation is classed as one cell type: passive stroma.

We introduce a generic inhibitor drug that is delivered through the blood circulatory system, diffuses through the tissue, and targets a key driver mutation in the cancer cells. The inhibitor drug inhibits pro-growth signalling and enhances pro-apoptotic signalling, ultimately reducing the viability of cancer cells. Although targeted therapies act specifically on cancer cells and do not directly affect CAFs, their activation reflects therapy-triggered wound/stress response from tumour cells. We assume that reactive stroma in cell-to-cell contact with cancer is activated by high local drug concentration that triggers the stress response.

We assume highest levels of crosstalk at the tumour-stroma interface since ECM and uptake by local cancer cells physically limits the diffusion of signalling molecules. Reactive stroma that become activated can rescue cancer cells by returning them to a viable, proliferative state through paracrine production of the *proliferation signal*.

While definite evidence of TME renormalisation after the cessation of treatment is lacking, *in-vivo* and clinical studies show a renewed response upon re-administration of TKI therapies [72, 74, 212, 213]. These data suggest that normalisation of the TME following the cessation of inhibitor drug delivery as a possible explanation for re-sensitisation. Normalisation of the TME allows for further response when treatment is reintroduced. Furthermore, CAFs have been shown to display phenotypic plasticity in response to extracellular cues [66, 67, 68, 69, 70]. Therefore, in the model, we assume activation of reactive stroma is transient and contingent on therapy-triggered recruitment cues from cancer cells.

We initially adopt this simplest description of tumour-stroma crosstalk requiring contact-mediated activation and drug-dependent deactivation. In Appendix A we explore the effect of non-contact-mediated crosstalk and alternative deactivation mechanisms.

4.1 Model definition

We choose to adopt a HDC modelling framework. We consider a rectangular two-dimensional cross-section of tissue that mimics a slice of a tumour. There are a variety of histological techniques performed on clinical biopsy slices that reveal the tissue structure at a microscopic level and allows for the classification of cells and cell function [214]. We model this cross-section with a square lattice, Ω. The domain, Ω, contains discrete agents representing the cells in a cross-section of tissue. In the model we have three sets of agents: blood vessels, stroma and cancer cells. The spatial configuration of the cells on Ω can be compared to histological data [215].

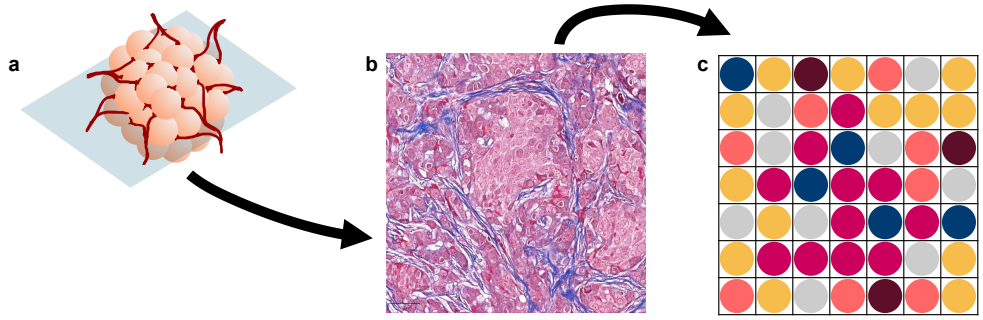

Figure 4.2: Capturing tumour spatial heterogeneity. a: A 2D cross sectional slice of a 3D vascularised tumour is taken. Note that we make the simplifying assumption that vasculature runs perpendicularly. **b:** Tumour spatial heterogeneity is characterised using histopathology techniques on the 2D slice. Example is a trichrome stain sample from a xenograft model of NSCLC (cell line - H3122) treated with *alectinib* for 3 weeks. Image courtesy of the Marusyk laboratory, Moffitt Cancer Center, Tampa. **c:** The information on tumour spatial heterogeneity can be transformed and cells placed on the lattice in a simplified yet representative configuration. This technique captures tumour spatial heterogeneity and allows for *in-silico* hypothesis testing and experimentation.

The individual agents comprise the stochastic component of the model. We model the molecular scale dynamics of the *proliferation signal* and the inhibitor drug with the deterministic component of the model. We let $p(\mathbf{x}, t)$ be the

proliferation signal and $d(\mathbf{x}, t)$ be the inhibitor drug concentration. Both p and d are continuous functions of space, $\mathbf{x}$, and time, t and are governed by PDEs, whose formulation depends on the agents in Ω.

In order to investigate the dynamics of resistance that can be attributed to immediate crosstalk between cancer and stroma cells, we assume that cells do not actively move within the domain but do spread through proliferation (in Appendix B a model variant with cancer cell movement is discussed). Each cancer and stroma cell advances through the cell cycle, divides, dies and updates their state according to the cell type specific rules and context dependent conditions (i.e. TME-dependent) described in later sections. Cancer and stroma cells have an intermitotic time, $I > 0$, and each cell is equipped with an internal clock to track its progress through the cell cycle. If there is sufficient space surrounding the dividing cell (i.e. at least one empty position in its Moore neighbourhood), division occurs. Two daughter cells are produced when a cell divides. One of the daughter cells occupies the mother's position and the other daughter cell is randomly placed in one of the empty locations in the Moore neighbourhood of the mother cell.

The concentrations of p and d are then updated according to the current configuration of the agents in Ω. Zero-flux Neumann boundary conditions, on the boundary of Ω, are imposed. A forward difference scheme in time and a second order central difference scheme in space approximation (FTCS) is used to numerically solve the PDEs and update the concentrations of p and d (details of the numerical schemes are described in Section 4.2). To comply with stability requirements of the numerical scheme we solve the equation for d on a finer timescale than that of the cells (Section 4.2 for details).

4.1.1 Blood vessels and drug concentration

A cross-section of tissue would realistically cut through a more intricate vasculature network and the resulting blood vessel positions on Ω would be comprised of more than one lattice position [216]. However, here we make the simplifying assumption that blood vessels cut the plane of Ω perpendicularly

and occupy a single lattice position. Vascular cells act as a point source and sink for the inhibitor drug. Vascular remodelling and degradation are neglected, and blood vessels are static and constant as the model describes tumour growth prior to angiogenesis. While these are simplifying assumptions, they still allow us to describe realistic drug diffusion dynamics in the tissue.

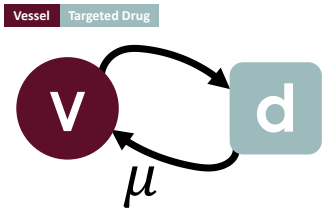

Figure 4.3: Vessel locations and the targeted drug. The drug enters Ω and re-enters the bloodstream at rate μ at the vessels.

We define $\mathcal{V}$ to be the set of vessel locations, that is $\mathbf{x} \in \mathcal{V}$ if there is a vessel at position $\mathbf{x}$. We determine $\mathcal{V}$ using the circle packing algorithm, first introduced in [217]. This algorithm uses *in-vivo* measurements for the average distance between vessels, σ_{mean}, to calculate the number of vessels in the domain, denoted by N_v [218]. We have:

$$N_v = \frac{|\,\Omega\,|}{{\sigma_{mean}}^2}, \tag{4.1}$$

where $|\,\Omega\,|$ is the area of the domain. The algorithm places the blood vessels in the domain respecting the experimentally measured minimum distance between vessels, σ_{min}. We provide an outline of the algorithm here.

Circle packing algorithm

Create a list, $\bar{\Omega}$, containing every lattice position in Ω.

For $i = 1, \ldots, N_v$:

1. Sample $\mathbf{v}_i$ from the list $\bar{\Omega}$ of lattice positions, and place a blood vessel cell at this position.
2. From the list $\bar{\Omega}$, remove the lattice positions, $\hat{\mathbf{x}} \in \bar{\Omega}$, such that $\|\hat{\mathbf{x}} - \mathbf{v}_i\| < \sigma_{min}$.

Vessel cells are the point sources for the inhibitor drug to enter the domain. The drug enters and diffuses into Ω while an amount is cleared from Ω at vessel sites representing flow back into the bloodstream (Fig. 4.3). The following PDE

describes the behaviour of the drug concentration, $d(\mathbf{x}, t)$, in Ω:

$$\frac{\partial d}{\partial t} = \overbrace{D_d \nabla^2 d}^{\text{diffusion}} - \overbrace{\mu v(\mathbf{x}, t) d}^{\text{clearance}}. \tag{4.2}$$

D_d is the diffusion coefficient; μ is the rate of drug clearance; $v(\mathbf{x}, t)$ is the binary function indicating the presence/absence of a vessel site at position $\mathbf{x}$ at time t:

$$v(\mathbf{x}, t) = \begin{cases} 1 & \text{if } \mathbf{x} \in \mathcal{V}, \\ 0 & \text{otherwise.} \end{cases} \tag{4.3}$$

To mimic drug delivery we impose maximal drug concentration at vessel sites, that is, we let $d(\mathbf{x}, t) = 1$ for $\mathbf{x} \in \mathcal{V}$ if the drug is being delivered at time t. Note that with this set up vessel sites act as boundaries of Ω with Dirichlet boundary conditions while the drug is administered, and Neumann boundary conditions otherwise. $d \in [0, 1]$.

4.1.2 Stroma cells

We classify stroma cells as either reactive or passive. We define reactive stroma cells that can engage in crosstalk with cancer cells through signalling cues and passive stroma as all the stroma cells that do not directly interact with cancer cells (Fig. 4.1 P). We initiate stroma cells randomly as either cell type according to a fixed proportion $\pi \in [0, 1]$, where $\pi = 0$ corresponds to all the stroma being passive and $\pi = 1$ corresponds to all the stroma being reactive. Reactive stroma cells can exist in either deactivated or activated state (Fig. 4.1 D and A, respectively).

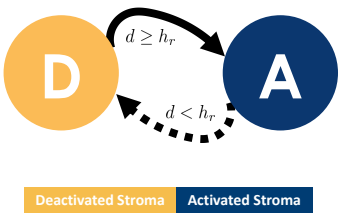

Figure 4.4: Activation and deactivation of reactive stroma. Deactivated stroma will become activated if the local drug concentration reaches the threshold for activation (and the proximal cancer cell condition is also satisfied). If the local drug concentration reduces below the threshold for activation the activated stroma will deactivate.

Specific environmental conditions allow reactive stroma to transition between these states. A deactivated cell can become activated, with probability p_A, in response to recruitment cues cancer cells emit. This transition depends on two conditions: the local concentration of the inhibitor drug being above a threshold $h_r \in [0, 1]$ (sufficiently high drug concentration to trigger stress signalling in the cancer cell); and the reactive stroma cell being proximal (i.e. in the Moore neighbourhood) to a cancer cell to receive the signal for recruitment. We assume that as long as the local drug concentration is at or above h_r a reactive stroma cell will remain in an activated state, otherwise, it will transition into a deactivated state (Fig 4.4). Alternative deactivation conditions were investigated and little change in the resulting dynamics of interest was discovered, we show these results in Appendix A.

We allow natural turnover of stroma, through death and birth processes, to recapitulate homeostatic tissue growth. Stroma cell death occurs with probability p_T. We choose p_T to be one order of magnitude smaller than p_A since we assume that the timescale of stromal activation is quicker than that of stroma turnover (Table 5.1). To capture tissue homeostasis, in contrast to the uncontrolled proliferation of cancer cells, stroma cell division is subject to contact inhibition [37]. We model this effect by introducing the parameter $n_{CI} \in \mathbb{N}$. If there are more than n_{CI} neighbours in the neighbourhood of a stroma cell, cell division is aborted. Daughter cells are the same cell type (passive or reactive) and state (activated or deactivated) as the mother cells. The stroma maintains a dynamical equilibrium as a result of turnover and contact inhibition (Section 4.4 for details and testing of the homeostatic tissue).

4.1.3 Cancer cells and *proliferation signal*

Tumours have increased proliferative and invasive potential with respect to stroma [37]. To model this we do not impose contact inhibition constraints on cancer cells, that is as long as there is one empty neighbouring space in the neighbourhood of a cancer cell, it will be able to divide. An intermitotic time I, drawn from a uniform distribution calibrated on experimental measures, is assigned to each newborn cancer cell.

The behaviour and viability of cancer cells is determined by the local *proliferation signal*, $p(\mathbf{x}, t)$ (Fig. 4.1 C and p, respectively). When local concentrations of the *proliferation signal* are high growth is enabled, and a cancer cell successfully progresses through the cell cycle and divides. Lower values of the local concentration of the *proliferation signal* induces quiescence or cell death. Two thresholds are introduced, h_d and h_p, where $h_d, h_p \in [0, 1]$ and $h_d < h_p$. A cancer cell at position $\mathbf{x}$ at time t will die if $p(\mathbf{x}, t) < h_d$ as the local accumulation of signal is not sufficient to ensure viability. A cancer cell at position $\mathbf{x}$ at time t is in a proliferating state if $p(\mathbf{x}, t) \geq h_p$, since local pro-growth signalling is sufficient to allow progression through the cell cycle. A cancer cell at position $\mathbf{x}$ at time t will enter a quiescent state if local concentration values of the *proliferation signal* are between these thresholds (i.e. $h_d \leq p(\mathbf{x}, t) < h_p$). Progression through the cell cycle is paused when a cancer cell is quiescent. We do not allow variability in terms of intrinsic sensitivity of cancer cells to the inhibitor drug here as we are concerned only with the emergence of EMDR. In Chapter 8 we consider cancer cells with evolving sensitivity profiles.

Cancer cells are self-sustaining and provide autocrine promotion of the *proliferation signal* at a rate $\beta > 0$ (Fig. 4.1 and Fig. 4.5). The parameter β is calibrated with *in-vivo* experimental data to capture the growth dynamics of a drug-naive tumour (Section 5.3.3 for details).

When treatment commences, p is depleted at a rate $\delta > 0$. The parameter δ is calibrated with *in-vivo* experimental data to capture the death dynamics of a tumour treated with an inhibitor drug (Section 5.3.4 for details).

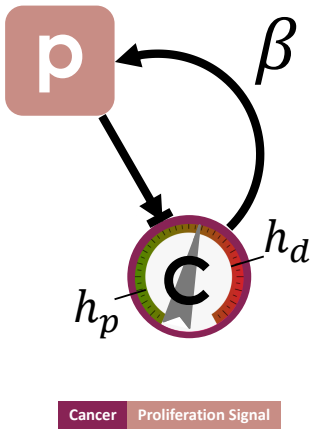

Figure 4.5: Cancer cells and the *proliferation signal*. Local *proliferation signal* intensity determines cancer cell behaviour according to two thresholds, h_d and h_p. Cancer cells can be either proliferating ($p \geq h_p$) or quiescent ($h_d \leq p < h_p$). If $p < h_d$ then they will die. Cancer cells provide autocrine promotion of the *proliferation signal* at rate β.

During treatment stromal activation can occur and activated stroma provides paracrine signalling that increases p at a rate $\gamma > 0$. The time to reactivation of the targeted pathway of an inhibitor drug in cancer cells undergoing therapy in an *in-vitro* experimental set up is used to calibrate parameter γ (Section 5.3.5 for details).

We do not include any form of movement in space of the *proliferation signal* as we mimic the accumulation of chemokines, such as growth factors, that are consumed locally or anchored to the ECM [219]. The *proliferation signal* is governed by the following PDE.

$$\frac{\partial p}{\partial t} = \left(\overbrace{\beta}^{\text{autocrine production}} + \overbrace{\gamma \sum_{\mathbf{y} \in \mathcal{M}_{\mathbf{x}}} a(\mathbf{y}, t)}^{\text{paracrine production}} \right) H(1-p) s(\mathbf{x}, t) - \overbrace{\delta d p}^{\text{drug inhibition}}, \quad (4.4)$$

where $\mathcal{M}_{\mathbf{x}}$ is the Moore neighbourhood of $\mathbf{x}$.

Here $s(\mathbf{x}, t)$ and $a(\mathbf{x}, t)$ are binary functions that indicate the presence/absence of a cancer cell, or an activated stroma cell at position $\mathbf{x}$ at time t, respectively:

$$s(\mathbf{x}, t) = \begin{cases} 1 & \text{if } \mathbf{x} \in \mathcal{C}_t, \\ 0 & \text{otherwise,} \end{cases} \quad (4.5)$$

and

$$a(\mathbf{x}, t) = \begin{cases} 1 & \text{if } \mathbf{x} \in \mathcal{A}_t, \\ 0 & \text{otherwise,} \end{cases} \quad (4.6)$$

where $\mathcal{C}_t$ and $\mathcal{A}_t$ are, respectively, the sets of cancer and activated stroma cell locations in Ω at time t. The Heaviside function, H, models a local saturation of total production once the concentration of p reaches 1.

During cell division we assume an initial local *proliferation signal* of at least, p_0,

where $h_d < p_0 \leq 1$ at each new cancer cell location.

Rigorous calibration of model parameters is based on experimental observations and quantifications, as described in Chapter 5.

4.2 Numerical approximation of partial differential equations

With our HDC model, we couple the stochastic dynamics of individual cells (cancer and stroma cells) with the deterministic dynamics of diffusible molecules (signalling molecules and the inhibitor drug) that act on different spatial and temporal scales. The molecular scale dynamics are modelled as continuous functions of time governed by PDEs (Eq. 4.2 and Eq. 4.4 for drug diffusion and *proliferation signal*, respectively).

We choose to discretize our PDEs using the explicit FTCS. For simplicity we use the same lattice size and spacing as the agent-based compartment of our model. While there are many numerical schemes that are available for us to use, we choose this scheme for its simplicity, tractability and frequent application in HDC modelling [220]. Descriptions of alternative discretization methods are available [220, 221, 222].

4.2.1 Drug concentration

We write the FTCS from Equation 4.2. We get:

$$d_{i,j}{}^{q+1} = d_{i,j}{}^{q}\left[1 - \Delta t\left(\mu v_{i,j}{}^{q} + \frac{4D_d}{(\Delta x)^2}\right)\right] + \Delta t\left[\frac{D_d}{(\Delta x)^2}\left(d_{i-1,j}{}^{q} + d_{i,j-1}{}^{q} + d_{i+1,j}{}^{q} + d_{i,j+1}{}^{q}\right)\right]. \quad (4.7)$$

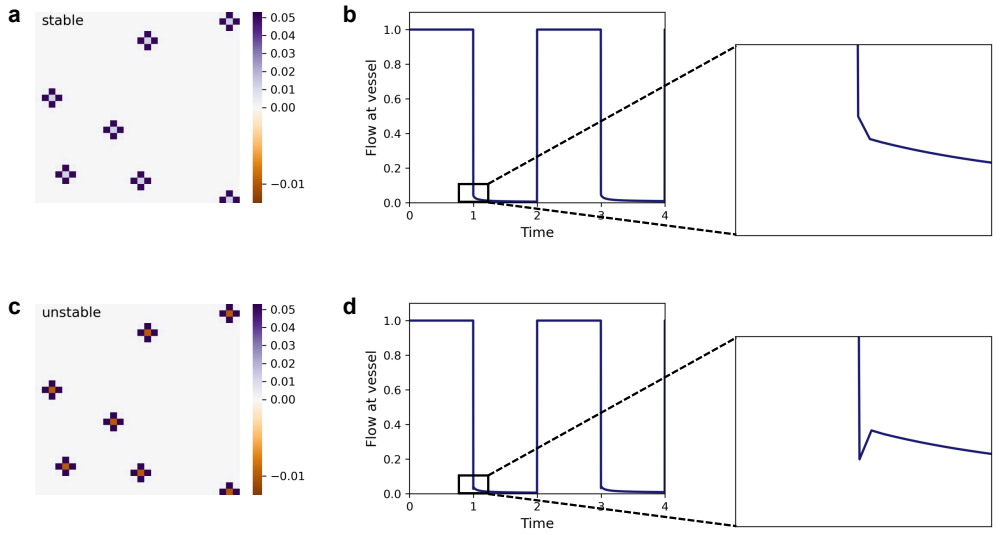

Figure 4.6: Comparison of stable and unstable numerical scheme for drug concentration. **a:** Drug concentration around vessel locations when the numerical scheme is stable ($\Delta t = 0.044$ hours). Here $d \geq 0$ for all locations. **b:** Timecourse of drug concentration net flow at a single representative vessel location where drug delivery and a break is alternated for two cycles. The inset shows the drug concentration flow transitioning smoothly when drug delivery is ceased. **c:** Drug concentration around vessel locations when the numerical scheme is unstable ($\Delta t = 0.05$ hours). Here we observe a numerical artefact where drug concentration values are negative at the vessel locations. **d:** Timecourse of drug concentration net flow at a single representative vessel location where drug delivery and a break is alternated for two cycles. The inset shows the drug concentration flow does not transition smoothly when drug delivery is ceased. The dip and rebound of the flow dynamics do not agree with the dynamics of the modelled system. Ensuring we capture realistic drug diffusion dynamics is crucial for our model.

We need to impose a constraint on Δt to ensure the stability of this explicit numerical scheme. To do this we consider the vessel sites in the worst-case scenario of no diffusion from neighbouring positions. In order to prevent $d < 0$, we require:

$$1 - \Delta t \left(\mu + \frac{4D_d}{(\Delta x)^2} \right) \geq 0. \tag{4.8}$$

This results in an upper bound on Δt:

$$\Delta t \leq \frac{1}{\mu + \frac{4D_d}{(\Delta x)^2}}. \tag{4.9}$$

The upper bound on Δt only applies to the drug concentration dynamics and it is not necessary for other compartments of the model to operate on such a fine grain. Hence, we update cell and *proliferation signal* dynamics every ten Δt to improve model efficiency.

Our intention is to model the smooth flow of drug concentration in and out of the vessel locations that mimics the smooth flow of blood in and out of the blood vessels. We construct a small *in-silico* experiment that alternates drug delivery with a holiday break for two choices of Δt, one where stability is ensured and the other where stability is not ensured. We show in Figure 4.6 inconsistencies that arise when the stability condition (Eq. 4.9) is not adhered to. In the stable case the drug concentration does not drop below zero (Fig. 4.6**a**), and the flow of drug concentration at vessel locations transitions smoothly when drug delivery is stopped (Fig. 4.6**b**). Conversely, in the unstable case the drug concentration becomes negative at the vessel locations (Fig. 4.6**c**), and the flow of drug concentration at the vessel locations is not smooth (Fig. 4.6**d**).

4.2.2 *Proliferation signal*

From Equation 4.4 we write the FTCS:

$$\begin{aligned} {p_{i,j}}^{q+1} = {p_{i,j}}^{q}\left[1 - \Delta t \delta {d_{i,j}}^{q}\right] \\ + \Delta t H (1 - {p_{i,j}}^{q}) {s_{i,j}}^{q} \left[\beta + \gamma \sum_{{y_{i,j}}^{q} \in \mathcal{M}_{{x_{i,j}}^{q}}} a({y_{i,j}}^{q}, t)\right]. \end{aligned} \tag{4.10}$$

We recall that $p \in [0, 1]$. If we ignore any addition to the proliferation from

autocrine and paracrine promotion, then we can determine a constraint on Δt that ensures the lower bound on p is adhered to. For $p \geq 0$, in the worst-case scenario with maximal drug, we have:

$$1 - \Delta t\delta \geq 0 \implies \Delta t \leq \frac{1}{\delta}. \tag{4.11}$$

We note here that for the parameter choices that we use in this thesis, the adherence to the upper bound on Δt due to the drug concentration (Eq. 4.9) ensures this constraint is also met.

While we ensure that $p \geq 0$, our choice of numerical scheme does not allow us to adhere to the upper bound on p. Suppose at time q there is a location with a cancer cell and a *proliferation signal* value very close to the upper bound. That is ${p_{i,j}}^q = 1 - \eta$ for some small value of η. Since $H(1 - {p_{i,j}}^q) = H(\eta) = 1$, we get:

$${p_{i,j}}^{q+1} = (1 - \eta)\left[1 - \Delta t\delta {d_{i,j}}^q\right] + \Delta t\left[\beta + \gamma \sum_{{y_{i,j}}^q \in \mathcal{M}_{{x_{i,j}}^q}} a({y_{i,j}}^q, t)\right]. \tag{4.12}$$

If we consider the case where there is no depletion of the *proliferation signal* due to the drug (${d_{i,j}}^q = 0$), then ${p_{i,j}}^{q+1}$ exceeds the upper bound if:

$$\eta < \Delta t\left[\beta + \gamma \sum_{{y_{i,j}}^q \in \mathcal{M}_{{x_{i,j}}^q}} a({y_{i,j}}^q, t)\right]. \tag{4.13}$$

If we take the limit as η approaches zero we get the upper bound, $\bar{p}$, on p of:

$$\bar{p} = 1 + \Delta t\left[\beta + \gamma \sum_{{y_{i,j}}^q \in \mathcal{M}_{{x_{i,j}}^q}} a({y_{i,j}}^q, t)\right]. \tag{4.14}$$

The upper bound for our chosen numerical scheme exceeds the upper bound on p. However, the error is small for small values of Δt ($\bar{p} \to 1$ as $\Delta t \to 0$).

4.3 Model implementation

We implement and simulate our model in Java using the Hybrid Automata Library (HAL) designed for hybrid modelling of cancer [223]. While HAL has mostly been used to simulate models developed to investigate cellular systems in oncological applications [224, 225, 226, 227, 228], it has also been used in other biological contexts [229, 230, 231].

4.4 Initial homeostatic tissue, tumour initiation and growth

To investigate tumour growth and the emergence of EMDR upon drug treatment in its microenvironment we need a tissue for the tumour to grow within and interact with.

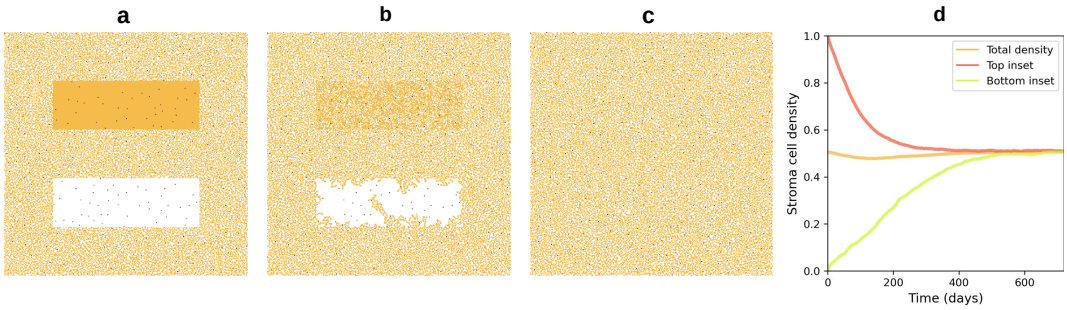

Figure 4.7: Tissue regeneration and homeostasis occur as a result of stroma turnover and contact inhibition. a-c: Progression towards homeostasis of stroma tissue of a single representative simulation of the model in the absence of cancer and inhibitor drug at: **a:** day 0, **b:** day 96, and **c:** day 720. There are two insets at day 0, one packed with stroma where there are no empty lattice positions (upper) and the other with all stroma removed (lower). By day 96 the upper inset is visibly less dense as the phenomena of contact inhibition prohibits stroma proliferation and we observe stroma cells infiltrating on the lower inset, mimicking the closure of a wound. At day 720 there is no evidence of the insets but rather a homeostatic bed of stroma. **d:** Stroma cell density for each inset and the whole domain from day 0 to day 720.

We construct a homeostatic bed of stroma cells as this initial tissue. Once a vessel distribution $\mathcal{V}$ in Ω is determined, all the remaining lattice locations are occupied

by stroma and the model is run, in the absence of cancer and inhibitor drug, until equilibrium is reached. Due to the suitably calibrated stromal cell turnover and contact inhibition a homeostatic tissue emerges that is in a dynamic equilibrium.

We test the robustness of the dynamic equilibrium of the homeostatic bed of stroma cells in response to excessive density and bulk tissue removal. Two insets are created in the homeostatic tissue, one with densely packed stroma cells and the other is left empty of stroma cells (Fig. 4.7**a**). We observe the densely packed inset becoming less dense and stroma cells infiltrating the empty inset mimicking the phenomena of contact inhibition and the process of wound healing as the system is evolved through time using the model (Fig. 4.7**b**). Both insets exhibit the same homeostatic state as the remaining tissue after sufficient period of time (Fig. 4.7**c - d**). Our model captures both contact inhibition and wound healing-like behaviour, allowing us to investigate the complexity of cancer-stroma interactions under therapy in a homeostatic tissue.

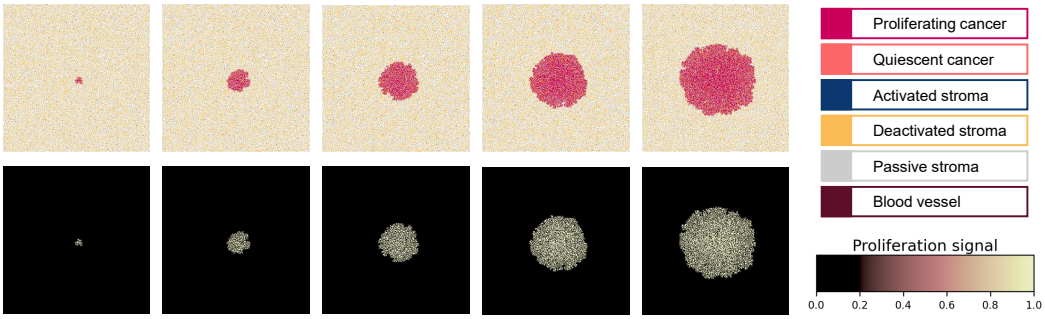

Figure 4.8: Tumour growing in homeostatic tissue to create the initial condition. We mimic a metastatic event by placing a single cancer cell adjacent to a central vessel location and evolve the system through time in the absence of the drug until a cancer cell population of 10^4 cells is reached. Spatial distributions and corresponding *proliferation signal* fields for five timepoints during the simulation are shown. The final spatial distribution of agents in Ω and the corresponding *proliferation signal* field is used as the initial condition for all our *in-silico* experiments.

We next introduce cancer. To mimic a metastatic event, we initiate disease by introducing a single cancer cell, adjacent to a central vessel, in the homeostatic tissue. The system in evolved through time allowing the cancer cell to

proliferate. This results in a tumour forming in the centre of Ω. When the number of cancer cells reaches 10^4 (a realistic detection level) the model is stopped, and we use the configuration of the system at this point as the initial condition for further experimentation and analysis of EMDR (Fig. 4.8). With this setup, we investigate the complex dynamics that emerge as a result of the multiscale interactions between cancer cells and the TME, shaped by signalling cues and delivery of an inhibitor drug.

4.5 Discussion

In this chapter we described the construction of our model, designed to capture the temporal and spatial dynamics of a solid tumour that is growing within a pre-existing homeostatic non-cancerous tissue. Therapy with a molecularly targeted drug can be introduced, delivered via the vascular system of the tissue (described in Section 2.1.2). The molecularly targeted drug reduces the pro-growth/anti-apoptotic signalling sensed by the cancer cells, affecting their proliferation and survival. The TME responds by stress-triggered CAFs activation that provides paracrine signalling that can rescue the cancer, capturing a potential mechanism of EMDR. We used a HDC model framework (described in Chapter 3) that allowed us to couple the stochastic dynamics of individual cells (cancer and stroma cells) with the deterministic dynamics of diffusible molecules (signalling molecules and the inhibitor drug).

In the Chapter 5 we discuss our model parameter calibration. The model parameters are rigorously calibrated and validated using *in-vitro* and *in-vivo* experimental data.

Chapter 5

Calibration of Model Parameters

In Chapter 4 we have presented a HDC model that captures the temporal and spatial dynamics of a solid tumour that grows within and interacts with its microenvironment while undergoing molecularly targeted therapy. For our model outputs to be considered relevant and reliable, our model parameters need to be carefully calibrated. We use existing data from the literature and, *in-vitro* and *in-vivo* experimental data to calibrate our model. We focus on a NSCLC cell line based on the availability of experimental data. While we attempt to calibrate as many of our model parameters to this type of cancer as we can, we note that this is not possible for some of our model parameters. The techniques we explain here can, however, be applied to equivalent datasets for another molecularly targeted cancer type. In a clinical setting our model can potentially be calibrated directly with patient derived data. Most of the material in this chapter is based on the work undertaken for this thesis that has been published [1].

We first discuss our parameter choices for the construction of the homeostatic tissue, including the structure of the lattice, the vessel and stroma distribution and diffusion of the molecular scale drug. These parameters are calibrated with data available in the literature. The cancer cell growth, and death, dynamics are calibrated and validated with *in-vivo* experimental data for an untreated, and treated, xenograft mouse models, respectively. We use *in-vitro* experimental

data to calibrate the rate of stromal rescue when the tumour is treated with the inhibitor drug.

5.1 Homeostatic tissue construction

The parameters associated with the construction of the homeostatic tissue are presented in Table 5.1.

Param.	Description	Value	Reference
h_r	inhibitor drug threshold for stroma activation	0.93	Model specific
π	proportion of reactive to passive stroma	0.5	Model specific
$\mid \Omega \mid$	domain size	0.3 cm $\times$ 0.3 cm	Model specific
Δx	lattice spacing	10 μm	Eukaryote cell size [233]
σ_{mean}	average distance between vessel sites	0.016 cm	[217]
σ_{min}	minimum distance between vessel sites	0.008 cm	[217]
I	cell intermitotic time	$U[0.9, 1.1]$ days	[234, 235]
p_T	stroma cell turnover probability	0.0042 day^{-1}	[217]
p_A	stroma cell activation probability	0.042 day^{-1}	Model specific
n_{CI}	contact inhibition	2 cells	Model specific

Table 5.1: Model parameters associated with the homeostatic tissue. Lattice spacing and vessel configuration parameter values are taken from experimental data. Parameter values governing cell cycle length and stroma turnover are informed by experimental data. Other parameter values are chosen specific to our model.

Since we assume the tumour is in the avascular stage we set the size of the tissue,

Ω, large enough to accommodate a tumour at the limit of this stage [232]. We model the homeostatic tissue using a square lattice with spacing, Δx, chosen to represent the diameter of a eukaryotic cell. While eukaryotic cells range in size, we choose a value from within the range that is reported in the literature [233]. To implement the circle packing algorithm that determines the vessel placement in the tissue, we use values for the minimum and average distance between vessels [218].

The homeostatic tissue is comprised mainly of stroma cells. Each stroma cell is assumed to be in a proliferating state and progresses through the cell cycle in one day [234, 235]. To maintain a homeostatic tissue there are mechanisms at play that suppress proliferation. These are determined by cell-to-cell contacts [37]. To model this phenomenon of normal tissue, the stroma cells in our model are subject to contact inhibition. The associated model parameter, N_{CI}, is a measure of the density of stroma within the tissue. Since the density of tissue within and across individuals and tissues is variable, for the purposes of our analysis we choose an arbitrary value. The turnover of stroma cells depends on parameter p_T. The value we choose is guided by the literature [217, 236]. Since there is considerable variability in the stromal content with tissue from an individual patient, and across different patients, we choose an arbitrary proportion of the stroma as reactive (π). While the crosstalk between cancer cells and the TME that induces environment-mediated resistance is not fully understood we assume CAFs provide paracrine rescue when stress cues, emitted by proximal cancer cells, are sensed. To mimic the stress-triggered rescuing response of CAFs during therapy we assume cancer cells will signal for assistance when the drug concentration is high. Therefore, we set the threshold for activation (h_r) close to, but lower than, maximum saturation. In order for the stromal activation to occur on a quicker timescale than the turnover, we set $p_A = 10p_T$.

5.2 Molecularly targeted drug

Molecular scale dynamics operate on a much smaller scale than the cell scale dynamics. The molecularly targeted drug enters through the vessel sites at

maximum concentration and diffuses into Ω. We calibrate the diffusion coefficient, D_d, using data for the molecular weight of inhibitor drugs (Table 1 in [237]). From the molecular weight we estimate the molecular radius [238]. With this estimated radius we can extrapolate the diffusion coefficient using experimental data (Fig. 1 in [239]). The drug diffuses into the vessels and is cleared at rate μ from the domain once the treatment is stopped. We arbitrarily choose the value of μ to ensure that the drug is cleared from the domain within a reasonable time frame. Our chosen values of D_d and μ determine the value of the timestep, Δt, (Eq. 4.9). Since the cell-scale dynamics do not need to operate at such a fine grain, they are determined every ten Δt. Finally, the drug delivery and drug holiday period lengths (τ_T and τ_H) are varied for our analysis. Our choices of τ_T and τ_H are within clinically relevant time frames.

The parameters associated with the administration of the molecularly targeted drug are presented in Table 5.2.

Param.	Description	Value	Reference
D_d	inhibitor drug diffusion coefficient	10^{-5} cm^2 day^{-1}	Extrapolated from [239], based on radius [238], for average molecular weight of inhibitor drugs [237]
μ	rate of inhibitor drug removal at vessel site	500 day^{-1}	Model specific
τ_T	treatment period length	varies	Model specific
τ_H	holiday period length	varies	Model specific
Δt	length of timestep	0.044 hours	Model specific

Table 5.2: Model parameters associated with the molecularly targeted drug. The diffusion coefficient value is estimated using experimental data. The drug removal rate is specific to our model. These parameter values determine the length of the timestep. Treatment scheduling parameter values are varied.

5.3 Cancer cells and the *proliferation signal*

Like the stroma cells, cancer cells have an intermitotic time of one day (Table 5.1). Our choices of the threshold for death and proliferation (h_d and h_p) are arbitrarily chosen, ensuring $h_d < h_p$. Cancer cell behaviour depends on local concentrations of the *proliferation signal* (Eq. 4.4). Using *in-vivo* experimental data of untreated and treated tumours, we employ Approximate Bayesian Computation (ABC) to calibrate the cancer cell intrinsic growth and death parameters. We calibrate the rate of stroma-derived paracrine promotion parameter with *in-vitro* experimental data.

5.3.1 Approximate Bayesian Computation

Parameter calibration within a Bayesian inference framework has become widely adopted for models of complex biological systems, [240, 241, 242]. ABC is a likelihood-free method [240, 241]. Early applications of ABC for parameter calibration arose in the field of genetics, where there was a need of a mathematically sound technique that could be implemented when calculation of the likelihood function is difficult [243, 244, 245, 246]. Within a Bayesian inference framework, for a given set of model parameters, $\zeta \in \mathcal{Z}$ with some known prior distribution $\Psi(\zeta)$, and observed data, $\hat{q} \in \mathcal{Q}_{\text{obs}}$, the posterior distribution $\Psi(\zeta \mid \hat{q})$ of model parameters is approximated by considering the likelihood of obtaining model outputs that are comparable (by measure a $\mathcal{F}$) to the set of observed data, within some measurable threshold ϵ.

There have been many algorithms developed to implement ABC [240, 247, 248, 249]. For our parameter calibration we use the rejection algorithm with Euclidean distance as our measure $\mathcal{F}$. Although it has been widely described in the literature ([241, 242, 244]), we provide an outline of the algorithm here.

Rejection algorithm

For $i = 1, \ldots, N$:

1. Sample ζ_i from the prior distribution $\Psi(\zeta)$ of model inputs.

2. Simulate output q_i with the model for input ζ_i.

3. Reject ζ_i if $\mathcal{F}(q_i, \hat{q}) > \epsilon$, otherwise $\zeta_i \in \Psi(\zeta \mid \hat{q})$.

5.3.2 *In-vivo* and *in-silico* experimental model set up

We calibrate the growth of cancer cells in the absence of treatment and the initial rate of decay when undergoing molecularly targeted therapy using *in-vivo* xenograft model data provided by the Marusyk Lab (Department of Tumor Microenvironment and Metastasis, H. Lee Moffitt Cancer Center). ALK+ NSCLC cells (cell line - H3122) are subcutaneously injected into flanks of five NSG mice ($n = 10$), for both the vehicle control and treatment (ALK inhibitor - *alectinib*) groups. Calliper-based measurements are used to monitor tumour growth. Further details of the cell line and the *in-vivo* experimental set up are provided in Appendix C. Since the growth dynamics of Human NSCLC cells subcutaneously injected into mouse xenograft models have very different growth dynamics to that of the same cells in human tissue, we modify the model setup in order to replicate the experimental one. Given the time frame of the experiment, we expect no infiltration of non-cancerous cells and reduced spatial constraints in the xenograft model. Therefore, we remove stroma cells from our model and increase the radius of division.

We construct an initial condition for the calibration by placing a single cancer cell in the centre of the domain and allow for proliferation in ideal conditions ($p_0 = h_p$ and $\beta = 1$) until a tumour consisting of 10^4 cells is formed. Our choice of parameters p_0 and β are used to create the initial configuration of cancer cells for our initial condition that does not carry memory of these parameters. This configuration is then used to calibrate the growth dynamics of the tumour against the average of the vehicle control data (untreated xenografts). We use ABC to refine a uniform joint prior distribution for parameters p_0 (the initial local *proliferation signal* value assigned to cancer cells when they divide), and β (the rate of autocrine production), to identify a posterior distribution that matches the experimental data. We choose point estimates from the posterior distribution for our p_0 and β values.

5.3.3 Initial local *proliferation signal* p_0 and the rate of autocrine production β

Firstly, we are tasked with determining the ranges of the uniform prior on each parameter. By our model construction, autocrine signalling production at rate β brings the local concentration of *proliferation signal* from p_0 to the threshold for proliferation h_p, sufficient for a cancer cell in a drug-free environment to divide. Hence, we impose the upper bound $p_0 < h_p$.

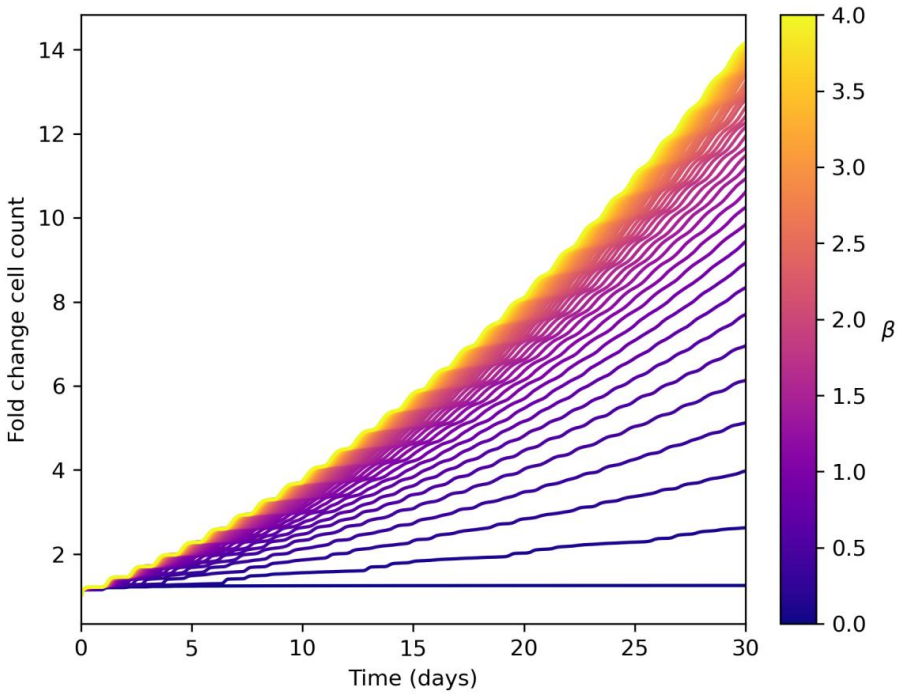

Figure 5.1: Growth dynamics as β varies. Fold change cell count over time for $\beta \in [0, 4]$. The experimental set up is the same as for the calibration of β. As β increases the fold change cell counts converge. Once β reaches a high enough value, cancer cells have sufficient autocrine signalling to reach a proliferative state before they are able to divide. Tumour growth is then limited by spatial constraints and cancer cell intermitotic time, saturating the parameter β.

When β is sufficiently high, p quickly reaches h_p and tumour growth depends on spatial constraints only, hence increasing β has a saturating effect on growth

dynamics. A maximum value of β is chosen that is greater than this saturation point (Fig. 5.1).

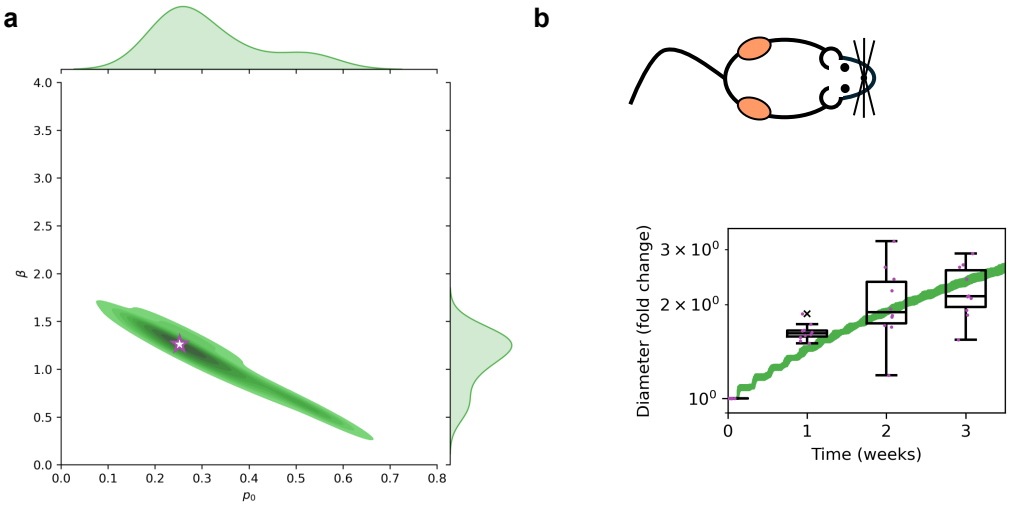

Figure 5.2: Experimental calibration of p_0 and β. a: The joint and marginal posterior distributions for p_0 and β obtained by ABC with $N = 10^4$ and $\epsilon = 0.018$. Inverse correlation is shown between p_0 and β accepted values. The chosen point estimates: $p_0 = 0.256$, $\beta = 1.25$ are marked with a star. **b:** The diameter fold change for *in-vivo* experimental data for the vehicle control replicates ($n = 10$, ***black*** boxplots and ***purple*** data points) and *in-silico* tumours (***green*** time series for parameter regimes corresponding to the (p_0, β) posterior distribution). For the boxplots, the centre line is the median; box limits are the upper and lower quartiles; whiskers are $\pm 1.5 \times$ IQR; and outliers are represented by a cross.

We use uniform priors: $(p_0, \beta) \in (U[0, h_p] \times U[0, 4])$, with pairs that result in an intermitotic time greater than two days discarded. We perform ABC with $N = 10^4$ and $\epsilon = 0.018$. A range of inversely correlated p_0 and β values is identified by the ABC (Fig. 5.2**a**). This result agrees with what we expect: high initial local pro-growth signalling requires lower autocrine production to sustain survival and proliferation, while a higher amount of autocrine signalling is required for the cancer cell to survive and proliferate if the initial local pro-growth signalling is low. We identify a peak in the posterior distribution corresponding to a p_0 value just above h_d and a β value over one. These are chosen as point

estimates ($p_0 = 0.256$, $\beta = 1.25$ day^{-1}) ensuring a good fit of the *in-silico* tumour growth dynamics to the vehicle control experimental cohort (Fig. 5.2**b**).

5.3.4 Rate of drug inhibition δ

In order to recapitulate the subcutaneous *in-vivo* experimental set up for the drug treated cohort we impose maximal drug concentration at the periphery of the tumour and allow it to diffuse into the tumour. We perform an initial scan of the tumour death dynamics for a range of δ values to identify a suitable uniform prior. From our scan we choose $\delta \in U[6, 7]$ as our prior distribution.

We then perform ABC with $N = 10^4$ and $\epsilon = 0.0005$, to calibrate the drug-induced tumour reduction against the average of the *in-vivo* experimental data of the drug treated cohort (Fig. 5.3**a**). We choose the point estimate for parameter δ that corresponds to the peak of the posterior distribution ($\delta = 6.68$ day^{-1}), from within the resulting posterior distribution ensuring a good fit of the *in-silico* tumour growth dynamics to the drug-treated experimental cohort (Fig. 5.3**b**).

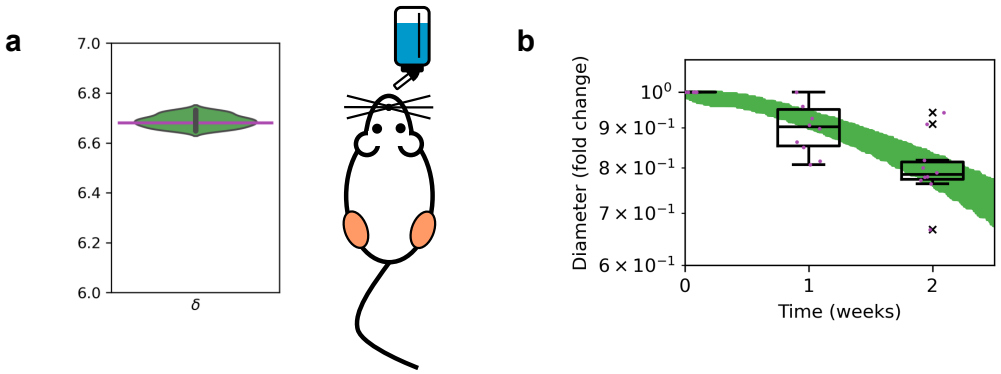

Figure 5.3: Experimental calibration of δ. a: The posterior distribution for δ obtained by ABC with $N = 10^4$ and $\epsilon = 0.0005$. Horizontal line marks the chosen point estimate. **b:** The diameter fold change for *in-vivo* experimental data for the drug-treated replicates ($n = 10$, ***black*** boxplots and ***purple*** data points) and *in-silico* tumours (***green*** time series for parameter regimes corresponding to the δ posterior distribution). For the boxplots, the centre line is the median; box limits are the upper and lower quartiles; whiskers are $\pm 1.5 \times$ IQR; and outliers are represented by a cross.

We have thus calibrated the parameters that govern cancer cell growth and death to *in-vivo* experimental data of NSCLC cells subcutaneously injected into the flanks of xenograft mouse models using ABC. We show violin plots of the resulting posterior distributions for the tumour growth parameters p_0 and β, and the tumour death parameter δ in Figure 5.4, indicating the chosen point estimates for each parameter.

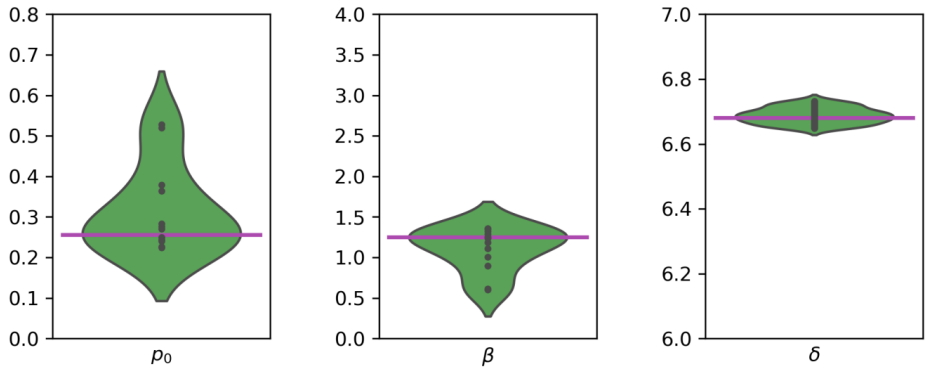

Figure 5.4: Summary of posterior distributions for individual parameters. Marginal posterior distributions for p_0 and β (corresponding to the joint posterior in Fig. 5.2**a**), and posterior distribution for δ (already shown in Fig. 5.3**a**) obtained by ABC. Horizontal lines mark the chosen point estimates ($p_0 = 0.256$, $\beta = 1.25$ day^{-1} and $\delta = 6.68$ day^{-1}).

5.3.5 Rate of paracrine production γ

We estimate the rate of paracrine production γ using the *in-vitro* experimental data in [10] to calibrate the rescue effect of CAFs. Their results show that tolerance to the inhibitor drug is conferred by melanoma-associated fibroblasts (the experimental counterpart to our reactive stroma cells), quantified by the restoration of ERK signalling within 12 hours. We let t_R be this time to recovery. In our modelling framework t_R corresponds to the average time it takes cancer cells in stromal co-cultures treated with the targeted drug to replenish their *proliferation signal*. We can calibrate parameter γ by matching this average time to the experimental measure, as follows.

Consider a cancer cell experiencing the *proliferation signal* at the threshold h_d when treatment starts at time t_0. We can simplify Equation 4.4 to consider the worst case scenario of the inhibitor drug concentration at maximum concentration ($d = 1$) and minimum paracrine help (one out of eight neighbouring activated reactive stroma cells), to obtain:

$$\frac{\partial p}{\partial t} = \beta + \gamma - \delta p, \tag{5.1}$$

which has solution:

$$p(t) = \frac{\beta + \gamma}{\delta} + \left(h_d - \frac{\beta + \gamma}{\delta} \right) e^{-\delta(t - t_0)} := \theta(h_d, \gamma, t - t_0) \text{ for } t > t_0. \tag{5.2}$$

To be effective in rescuing a cancer cell from its death fate, the single activated stroma cell must push the local *proliferation signal* above h_p. Hence, a lower bound on the paracrine production rate, $\underline{\gamma}$, is obtained, imposing:

$$\theta(h_d, \underline{\gamma}, t_R) \geq h_p. \tag{5.3}$$

Note that $\underline{\gamma}$ depends on the choice of β and δ. Additionally, note that this condition cannot be solved explicitly for γ. Hence, the lower bound, $\underline{\gamma}$, on the paracrine production rate is determined numerically. With our choice of $\beta = 1.25$ and $\delta = 6.68$, the numerical lower bound is $\underline{\gamma} = 4.2412$. We choose $\gamma = 4.242$ day^{-1} cell^{-1}.

The resulting parameter values associated with the cancer cells and *proliferation signal* are presented in Table 5.3. In Appendix D we present an alternative calibration using individual replicate data.

Param.	Description	Value	Reference
h_d	*proliferation signal* threshold for death	0.2	Model specific
h_p	*proliferation signal* threshold for proliferation	0.8	Model specific
p_0	*proliferation signal* at birth	0.256	Experimentally calibrated (Section 5.3.3)
β	*proliferation signal* autocrine production	1.25 day^{-1}	Experimentally calibrated (Section 5.3.3)
γ	*proliferation signal* paracrine production	4.242 day^{-1} cell^{-1}	Experimentally calibrated (Section 5.3.5)
δ	*proliferation signal* degradation by inhibitor drug	6.68 day^{-1}	Experimentally calibrated (Section 5.3.4)

Table 5.3: Model parameters associated with the cancer cells and the *proliferation signal*. Threshold parameter values are chosen specific to our model. Parameter values that govern cancer cell growth and death are calibrated to *in-vivo* experimental data. The paracrine rescue parameter value is calibrated to *in-vitro* experimental data.

5.4 Validation of the calibrated model

We seek to validate the chosen parameter regime by comparing the output of our calibrated model to the post-treatment regrowth dynamics of additional *in-vivo* experimental data. The tumour diameters of the NSCLC mouse xenografts ($n = 10$) treated with ALK inhibitor (experimental setup described in Section 5.3.4) are measured for four weeks after stopping treatment. We simulate a drug delivery period followed by a period where drug delivery is ceased, to match this experimental setup *in-silico*. We allow the drug to diffuse out of the domain.

Time series profiles of the tumour diameter fold change for 30 simulations of the *in-silico* experiment match the *in-vivo* experimental data for the regrowth period well, thus validating the parameter calibration (Fig. 5.5).

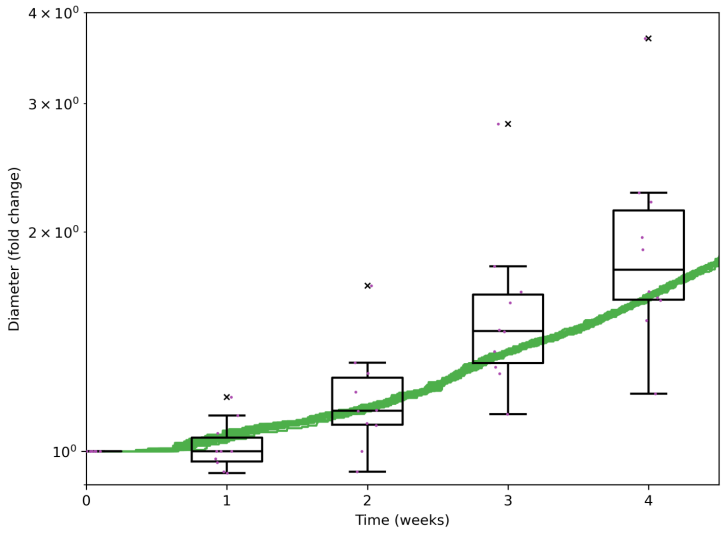

Figure 5.5: Validation of the calibrated parameters to *in-vivo* experimental data. The tumour diameter fold change for *in-silico* tumours (***green*** time series for 30 simulations of the model with $p_0 = 0.256$, $\beta = 1.25$ and $\delta = 6.68$) is compared to the *in-vivo* experimental data for the drug-treated replicates post treatment ($n = 10$, ***black*** boxplots and ***purple*** data points). For the boxplots centre line is the median; box limits are the upper and lower quartiles; whiskers are $\pm 1.5 \times$ IQR; and outliers are represented by a cross.

5.5 Discussion

In this chapter we discussed the calibration of our model parameters. The parameters associated with the construction of the homeostatic tissue and the molecular scale diffusion dynamics were calibrated with data available in the literature. We rigorously calibrated the growth and death dynamics of the cancer cells in our HDC model with *in-vivo* experimental data using ABC and validated our calibrated parameter choices with extended *in-vivo* experimental

data. We used *in-vitro* experimental data to calibrate the rate of paracrine signalling rescue provided by the activated stroma.

In Chapter 6 we integrate all the calibrated parameters into the model. With all the calibrated parameters integrated we can capture the tissue-scale dynamics that result from the cell-scale interactions of a solid tumour undergoing therapy with a molecularly targeted drug. We test our model for continuous treatment and observe the emergence of resistance and eventual treatment failure. Next, we investigate introducing breaks in treatment, that exploit the transient nature of the reactive stroma, to modulate tumour burden. We then characterise the resulting residual disease.

Chapter 6

Treatment Scheduling and Patterns of Residual Disease

In Chapter 4 we describe a model that captures the temporal and spatial dynamics of a solid tumour, embedded within homeostatic tissue, while undergoing therapy with an inhibitor drug that is delivered through the tissue's vasculature. In Chapter 5 we calibrate and validate the model parameters using *in-vitro* and *in-vivo* experimental data. In this chapter we use the calibrated model to explore, through intermittent treatment regimes, the implications of the transient and reversible nature of stroma reactivity. First, we consider a landscape of intermittent treatment schedules and determine a regime that displays sustained control of tumour burden at low levels (i.e. residual disease). We then analyse the residual disease and characterise it in relation to the TME temporal evolution and the cancer-stroma crosstalk throughout the treatment regime. Our focus is specifically on the density and co-localisation of cancer cells and activated stroma cells over time. Then we explore the diffusion dynamics of the inhibitor drug delivered via the tissue's vascular system, and of the *proliferation signal*, establishing a link between treatment outcome and the local vessel density. We begin to elucidate the complex dynamics behind the development of transient resistance observed in tumours undergoing targeted therapy with inhibitor drugs with our spatial and temporal analysis. Most of

the material in this chapter is based on the work undertaken for this thesis that has been published [1].

6.1 Continuous treatment

Without treatment the tumour will continue to grow after detection ($t = 0$) as cancer rapidly invades the homeostatic tissue (Fig. 6.1**a** for the tumour burden and **b** for the spatial distribution of Ω and drug field). However, if the tumour is treated continuously from detection with the inhibitor drug, we observe an initial reduction in tumour burden (Fig. 6.1**a**). As the *proliferation signal* is depleted, cancer cells become quiescent, and once the local *proliferation signal* is brought below h_d, they die (Fig. 6.1**c**). As treatment continues there is progressive activation of reactive stroma that, through paracrine promotion of the *proliferation signal*, rescue a portion of cancer cells by returning them to a proliferative state (Fig. 6.1**d**). This eventually results in tumour regrowth and treatment failure (Fig. 6.1**a** and Fig. 6.1**e**).

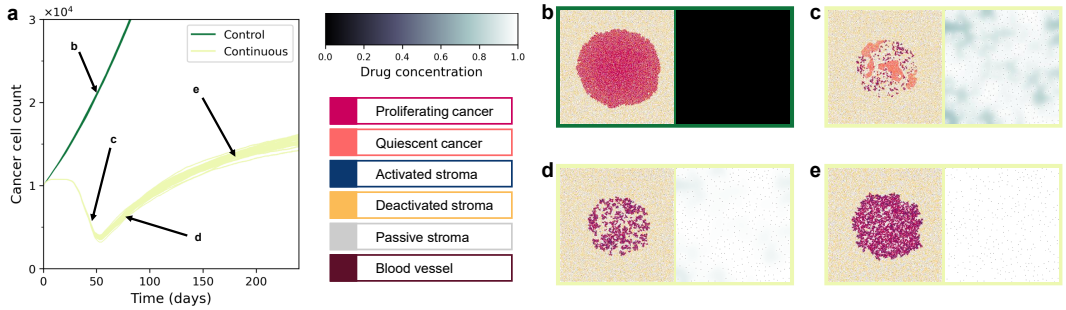

Figure 6.1: Outcome of continuous treatment. a: Tumour burden for $t \in [0, 240]$ days under no treatment and continuous treatment. Individual realisations are shown, with 30 stochastic simulations conducted for both untreated and treated conditions. Continuous treatment initially displays a very good response to treatment, followed by EMDR-driven relapse. **b - e** show spatial distribution (left) and drug concentration (right) at representative time points for a single simulation. **b:** Day 51 for the untreated tumour. **c:** Day 45 of continuous treatment, **d:** Day 75 of continuous treatment, and **e:** Day 181 of continuous treatment. Animations of the *proliferation signal*, spatial distribution and drug concentration for the untreated and treated scenarios are available in Appendix E.

Under continuous treatment conditions, the cumulative effect of stromal activation operates on a longer timescale than that of the *proliferation signal* depletion, resulting in the observed delay of the tumour regrowth following the initial response to the inhibitor drug. The timescale of the regrowth dynamics of the continuously treated tumour, dependent on the additional paracrine signalling provided by the activated stroma, is slower than the timescale of the drug-naive tumour (Fig. 6.1**a**). Furthermore, we note that the resulting tissue of the drug-naive tumour consists of a dense mass of cancer cells while the resulting tissue of the continuously treated tumour is composed of clusters of surviving, proliferative cancer cells infiltrated by activated reactive stroma (Fig. 6.1**e**).

6.2 Intermittent treatment scheduling

We can exploit the transient and reversible nature of therapy triggered stromal activation by modulating drug delivery through introducing breaks in treatment delivery. Namely, by using intermittent treatment schedules where delivery of the inhibitor drug is paused during treatment holidays, allows the promoting and rescuing action of reactive stroma to be managed. However, the reduction of overall stromal activation through pauses of drug delivery comes at the expense of loss of control on tumour burden. Namely, during pauses in treatment, activated reactive stroma eventually deactivates when the drug concentration is reduced while no additional drug enters Ω and the drug already in Ω diffuses out through the vessels. Without the local paracrine assistance provided to rescue cancer cells from the activated reactive stroma, the cancer cells that rely on paracrine assistance can become quiescent and die. However, some cancer cells can survive despite the loss of the paracrine assistance and when the local drug concentration decreases sufficiently, they can re-enter a proliferative state. A surge in proliferation can occur over a treatment holiday, although growth can be hindered by spatial competition from stroma cells that, during the previous treatment delivery, had infiltrated the space freed up by bulk cancer cell death. Crucially, the overall outcome of an intermittent treatment regime depends on the prevalence and timescales of all these

processes. To investigate this further we consider intermittent treatment schedules with regular alternating periods of drug delivery and drug holiday. We let τ_T and τ_H be the length of the drug delivery and drug holiday periods, respectively. One cycle of treatment consists of one drug delivery period followed by one drug holiday period ($\tau_T + \tau_H$).

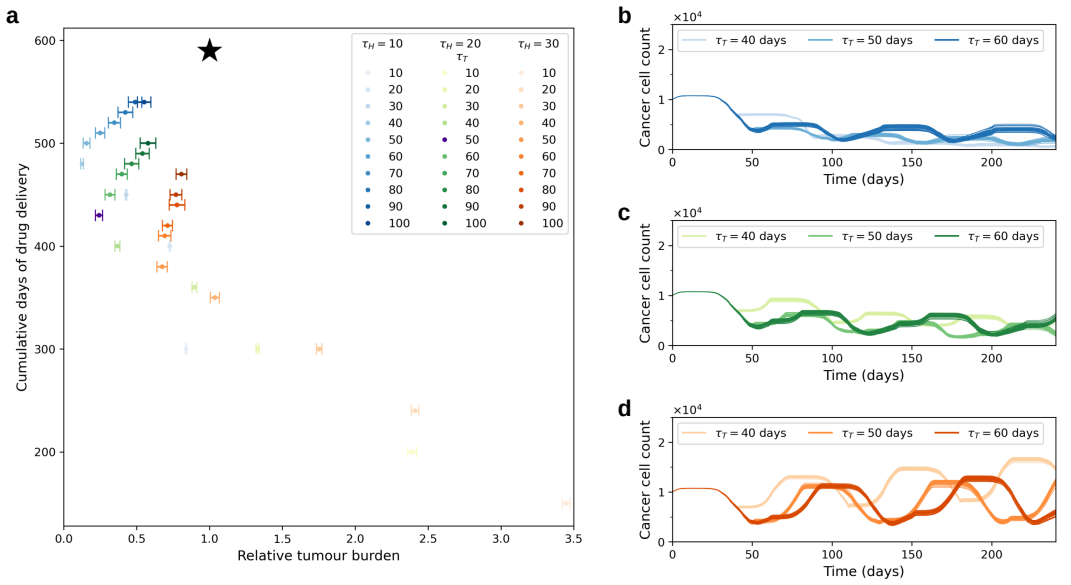

Figure 6.2: Investigation of treatment regimes. **a** Cumulative days of drug delivery (measured as the sum of drug delivery days over 590 days of therapy) against relative tumour burden (measured as the sum of total cancer cell count over the $t \in [0, 590]$ day window normalised to the continuous treatment case) for $\tau_T = \{10, 20, 30, 40, 50, 60, 70, 80, 90, 100\}$ days for $\tau_H = 10$ days (*blue*), $\tau_H = 10$ days (*green*), and $\tau_H = 30$ days (*orange*). Results show the average of 30 simulations of each schedule and includes 95% confidence intervals. The star indicates measures for continuous treatment. As τ_H increases the relative tumour burdens for each τ_T also increases and while the cumulative days of treatment decreases. Relative tumour burden initially decreases as cumulative days of drug delivery increases, but from; $\tau_T = 40$ days for the $\tau_H = 10$ days regime; and $\tau_T = 50$ days for the $\tau_H = \{20, 30\}$ days regimes; the relative tumour burden increases. **b - d** show tumour burden over 30 simulations for treatment regimes $\tau_T = [40, 50, 60]$ days from day 0 to day 240. **b:** $\tau_H = 10$ days. **c:** $\tau_H = 20$ days. **d:** $\tau_H = 30$ days. These intermittent treatment schedules show, overall, a long-term improved outcome compared to continuous treatment.

First, we compare the outcomes of multiple replicates of different intermittent

treatment regimes $\tau_H = 10$ days, $\tau_H = 20$ days and $\tau_H = 30$ days with $\tau_T = \{0, 10, 20, 30, 40, 50, 60, 70, 80, 90, 100\}$ days over 590 days of therapy. We consider the overall tumour burden and the cumulative days of drug delivery, relative to the continuous treatment case. With these measures we quantitatively consider the trade-off between reduction of tumour burden and duration of pharmaceutical intervention. We observe a non-linear correspondence between τ_T and relative tumour burden for each choice of τ_H (Fig. 6.2**a**).

The cumulative days of drug delivery decreases, and the relative tumour burden increases as τ_H increases for each choice of τ_T (Fig. 6.2**a**). When $\tau_T < 50$ days the significant residual disease present at the end of the first drug delivery period almost always is indicative of treatment failure. For intermittent treatment regimes with $\tau_H = 10$ days there is no tumour regrowth in holiday periods (Fig. S6.2**b**). For intermittent treatment regimes where $\tau_H > 10$ days tumour regrowth in the holiday period is observed, consistent with experimental results [72]. The regrowth during drug holiday periods increases as τ_H increases resulting in overall higher amounts of residual disease. This is observed when tumour regrowth during the drug holiday period for $\tau_H = 20$ days (Fig. 6.2**c**) is compared to the greater tumour regrowth for $\tau_H = 30$ days (Fig. 6.2**d**). For each τ_H, the tumour burden decreases for $\tau_T < 50$ days and increases for $\tau_T > 50$ days. The $\tau_T = 50$ days regime for each τ_H results in the lowest tumour burden.

In Figure 6.3 we show examples of the resulting tumour burden for varying lengths of drug delivery period τ_T, with $\tau_H = 20$ days. Consistent with the above analysis, we observe that with short treatment periods ($\tau_T = 10$ days) tumour growth continues as the drug concentration in the domain is not sufficient to cause death in the cancer population (Fig. 6.3**b**). Some tumour burden control is achieved for $\tau_T = 30$ days, where the tumour growth is reduced but not sufficiently for long-term control (Fig. 6.3**c**). After approximately 150 days the outcome is quantitatively comparable to that of the continuous treatment regime. Significant reduction in tumour burden within the first two treatment periods (Fig. 6.2**c**) and long-term control of tumour burden at low levels is observed for treatment period lengths greater than 30 days (Fig. 6.3**d - e**).

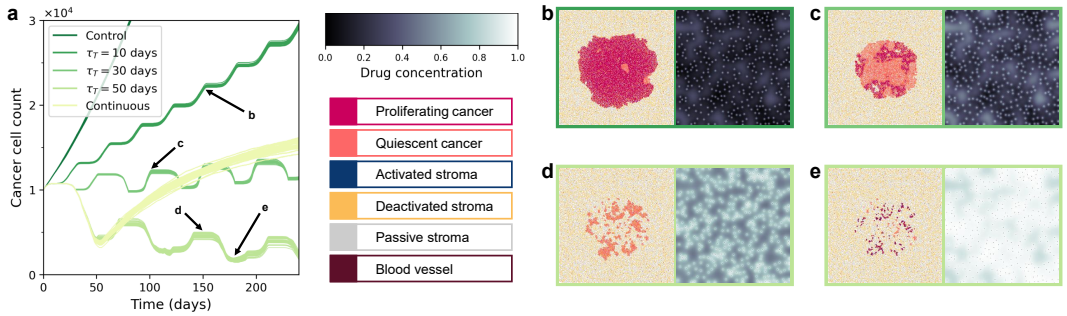

Figure 6.3: Exploration of treatment scheduling. **a:** Tumour burden for $t \in [0, 240]$ days under no treatment, continuous treatment, and five intermittent treatment schedules ($\tau_T = \{10, 30, 50\}$ days and $\tau_H = 20$ days). Individual realisations are shown, with 30 stochastic simulations conducted for both untreated and treated conditions. As the length of the treatment period τ_T of intermittent treatment increases a reduction in tumour burden is observed. **b - e** show spatial distribution (left) and drug concentration (right) at representative time points for a single simulation of the regime of interest. **b:** Day 150 of intermittent treatment ($\tau_T = 10$ days, $\tau_H = 20$ days) regime. **c:** Day 100 of intermittent treatment ($\tau_T = 30$ days, $\tau_H = 20$ days) regime. **d:** Day 150 of intermittent treatment ($\tau_T = 50$ days, $\tau_H = 20$ days) regime. **e:** Day 181 of intermittent treatment ($\tau_T = 50$ days, $\tau_H = 20$ days) regime. Animations of the *proliferation signal*, spatial distribution and drug concentration for each treatment regime are available in Appendix E.

Although most inhibitor drugs have reduced toxicity, a crucial factor to consider in the context of clinical decision-making over treatment scheduling would be the cumulative drug delivery time. Therefore, it is essential to consider the trade-off between minimising relative tumour burden and limiting cumulative treatment days. Under the parameter regime adopted here, considering this trade-off while also capturing the observed experimental results we choose intermittent regime $\tau_T = 50$ days and $\tau_H = 20$ days to investigate how fluctuating environmental conditions modulate transient stroma activation, crosstalk with cancer, and, ultimately, the resulting residual disease.

It is important to note that these quantitative results rely on the specific parameter regime adopted (Chapter 5 for details of the experimentally informed parameter calibration). Model parameters would have to be calibrated against patient-specific measurements in a clinically relevant scenario.

6.3 Spatial attributes of environmentally mediated drug resistance

With the treatment regime $\tau_T = 50$ days and $\tau_H = 20$ days we observe control of tumour burden but not eradication. In Figure 6.4**a** we show mean-field drug concentration, along with cancer and activated stroma cell counts over 590 days. The dynamics settle around an approximately cyclic pattern after two treatment cycles and we observe that over following consecutive treatment cycles, the location of surviving cancer is in similar regions. In Figure 6.4**b** we show the spatial configurations of residual disease at corresponding times of three consecutive treatment cycles for one realisation. It can be seen that cancer persists in the same regions in Ω for each of the time points considered.

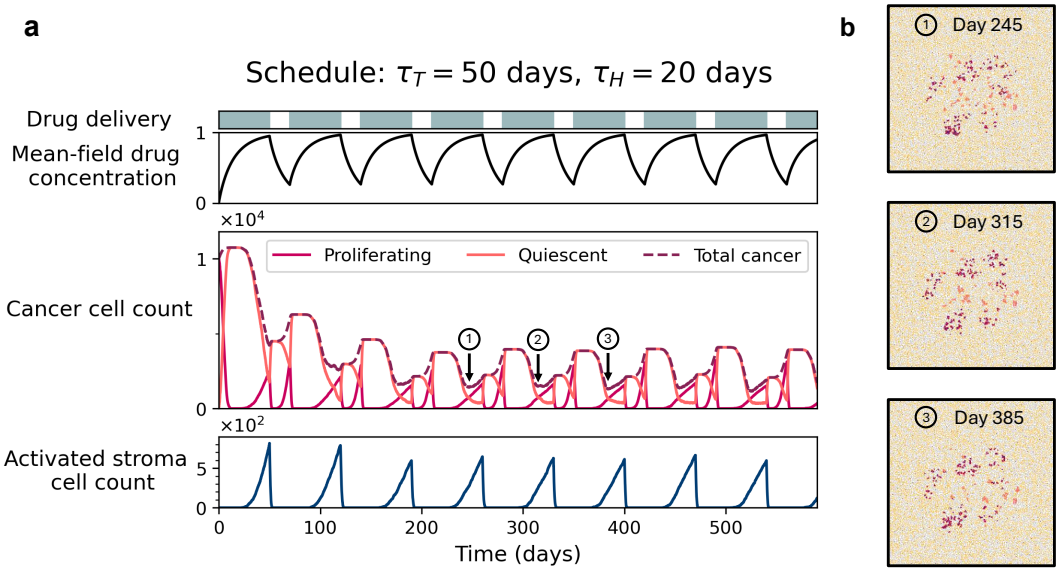

Figure 6.4: Emerging residual disease. a: Timecourse of a single representative simulation of treatment schedule $\tau_T = 50$ days and $\tau_H = 20$ days over 590 days showing drug concentration mean-field value; cancer cell populations; and activated stroma cell populations. **b:** Spatial distribution of cells at 245, 315 and 385 days, corresponding to lowest total cancer cell population in treatment cycles after the initial transient (corresponding time points in panel **a**). See Appendix E for animations of the spatial distribution, *proliferation signal* and drug concentrations for treatment regime $\tau_T = 50$ days, $\tau_H = 20$ days.

After discarding the transient window at the start of treatment ($t \in [0, 150]$ days), we quantify the longitudinal occupancy of cancer cells in Ω, over the remainder of the treatment. With this measure we determine regions in Ω where surviving cancer is located once the dynamics settle around the approximately cyclic pattern (Fig. 6.5**a**). Moreover, the longitudinal occupancy of activated stroma cells in Ω over the same time interval, reveals that the regions of high longitudinal occupancy of cancer almost always correspond to those with high longitudinal occupancy of activated stroma (Fig. 6.5**b**). This co-location points to the fact that resistance is being driven by activated stroma, that is, in these regions we observe tissue-scale EMDR at play. However, we note a small region with markedly higher longitudinal occupancy of cancer does not correspond to a region of high activated stroma. These distinct regions will be analysed and compared in Section 6.4.

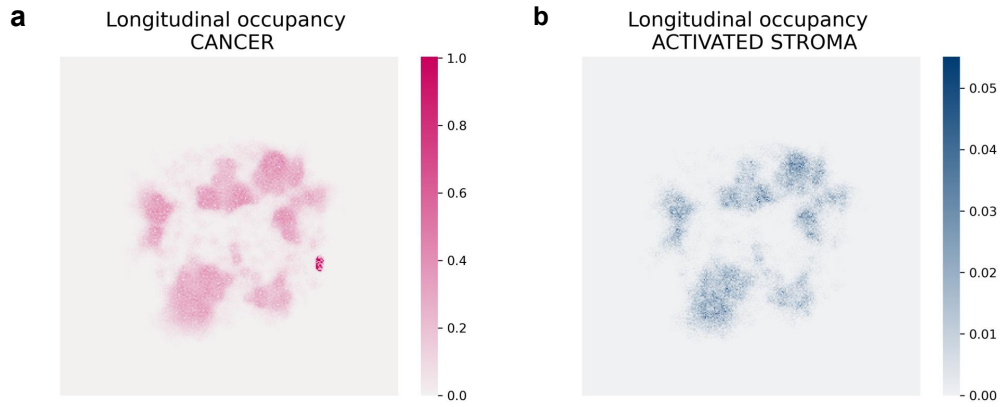

Figure 6.5: Longitudinal occupancy of residual disease and activated stroma. **a:** Longitudinal occupancy of cancer in Ω. **b**: Longitudinal occupancy of activated stroma in Ω. Longitudinal occupancy is measured as fraction of time a lattice location in the domain is occupied by the cell type of interest over 30 simulations, discarding the transient ($t \in [150, 590]$ days). Regions of high longitudinal occupancy of activated stroma are co-located with regions of high longitudinal occupancy of cancer. There is a small region of very high longitudinal occupancy of cancer that is not co-located with activated stroma.

To investigate local cell-to-cell interactions between cancer and stroma we introduce the *activation window* as the period of the treatment cycle when

activated stroma is present (Fig. 6.6**a**). This corresponds to the end of each drug delivery period when the inhibitor drug concentration has reached a level sufficient for stroma activation.

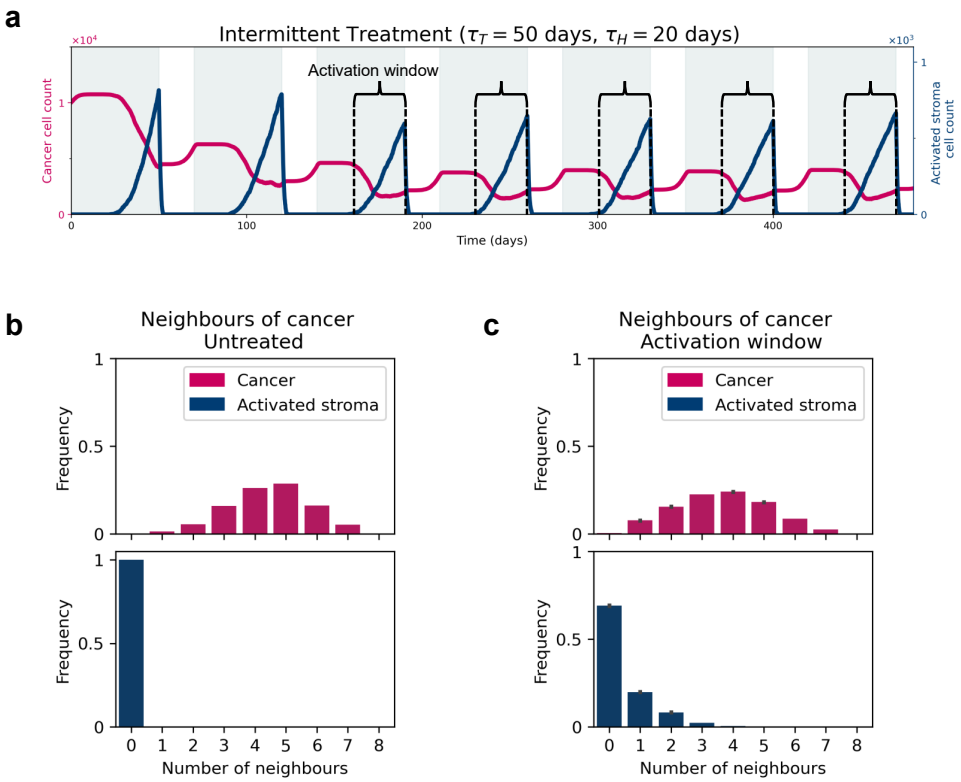

Figure 6.6: Exploration of spatial attributes of residual disease. a: Timecourse of cancer and activated stroma cell populations for a single representative simulation of treatment schedule $\tau_T = 50$ days and $\tau_H = 20$ days over 590 days. The *activation window* is shown. **b:** Cumulative distributions of number of cancer cell and activated stroma neighbours of cancer cells in the initial condition configuration. **c:** Cumulative distributions of number of cancer cell and activated stroma neighbours of cancer cells in the activation window over the same 30 simulations in Figure 6.5 with standard error shown. Here the *activation window* is the last 60% of the 50 days treatment window discarding the transient. Animations of the spatial distribution, *proliferation signal* and drug concentrations for treatment regime $\tau_T = 50$ days, $\tau_H = 20$ days are available in Appendix E.

We characterise the makeup of the neighbourhood of surviving cancer cells in the *activation window*. First, we consider the distribution of cancer cells neighbouring

a surviving cancer cell grown in the homeostatic, drug-free environment prior to treatment (i.e. for the initial condition configuration). There is a slight negative skew with an average of five cancer neighbours in their Moore neighbourhood (Fig. 6.6**b**). Next, we consider the distribution of cancer cells neighbouring a surviving cancer cell during the *activation window* and find it is approximately symmetric, with an average of four cancer neighbours in their Moore neighbourhood (Fig. 6.6**c**). There is a shift of the distribution of cancer cells neighbouring a surviving cancer cell to the left in the *activation window* compared to the initial distribution of cancer neighbours of cancer cells. With fewer cancer neighbours that provide autocrine signalling, survival of cancer depends on paracrine signalling from the TME. Analysing the distribution of activated stroma neighbours neighbouring a surviving cancer cell, during the *activation window*, shows that protection from the effects of the inhibitor drug is achieved by a small number of activated stroma neighbours that provide sufficient paracrine signalling for survival (Fig. 6.6**c**).

6.4 Survival, eradication and persistence niches

Since we observe two different patterns of residual disease, one where activated stroma is co-located with surviving cancer and the other where it is not, we move to fully characterise the TME conditions that allow for resistance to treatment to emerge. The spatial distribution of residual disease allows us to identify distinct niches in Ω. One where cancer is consistently eradicated, one where survival is driven by EMDR and another where cancer persists throughout treatment. In Figure 6.7 we show examples of an eradication niche (E), a survival niche (S) and a persistence niche (P). The concentration of the inhibitor drug builds up as it enters Ω, and a wave of cancer cell death follows (links to animations are provided in Appendix E). The survival and eradication niches both experience these dynamics of bulk death, while the persistent niche does not. Cancer cells in the persistence niche survive over the course of treatment in a quiescent state. In the survival niche, despite experiencing the wave of cancer cell death, small clusters of cancer cells escape the effect of treatment for the duration of the drug delivery window. Stroma cells can infiltrate the newly accessible space that is available as a result of the wave of cancer death albeit constrained by contact

inhibition.

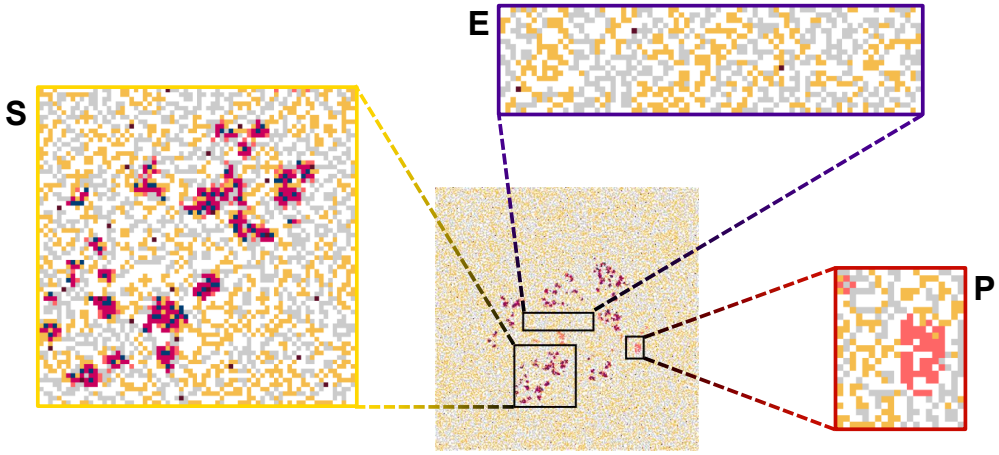

Figure 6.7: Emerging niches. Cell distribution in Ω at day 526 from a single representative simulation. There are regions where disease is eradicated and regions where disease remains. Of the regions with residual disease there are two distinct patterns. We classify these three distinct regions that emerge. The zoomed-in insets are examples of a survival niche (S), an eradication niche (E) and a persistence niche (P).

We investigate the dual (promoting and competing) nature of cancer-stroma interactions by comparing the TME conditions in the survival, eradication and persistence niches. First, we characterise cancer cell neighbourhoods over the entire treatment window for all three niches (Fig. 6.8). We find that cancer cells in the survival niche have fewer cancer neighbours and more passive stroma neighbours, than those in the eradication niche. These observations point to reduced autocrine signalling and more competition for space from passive stroma neighbours, respectively. When considering the spatial competition from reactive stroma, irrespective of activation status, a similar result is observed. A reduction in autocrine assistance and increased spatial competition are features we would intuitively associate with an eradication niche, rather than a survival niche. However, when we analyse the activated stroma neighbours of cancer cells in both these niches, it is clear that cancer cells in the survival niche

experience higher paracrine promotion over the cycles of treatment. Therefore, we find that the modulation of proliferative signal can be shifted to enable survival and growth by the paracrine stimulus to proliferation provided by activated stroma and this makes up for loss of autocrine signalling and the enhanced spatial competition. Paracrine promotion, however, does not explain the survival of cancer cells in the persistence niche where no activated stroma neighbours are present. Therefore, their survival must be explained by a different mechanism.

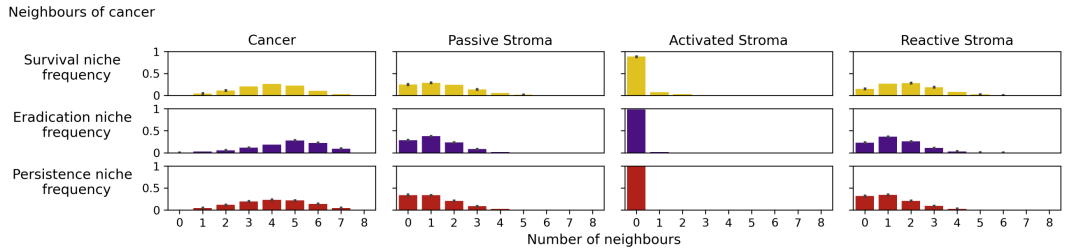

Figure 6.8: Niche characterisation of cell neighbourhoods. Distributions of different cell types of neighbours to cancer cells, over the $t \in [0, 590]$ days window, for the same 30 simulations as Figure 6.5. Distributions of average cancer, passive stroma, activated stroma and reactive stroma neighbours of cancer cells with standard errors are shown for the survival niche (yellow), the eradication niche (purple) and the persistence niche (red). The representative survival, eradication and persistence niches are the same as in Figure 6.7.

All three niches emerge from homogeneous conditions, that is, the same initial mass of cancer cells embedded in similarly reactive stromal tissue. To identify the source of the homogeneity-breaking we investigate the intermittent delivery of the inhibitor drug. Cancer cell death and the activation of reactive stroma proximal to cancer, are both induced by the build up of the drug concentration locally. This suggests that local drug concentration that is determined by the combination of the vessel distribution and the diffusion dynamics in Ω, could explain the different outcomes in each of the niches. The local drug concentration builds up quicker in regions where the density of vessels is higher than in regions where the vessel density is lower.

In order to quantify these effects, we introduce a local density measure $\rho(\mathbf{x})$

calculated on position $\mathbf{x}$ in Ω as the sum of the reciprocal exponential Euclidean distances between the position and each blood vessel site (denoted by $\hat{d}_{\mathbf{y}}(\mathbf{x})$). We have:

$$\rho(\mathbf{x}) = \frac{1}{\alpha(\mathbf{x})} \sum_{\mathbf{y} \in \mathcal{V}} e^{-\hat{\alpha} \| \hat{d}_{\mathbf{y}}(\mathbf{x}) \|}, \tag{6.1}$$

where $\hat{\alpha}$ is a constant determining the range of each vessel contribution. The normalisation term $\alpha(\mathbf{x})$ is the sum of the reciprocal exponential Euclidean distances between the position and each location in Ω such that:

$$\alpha(\mathbf{x}) = \sum_{\mathbf{y} \in \Omega} e^{-\hat{\alpha} \| \hat{d}_{\mathbf{y}}(\mathbf{x}) \|}. \tag{6.2}$$

We hypothesise that in regions of high vessel density, cancer cells experience more intense effects of the inhibitor drug yet are more likely to be rescued by activated stroma. The vessel density measure, ρ, for the given vessel distribution is shown in Figure 6.9. We observe that the region identified as the survival niche has a higher density than that of the region identified as the eradication niche, consistent with our hypothesis. At low vessel densities the local drug concentration will not build up to a level sufficient to cause cancer cell death within the drug delivery period.

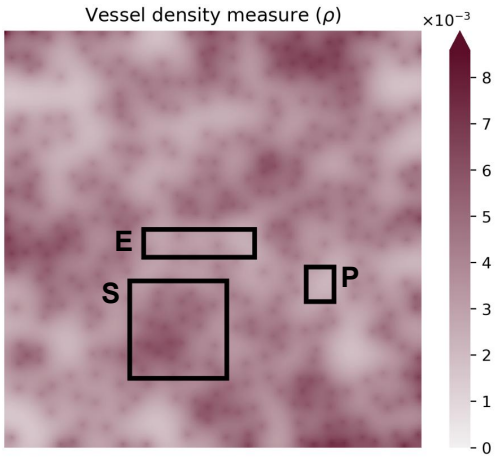

Figure 6.9: Local vessel density in the domain. Vessel density measure, $\rho(\mathbf{x})$, over Ω, for the static vessel distribution $\mathcal{V}$. Here $\hat{\alpha} = 0.1$. Boxes tracing the same regions considered in Figure 6.7, show the survival niche (S) has higher ρ values than in the eradication niche (E), while ρ values are the lowest in the persistence niche (P).

The timescale of local drug concentration build up decreases as the vessel density increases. This allows for levels of local drug concentration sufficient to kill cancer cells to occur within the drug delivery period. Eventually the vessel density will be high enough to allow for the levels of local drug concentration to reach the threshold for stomal activation with the time frame of drug delivery. The protective action of the activated stroma will unfold over the longer timescale of consecutive treatment cycles. We expect this to be a non-linear effect, however, since excessively high vessel densities will facilitate the build up of local drug concentration on a shorter timescale killing cancer cells faster than stroma can become activated. On the other hand, the build up of local drug concentration will not be sufficient to cause bulk death of cancer cells when the vessel density is extremely low. We note that the vessel density in the persistence niche is lower than the vessel density in the eradication niche (Fig. 6.9). Therefore, while we identified stromal activation as the key mechanism driving residual disease in the survival niche, residual disease in the persistence niche can be explained by low vessel density.

6.5 Vessel density driven trade-off

Further, we investigate how vessel density affects the two antithetic processes of stromal activation and cancer death during treatment by considering an experiment where we apply intermittent treatment to domains of artificially varied vessel densities. We create eight distinct domains with 50, 150, 200, 250, 300, 350, 400 and 450 vessel sites. These correspond to ρ values 0.54×10^{-3}, 1.63×10^{-3}, 2.18×10^{-3}, 2.73×10^{-3}, 3.28×10^{-3}, 3.82×10^{-3}, 4.38×10^{-3} and 4.94×10^{-3} respectively. We apply a scaling to σ_{min} and employ the circle packing algorithm for each domain to ensure adequate dispersal of vessels and avoid clustering. We then create a homogeneous bed of stroma for each domain on which a cancer cell can be placed and a tumour grown as the initial condition. We simulate a treatment regime of 50 days treatment and 20 days holiday for 200 days.

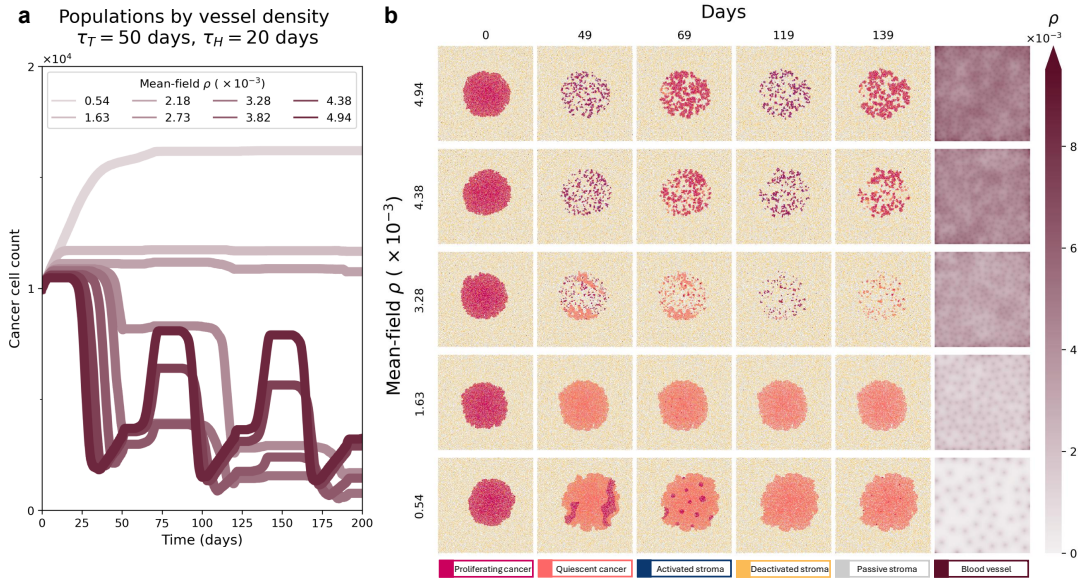

Figure 6.10: Vessel density measure investigation. a: Tumour burden for each ρ equal to 0.54×10^{-3}, 1.63×10^{-3}, 2.18×10^{-3}, 2.73×10^{-3}, 3.28×10^{-3}, 3.82×10^{-3}, 4.38×10^{-3} and 4.94×10^{-3} for 200 days. **b:** The first five columns show visualisation of cells for single representative simulations for ρ equal to 0.54×10^{-3}, 1.63×10^{-3}, 3.28×10^{-3}, 4.38×10^{-3} and 4.94×10^{-3} on day 0, 49, 69, 119 and 139. The last column shows visualisation of the vessel density measure ρ for each vessel field considered. Here $\hat{\alpha} = 0.1$. As ρ increases the spatial attributes of the treatment failure change. At lower ρ treatment failure is driven by poor perfusion where the inhibitor drug is not able to reach sufficient concentration levels to reduce the *proliferation signal* below h_d. For higher ρ, where the inhibitor drug is able to perfuse and build up in the domain, EMDR is evident where cancer survivors are clustered around activated stroma.

The tumour burden for varying ρ is shown in Figure 6.10**a**. A non-linear relationship between tumour burden and ρ is observed. Tumour burden remains high with low ρ. As less of the inhibitor drug can enter and diffuse in the domain the drug concentration does not build up sufficiently to kill the cancer cells within the drug delivery period and they persist as a mass of cancer cells in a quiescent state (Fig. 6.10**b** for visualisations of the cells). The tumour burden decreases as ρ increases until $\rho = 3.82 \times 10^{-3}$ as the increased number of vessel sites allows for more inhibitor drug to enter the diffuse in the domain, reducing the timescale of the drug concentration build up, allowing for levels sufficient to kill cancer cells. The tumour burden increases again for even higher ρ values as

the drug concentration can build up to levels above the threshold for stromal activation within the treatment delivery period driven by the increased number of vessel locations where drug enters and diffuses into the domain. As stromal activation increases, the amount of paracrine signalling provided also increases, and we observe higher tumour burden as more cancer cells are rescued during drug delivery.

To summarise our findings, we consider visualisations of the cells at a corresponding times across the simulations (Fig. 6.11).

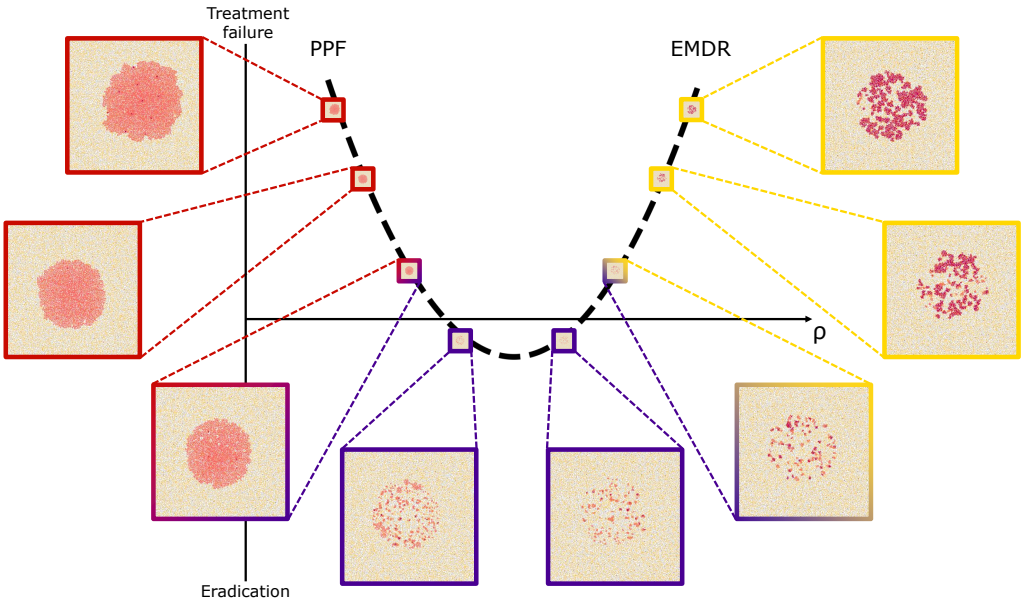

Figure 6.11: Investigation of vessel density and treatment outcomes. Distribution of cells at day 139 from single representative simulations with increasing vessel density for chosen vessel densities across the domain (the same as those selected for the experiment presented in Fig. 6.10). From the left the ρ is: 0.54×10^{-3}, 1.08×10^{-3}, 2.18×10^{-3}, 2.73×10^{-3}, 3.28×10^{-3}, 3.82×10^{-3}, 4.38×10^{-3} and 4.94×10^{-3}. Treatment failure due to poor perfusion of the drug (PPF) is evident for low vessel density, while EMDR drives treatment failure for higher vessel densities.

At low vessel densities (left insets colour-coded red), where there are fewer locations for the targeted drug to enter the domain, it is not able to sufficiently diffuse and build up throughout the domain, hence cancer cells survive. We call this type of treatment failure, poor perfusion failure (PPF). As the vessel

density increases (centre insets colour-coded purple of Fig. 6.11), the number of locations where the inhibitor drug enters Ω also increases. Allowing for more drug to diffuse and build up to levels sufficient to cause the bulk death of cancer cells but not to cause significant stromal activation. This results in the eradication of cancer cells, that is indicative of treatment success. For even higher vessel densities (right insets colour-coded yellow of Fig. 6.11), the inhibitor drug enters the domain at more locations and is able to diffuse and build up in the tissue much quicker. Stromal activation is then much more likely. The activated stroma provides the additional paracrine promotion of the *proliferation signal* that is required to rescue cancer cells, resulting in EMDR.

6.6 Drug distribution dynamics

Since a transition from PPF to EMDR is observed as the vessel density and/or drug delivery period increases we further investigate how vessel density and treatment scheduling can modulate resistance. We consider one cycle of treatment. The drug concentration builds up in Ω when the drug is delivered, with regions of high local vessel density exceeding the threshold for stromal activation, h_r, quicker than regions with low local vessel density. In Figure 6.12**a** we show a snapshot of the drug concentration field just after halfway through the drug delivery period . At this point in the treatment cycle, a significant portion of the survival niche experiences drug concentrations sufficient for stromal activation ($d(\mathbf{x}, t) \geq h_r$), whereas only a very small fraction of the eradication niche and none of the persistence niche experiences this condition. When we consider a snapshot later in the drug delivery period, all of the survival niche is now above threshold, a significant fraction of the eradication niche also has drug concentration sufficiently high for stromal activation, while in the persistence niche there is only a very small portion above threshold (Fig. 6.12**b**). We argue that residual disease in the latter is a result of low overall drug concentrations, not sufficient to kill cancer cells. While in the survival niche exposure to drug concentrations above h_r is longer. Over each drug delivery cycle there is increased stromal activation that tips the balance from the death-inducing action of the drug towards the

activation-promoting action of the drug.

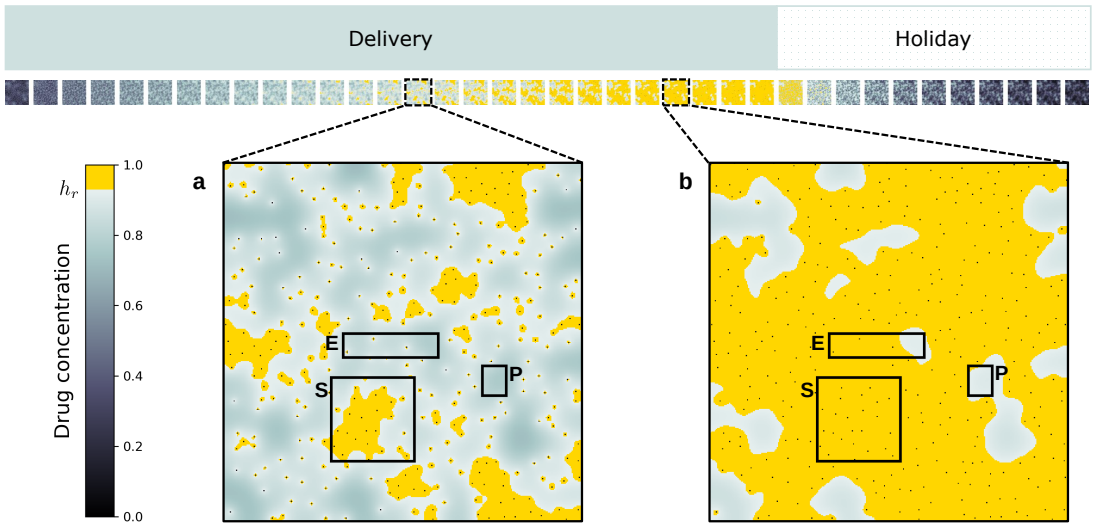

Figure 6.12: Targeted drug spatio-temporal dynamics over a treatment cycle. The drug concentration, d, for the third treatment cycle (drug delivery + holiday period). The representative survival (S), eradication (E) and persistence (P) niches are the same as in Figure 6.7 and locations where $d \geq h_r$ are highlighted in yellow. **a:** Drug concentration in the middle of the treatment period. A large fraction of the survival niche has above-threshold locations, while the eradication niche has a very low fraction and the persistence niche has no locations of above-threshold locations. **b:** Drug concentration towards the end of the drug delivery period. The entirety of the survival niche locations are above-threshold now, and a large fraction of the eradication niche. Only a very small fraction of locations in the persistence niche are above the threshold.

Since a significant fraction of locations in the survival niche experience above h_r drug concentrations for a longer time than the eradication niche the probability of stromal activation is higher in the survival niche than in the eradication niche. This agrees with the results of our activated stroma longitudinal occupancy analysis (Fig. 6.5**b**) and activated stroma neighbours analysis (Fig. 6.8). In the persistence niche, however, the much slower build up of drug concentration does not allow for the local drug concentration to reach levels sufficient to cause cancer cell death within the drug delivery period. With the

insufficient drug concentrations in the persistence niche there is less depletion of the *proliferation signal*, and the cancer cells persist throughout consecutive treatment cycles. This agrees with the results of our longitudinal occupancy of cancer analysis (Fig. 6.5**a**). Without the added paracrine promotion of the *proliferation signal* produced by activated stroma cells, cancer cells in the eradication niche are not able to survive. Conversely, survival of cancer cells in the survival niche is enabled by the additional promotion of the *proliferation signal* provided by activated stroma. This ultimately results in the emergence of EMDR.

6.7 *Proliferation signal* dynamics

We consider the first three treatment cycles of the intermittent treatment schedule ($\tau_T = 50$ days, $\tau_H = 20$ days) to investigate the cumulative effects of consecutive rounds of drug treatment cycles in shaping the *proliferation signal*, and ultimately the TME landscape which determines cell fate (survival or death) locally, and residual disease at the larger tissue scale.

At the start of the third cycle of treatment residual disease is present in all three niches (Fig. 6.13**a**). The eradication niche contains small clusters of locations where the *proliferation signal* is above the threshold for cancer cell death, h_d, but below the threshold for cancer cell proliferation, h_p. Likewise, in the persistence niche the *proliferation signal* is between h_d and h_p, albeit the locations form a bulk mass. Conversely, in the survival niche there is a bulk mass of locations where the *proliferation signal* is above the threshold for cancer cell proliferation.

When the treatment commences the drug concentration builds up quickly in the survival niche and depletes the *proliferation signal* (Fig. 6.13**b**). This results in both death of cancer cells and activation of reactive stroma cells. With the stromal activation, the *proliferation signal* rebounds sufficiently to sustain proliferation during the drug delivery period (Fig. 6.13**c**). Although *proliferation signal* levels initially drop below h_p at the start of the holiday period when the stroma deactivates, they soon increase above the threshold for proliferation again as the drug is cleared (Fig. 6.13**d**). Hence, the driver for

residual disease in the survival niche is the local paracrine promotion of the *proliferation signal*.

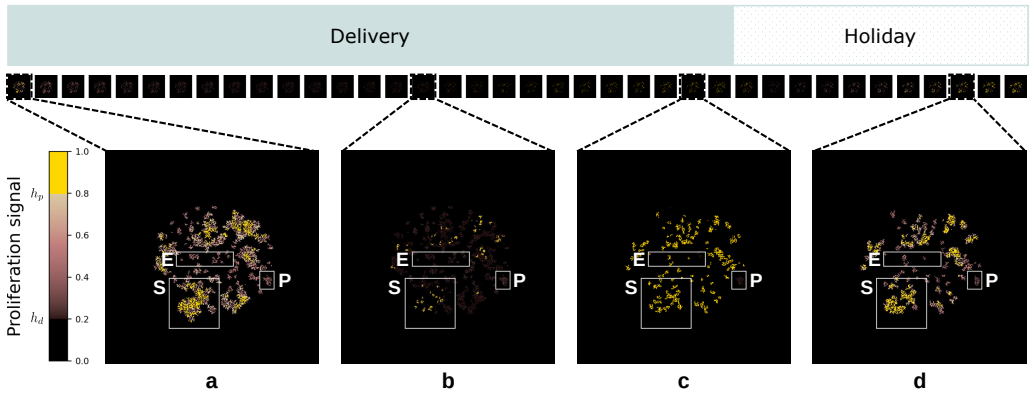

Figure 6.13: *Proliferation signal* modulation over a treatment cycle. The *proliferation signal*, p, during the third treatment cycle (drug delivery + holiday period) with yellow highlight for locations where $p \geq h_p$ and black for locations where $p < h_d$. The representative survival (S), eradication (E) and persistence (P) niches are the same as in Figure 6.7. **a:** All three niches contain locations where the *proliferation signal* is above h_d at the start of the drug delivery period. These form a bulk region in the survival and persistence niches, and small sparse clusters in the eradication niche. Locations in the proliferative window are only present in the survival niche. **b:** In the middle of the drug delivery period only a small number of locations in the survival niche remain in the proliferative window. The *proliferation signal* in the eradication and persistence niches is significantly depleted, with still no locations in the proliferative window. **c:** At the end of the drug delivery period in the survival niche the fraction of locations in the proliferative window has increased through cancer proliferation and further stroma activation. The eradication niche is almost entirely in the death window with a limited fraction of locations in the proliferation window that indicates the late activation of stroma. In the persistence niche the locations with *proliferation signal* are still in the quiescent window. **d:** In the eradication and persistence niches no locations are in the proliferative window towards the end of the drug holiday period. However, in the survival niche, the region in the proliferative window that appeared during the drug delivery period expands further, while other locations move from the death to the quiescent window.

In the eradication niche the drug concentration builds up slowly during the drug delivery period, resulting in slower depletion of the *proliferation signal* to levels below the threshold for cancer cell death, while also delaying stromal activation

(Fig. 6.13**b - c**). The slower timescale of stromal activation results in sparse clusters of cancer cells survivors, that over consecutive cycles of treatment diminish (Fig. 6.13**d**), eventually resulting in the elimination of the cancer cell population. Therefore, the cause of the successful eradication in this niche is the lack of paracrine promotion of the *proliferation signal*.

The drug diffusion dynamics are even slower in the persistence niche. This results in insufficient drug concentration levels to effectively deplete the *proliferation signal*. Only the autocrine signalling from the mass of cancer cells in this niche sustains the *proliferation signal* levels just above the threshold for cancer cell death (Fig. 6.13**b - c**). These low levels of the *proliferation signal* are maintained throughout the treatment cycle where they are slowly depleted during drug delivery and then rebound slowly during the holiday period, as some reservoir is built up (Fig. 6.13**d**). This allows the cancer cells to survive in a quiescent state. Therefore, treatment escape by dormancy is the driver for residual disease in the persistence niche. An animation of the *proliferation signal* and drug concentrations in survival, eradication and persistence niches for treatment regime $\tau_T = 50$ days, $\tau_H = 20$ days is available in Appendix E.

6.8 Discussion

In this chapter we showed our model captures the dynamics of EMDR, including the initial response to treatment followed by the resurgence of disease [8, 72, 250, 251]. With our model we exploited the reversibility of stroma response to modulate tumour burden by introducing breaks in treatment. Removal of the paracrine signalling during treatment breaks allowed for the TME to normalise and when treatment was started again some additional success was achieved with the same drug. Over consecutive cycles of treatment, heterogeneous TME conditions resulted in different local outcomes and shaped residual disease.

Our extensive investigation of cell-scale interactions in response to the molecular scale dynamics allowed us to characterise niches where cancer was eradicated and those where cancer survived. We found a non-linear relationship between

vessel density and treatment outcome, where treatment failed for both low vessel densities and high vessel densities, and was successful for intermediate vessel densities. Different patterns of residual disease emerged, for low vessel densities, cancer cells survived as a bulk mass in a quiescent state. Whereas, in high vessel densities, cancer cell survival depended on the additional paracrine signalling provided by activated stroma. This resulted in clusters of proliferating cancer cells infiltrated by activated stroma.

Residual disease was formed via two distinct mechanisms, dormancy and local paracrine promotion being at the heart of the persistence and survival niches, respectively. Vessel density and treatment scheduling both affected the diffusion dynamics of the molecularly targeted drug, which in turn affected the dynamics of the *proliferation signal*, and, ultimately, treatment response and resulting residual disease.

Recent experimental results suggest that there is no activation/deactivation process and instead protection is provided by the spatial structure of the stroma [7, 215]. In Chapter 7 we present an alternative model where stromal activation is omitted and instead we assume that during therapy CAFs offer a protective niche for cancer cells.

Chapter 7

A Model of Stroma Proximity-Dependent Mechanisms of Protection in Environmentally Mediated Drug Resistance

In the model we presented in Chapter 4, cancer cells received protection from stroma following an activation process (stroma-activation dependent model). Our model assumption, based on results of an *in-vitro* experiment that suggested therapy-triggered stroma derived protection for a population with some prior level of differentiation [10], is intended to capture therapy-triggered rescue driven by the TME. The mechanisms by which the TME mediates resistance are complex, multifactorial and not fully understood. Ongoing research is attempting to navigate the complexity and unpick the processes that lead to the emergence of EMDR. Recent experimental results have shed light on the mechanisms of resistance driven by the microenvironment. The study by Desai *et al.* suggests that stroma activation is not necessary for protection but rather the stroma itself offers structural protection [7]. These results provide the motivation for us to explore an alternative hypothesis for the potential mechanism of EMDR, proximity dependent protection. We introduce a new

variant of our model where we assume stroma driven rescue does not depend on stromal activation but rather on the protective capacity of stroma (stroma-proximity dependent model).

7.1 Model definition

Our new model modifies compartments of the stroma-activation dependent model we describe in Chapter 4. As stromal protection does not depend on activation of stroma, reactive stroma does not switch between activated and deactivated states. We now refer to reactive stroma as fibroblasts, F, and all other non-cancer cells in the TME as inactivated, I (i.e. the same as passive cells in the original model presented in Chapter 4). Cancer cell viability and proliferative status still depend on the local *proliferation signal* intensity, p, however, cancer cells can now be in one of two states, protected, P, or non-protected, N. Proximity to fibroblasts can provide protection from the effects of the inhibitor drug. A cancer cell that is sufficiently close to a fibroblast can transition from a non-protected to a protected state, with probability p_R, in response to local TME conditions (sufficiently high drug concentration to trigger stress a response, i.e. above h_r). We introduce a stromal protection measure $d_s > 0$, that corresponds to the maximum distance over which a fibroblast can exert protective effects. Namely, this measure determines the size of the Moore neighbourhood of a cancer cell that is used to detect a fibroblast that can offer protection.

All cancer cells still provide autocrine promotion of the *proliferation signal* at rate β, however a protected cancer cell provides additional promotion at a rate γ (similar to the additional paracrine signalling provided by the activated stroma in the stroma-activation dependent model). The PDE governing the *proliferation signal* is modified and becomes:

$$\frac{\partial p}{\partial t} = (\beta + \gamma r(\mathbf{x}, t))\, H(1-p) s(\mathbf{x}, t) - \delta d p, \tag{7.1}$$

where $\mathcal{P}_t$ is the set of protected cancer cells:

$$r(\mathbf{x}, t) = \begin{cases} 1 & \text{if } \mathbf{x} \in \mathcal{P}_t, \\ 0 & \text{otherwise.} \end{cases} \tag{7.2}$$

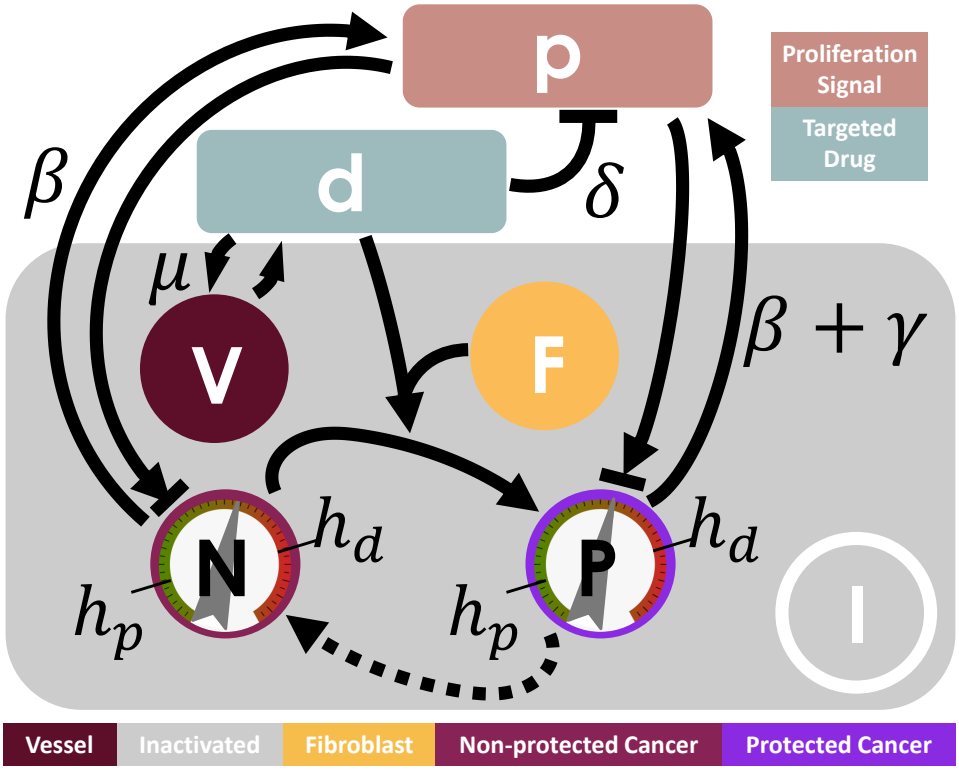

Figure 7.1: Key interactions between cancer cells and the TME assumed in the stroma-proximity dependent model. TME comprises of fibroblast cells, F, and inactivated cells, I. Fibroblast cells can provide protection for a cancer cells during therapy. A targeted inhibitor drug, d, enters the system at maximal concentration and is removed at rate μ through vessel sites V. Cancer cells can be either non-protected, N, or protected, P, depending on the local concentration of the targeted drug (above threshold h_r) and proximity to a fibroblast cell. Protected cancer cells revert to a non-protected state if the drug concentration falls below h_r or it is no longer within sufficient proximity to a fibroblast. Cancer cell, behaviour is dependent on the local concentration of the *proliferation signal*, p, with thresholds for death, h_d, and proliferation, h_p. All cancer cells provide autocrine promotion of local *proliferation signal* at rate β. Protected cancer cells provide addition promotion of the local *proliferation signal* at rate γ. The *proliferation signal* is depleted by the inhibitor drug at rate δ.

We initiate stroma cells randomly as either fibroblast or inactive cell type according to a fixed proportion $\pi \in [0, 1]$, where $\pi = 0$ corresponds to all the stroma being inactive and $\pi = 1$ corresponds to all the stroma being fibroblasts. All other components of the model are the same as the stroma-activation dependent model. Where applicable, we use our previously calibrated parameter values as described in Chapter 5 (Tables 5.1 and 5.2 for the relevant parameter choices). Specifically, it is still appropriate for us to use our parameter choices for h_d, h_p and our previously experimentally calibrated values of p_0, β, γ and δ (Chapter 5 and Table 5.3). We use the experimentally calibrated value $d_s = 45$ μm as our measure of protection for the fibroblasts in the model [7]. We use the initial condition configuration as presented in Section 4.4.

All newly defined model parameters are presented in Table 7.1.

Param.	Description	Value	Reference
d_s	fibroblast measure of protection	45 μm	[7]
h_r	inhibitor drug threshold for cancer protection	0.93	Model specific
p_R	cancer cell protection probability	0.002 day^{-1}	Model specific
π	stroma abundance	0.5	Model specific

Table 7.1: Model parameters introduced for the stroma-proximity dependent model. Distance measure of fibroblast protection is taken from experimental data. Other parameter values are chosen specific to our model.

7.2 Treatment scheduling

With the stroma-proximity dependent model we scan the treatment schedule landscape, considering the outcomes of multiple replicates of different treatment regimes with $\tau_T = \{0, 10, 20, 30, 40, 50, 60, 70, 80, 90, 100\}$ days and $\tau_H = 20$ days over 590 days of therapy. First, we quantitatively consider the trade-off between

reduction of tumour burden and duration of pharmaceutical intervention. We observe a non-linear correspondence between τ_T and relative tumour burden (Fig. 7.2**a**). Consistent with our previous results, we observe a reduction in relative tumour burden as τ_T increases until $\tau_T = 50$ days. At this point we see an increase in relative tumour burden as the drug delivery window lengthens.

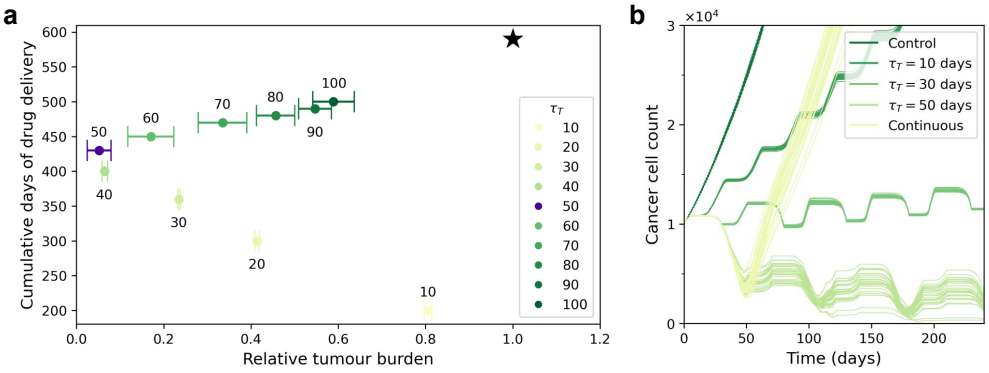

Figure 7.2: Intermittent treatment regime analysis for the stroma-proximity dependent model. a: Cumulative days of drug delivery (measured as the sum of drug delivery days over 590 days of therapy) against relative tumour burden (measured as the sum of total cancer cell count over the $t \in [0, 590]$ day window normalised to the continuous treatment case) for $\tau_T = \{10, 20, 30, 40, 50, 60, 70, 80, 90, 100\}$ days for $\tau_H = 20$ days. Results show the average of 30 simulations of each schedule and includes 95% confidence intervals. The star indicates measures for continuous treatment. Relative tumour burden initially decreases as cumulative days of drug delivery increases, but from $\tau_T = 50$ days the relative tumour burden increases. **b:** Tumour burden for $t \in [0, 240]$ days under no treatment, continuous treatment, and five intermittent treatment schedules ($\tau_T = \{10, 30, 50\}$ days and $\tau_H = 20$ days). Individual realisations are shown, with 30 stochastic simulations conducted for both untreated and treated conditions. As the length of the treatment period τ_T of intermittent treatment increases a reduction in tumour burden is observed.

Examples of the resulting tumour burden for varying lengths of τ_T are shown in Figure 7.2**b**. We observe that with short treatment periods ($\tau_T = 10$ days) tumour growth continues as the drug concentration in the domain is not sufficient to cause cancer cell death. As τ_T increases, some form of tumour burden control is achieved and for $\tau_T = 50$ days low levels of tumour burden are maintained.

7.3 Patterns of residual disease

We explore the intermittent treatment schedules where $\tau_T = \{40, 50, 60\}$ days and $\tau_H = 20$ days, where some degree of tumour burden maintenance is achieved (Fig. 7.2 and Fig. 7.3**a**). Each of the intermittent schedules have different patterns of residual disease at the end of their third drug delivery period. For $\tau_T = 40$ days the drug concentration does not build up sufficiently in some regions of the domain to cause bulk death of cancer cells within the drug delivery window. We observe densely packed non-protected cancer cells in these regions. Where the drug concentration builds up sufficiently to cause cancer cell death and trigger protection, we observe a small region of protected cancer cells (Fig. 7.3**b**).

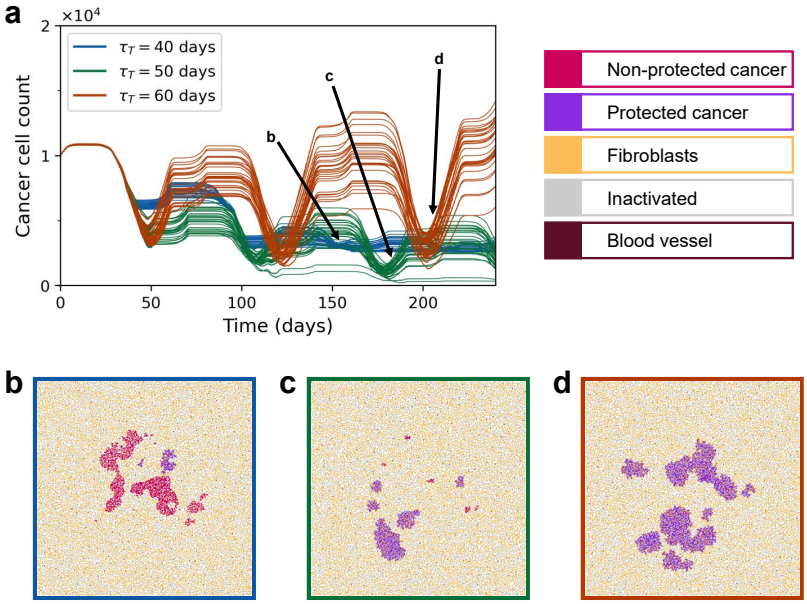

Figure 7.3: Comparison of low levels of residual disease in the stroma-proximity dependent model. a: Tumour burden for $t \in [0, 240]$ days under three intermittent treatment schedules ($\tau_T = \{40, 50, 60\}$ days and $\tau_H = 20$ days). Individual realisations are shown, with 30 stochastic simulations conducted for both untreated and treated conditions. **b - d** show the spatial distribution at representative time points for a single simulation of the treatment regime of interest. **b:** Day 157 of intermittent treatment ($\tau_T = 40$ days, $\tau_H = 20$ days). **c:** Day 183 of intermittent treatment ($\tau_T = 50$ days, $\tau_H = 20$ days). **d:** Day 209 of intermittent treatment ($\tau_T = 60$ days, $\tau_H = 20$ days).

As the drug delivery window increases to $\tau_T = 50$ days there are only a few small clusters of non-protected cancer cells and larger clusters of protected cancer cells (Fig. 7.3**c**). For this intermittent treatment regime, the timescale of protection does not allow for significant residual disease to occur during the drug delivery window and over successive drug delivery cycles the tumour burden slowly decreases. For $\tau_T = 60$ days there are much larger clusters of protected cancer cells and no remaining non-protected cancer cells (Fig. 7.3**d**). The extended period of drug delivery allows for the drug concentration to build up to levels sufficient to cause bulk cancer death and extending the time cancer cells spend under protection, resulting in more residual disease at the end of each drug delivery window. Over successive treatment cycles tumour burden increases, and treatment fails.

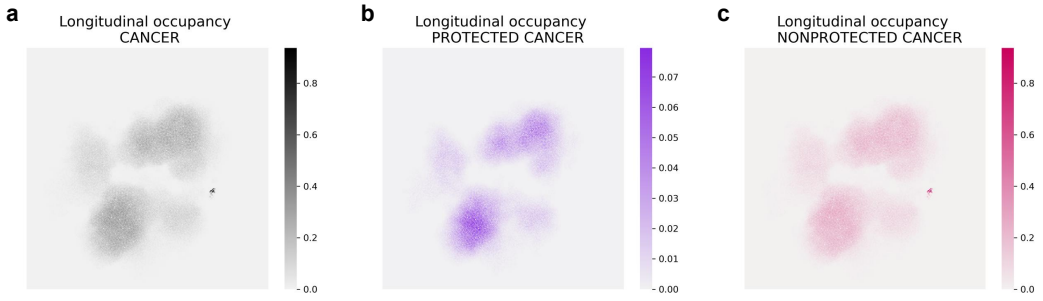

Figure 7.4: Longitudinal occupancy of residual disease in the stroma-proximity dependent model. a: Longitudinal occupancy of cancer cells in Ω. **b:** Longitudinal occupancy of protected cancer cells in Ω. **c:** Longitudinal occupancy of non-protected cancer cells in Ω. Longitudinal occupancy is measured as fraction of time a lattice location in the domain is occupied by the cell type of interest over 30 simulations, discarding the transient window ($t \in [150, 590]$ days). Regions of high longitudinal occupancy of protected cancer cells are co-located with regions of high longitudinal occupancy of cancer, suggesting that residual disease can be explained by stromal protection. Of note is the small region of very high longitudinal occupancy of cancer that remains non-protected throughout treatment.

In Figure 7.4 we consider the longitudinal occupancy of cancer cells in Ω, over $t \in [150, 590]$ (discarding the transient window). This measure allows us to determine the regions in Ω where surviving cancer is located once the cyclic pattern in the dynamics is reached (Fig. 7.4**a**). The location of surviving cancer

is very similar to that of the stroma-activation dependent model. Since the vessel distribution is the same in both models, cancer surviving in similar locations suggests that the drug diffusion dynamics also play a crucial role in the stroma-proximity dependent model (Fig. 6.5**a**). When we consider the longitudinal occupancy for protected and non-protected cancer cells separately (Fig. 7.4**b** and Fig. 7.4**c**, respectively), a small region where cancer cells survive without stromal protection is revealed. This region corresponds to the persistence niche identified in the stroma-activation dependent model (Chapter 6) where residual disease results from PPF due to the low vessel density of the region. Our results here indicate that again, for this region, PPF is responsible for residual disease rather than environmentally mediated protection (Section 6.4 and Fig.6.7).

7.4 Stroma abundance and dispersal factor in treatment response

It is generally accepted that across different types of cancer high stroma-to-tumour ratio is associated with poor prognosis and a diminished response to treatment [43, 215, 252, 253]. Mechanisms such as upregulation of ECM and paracrine signalling, driven by the stroma, contribute to therapy resistance. However, it is not clear to what extent these phenomena contribute and account for the observed heterogeneity in treatment responses. A recent *in-silico* study has identified stromal dispersion as a potential feature of TME composition that can affect EMDR [215]. With our stroma-proximity dependent model, we set about to test the hypothesis that there is an association between stromal dispersion and treatment response.

To allow for fibroblast configurations with varying dispersions we introduce a clustering parameter, c_d. When the non-cancer cells are initiated, they are assigned the inactivated cell type. The number of fibroblast clusters is calculated by dividing the proportion π of the initial non-cancer cell count by c_d. A circle packing algorithm is used to determine the centre of each fibroblast cluster and then all inactivated cells within the Moore neighbourhood of size c_d of the centre (including the centre) is assigned the fibroblast cell type. Initial

configurations with fibroblast clusters of varying values of c_d are shown in Figure 7.5. For low values of c_d fibroblasts are more dispersed (Fig. 7.5**a**) and as c_d increases fibroblasts become less dispersed and form larger clusters (Fig. 7.5**b - c**).

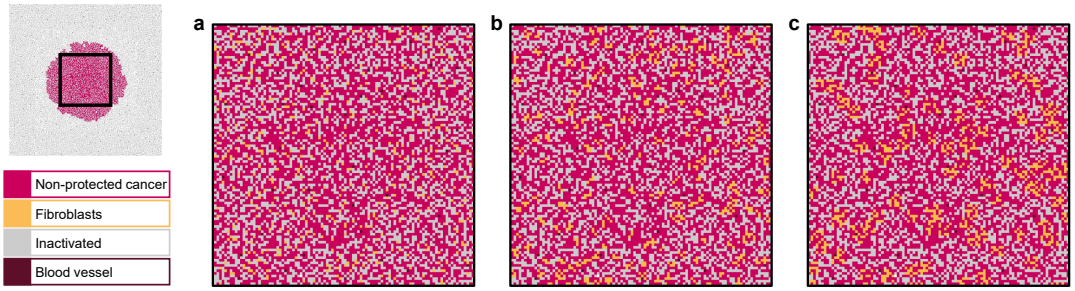

Figure 7.5: Fibroblast dispersal in the initial configuration. Spatial distribution of the initial configuration for different values of c_d for $\pi = 0.5$. We show a zoomed-in central subset of Ω for different values of c_d. Fibroblast dispersal decreases and the size of the clusters increase as c_d increases. **a:** $c_d = 3$, **b:** $c_d = 5$, and **c:** $c_d = 7$.

We consider three different fibroblast proportions ($\pi = \{0.4, 0.5, 0.6\}$) with three different levels of clustering ($c_d = \{3, 5, 7\}$). As the stroma abundance in Ω increases, the amount of residual disease also increases and the time to disease resurgence decreases (Fig 7.6). With more fibroblasts that offer protection, more cancer cells survive the treatment in a protected state and there are a larger number of potential protective niches that protected cancer cells can proliferate into. This results in overall higher amounts of residual disease and a reduction in the time to disease resurgence (Fig. 7.6).

Conversely, as the level of clustering of the fibroblasts in Ω increases, the time to disease resurgence also increases (Fig. 7.6). When the fibroblasts are more dispersed there is less overlap between each fibroblasts Moore neighbourhood of protection than when the fibroblasts are clustered together. Less overlap provides more locations where cancer can be protected and results in overall larger amounts of residual disease and a reduced time to disease resurgence. When fibroblasts are more clustered, more overlap results in fewer locations where cancer can receive

protection during therapy. This results in an improved response to therapy with lower levels of residual disease and increased times to disease relapse.

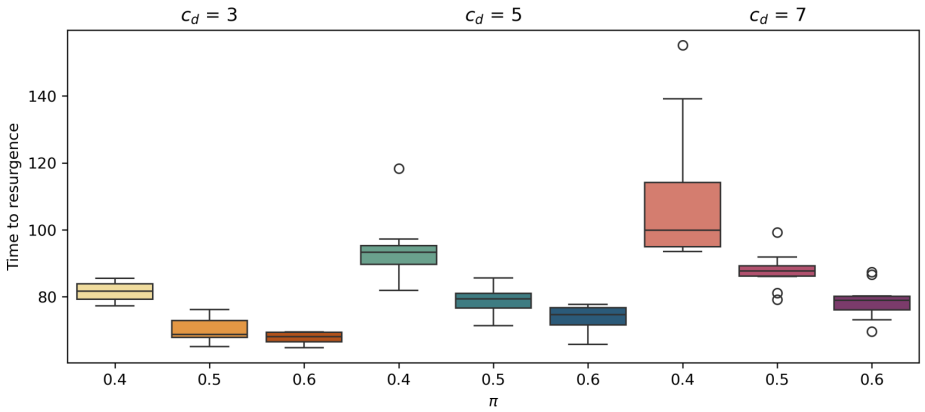

Figure 7.6: Stromal abundance and dispersal effects on treatment outcome. Time to resurgence (measured as the time till cancer cell count reaches the initial value of 10^4 cells following disease progression) for three different fibroblast proportions $\pi = \{0.4, 0.5, 0.6\}$ and three different clustering sizes $c_d = \{3, 5, 7\}$ for 150 days of continuous treatment. As the stroma abundance increases the time to resurgence decreases. Conversely, as the cluster size increases the time to resurgence increases. Data from ten simulations of each combination of fibroblast proportion and clustering size is shown. In the boxplots, the centre line is the median; box limits are the upper and lower quartiles; whiskers are $\pm 1.5 \times$ IQR; and outliers are represented by a circle.

Our results indicate that stromal dispersion can influence levels of residual disease and response to therapy. In tissue where CAFs (fibroblasts, F) are sufficiently abundant to drive EMDR, a more dispersed CAF population provides a larger protective niche, resulting in larger amounts of residual disease. Larger amounts of residual disease reduce the time to disease resurgence. Alongside the contribution of the stroma/tumour ratio, stromal dispersion is a crucial factor that can drive EMDR and affect therapy outcomes.

7.5 Discussion

In this chapter we introduced a variation of the model we presented in Chapter 4 (stroma-activation dependent model). This variant has an alternative

mechanism of EMDR that we implemented in response to recent experimental results [7]. This new model captured EMDR at the tissue scale driven by stroma-proximity dependent mechanisms in response to local TME conditions. While the diffusion dynamics of the molecularly targeted drug, determined by the vessel density and treatment scheduling, still played a crucial role in the response to treatment, it was but one of the features of TME-mediated resistance. Here we investigated the relationship between stroma abundance, stroma dispersal and response to treatment. We found that stroma dispersal affected treatment response, with greater dispersal resulting in larger amounts of residual disease and a reduced time to disease resurgence. Our results agreed with a recent *in-silico* study [215]. EMDR is only one component of resistance to therapy. Cell-based resistance is another important component. In Chapter 8 we relax the assumption of phenotypic homogeneity in cancer cells' response to local TME cues and investigate the emerging phenotypic variation in response to treatment.

Chapter 8

Integrating Cell-based and Environmentally Mediated Drug Resistances: the Role Microenvironment Conditions Play in Shaping Phenotypic Variation and Residual Disease

In Chapters 6 and 7 we investigated the contribution to resistance mediated by the TME. We show that residual disease can emerge during therapy, driven by tumour-stroma interactions. The drug diffusion dynamics play a crucial role in location and shape of the residual disease (Sections 6.6 and 7.3). We find introducing breaks in therapy results in some modulation of the disease burden (Sections 6.2 and 7.2). Although it is an important factor in the formation of residual disease, particularly at the onset of treatment, EMDR is only one component of resistance. Cell-based mechanisms also contribute to the development of resistance, and ultimately treatment failure.

For our investigation of EMDR we assumed a homogeneous population of cancer cells. This allowed us to focus on the contribution to resistance driven by the TME only. However, tumours are not a mass of homogeneous cancer cells but are comprised of a population of cancer cells that is genotypically and phenotypically diverse. Over time these populations evolve, responding to intrinsic and extrinsic factors, undergoing various genetic and epigenetic modifications that contribute to the development of residual disease and ultimately disease relapse, [37, 46, 78].

Here, we combine TME-driven mechanisms (described in Chapter 7) with cell-based mechanisms of acquired resistance and investigate the residual disease that emerges and eventually leads to treatment failure. We extend the stroma-proximity dependent model by incorporating a framework for cancer cell heterogeneity via a phenotypic landscape. With our phenotypic landscape we can capture multiple drug-tolerant states as a path to stable resistance.

8.1 Phenotypic landscape

In the current modelling setup, cancer cell viability and behaviour are determined by local *proliferation signal* intensity, according to two thresholds, h_d and h_p. The threshold for death (h_d) represents the lowest amount of local pro-growth signalling at which a cancer cell can remain viable, whereas the threshold for proliferation (h_p) represents the minimum amount of local pro-growth signalling that a cancer cell must sense in order to divide. We model phenotypic heterogeneity within the cancer cell population whereby individual cancer cells respond to local signalling cues differently, mimicking upregulation/downregulation of cell-surface receptors that distort environmental signalling intensity perception. We achieve this by allowing for potential variation of these thresholds. At cell division we allow an incremental change of Δr to each new cancer cells h_d and h_p with probability p_m.

With lower values of h_d, cancer cells can survive in environments with lower amounts of *proliferation signal*, making them more able to tolerate the effects of treatment for longer. Cancer cells with very low h_d and high h_p can survive treatment albeit in a quiescent state. These cells display the traits associated with

drug-tolerant cells (DTPs). A cancer cell with $h_d = 0$ is completely resistant and will persist throughout treatment. Conversely, higher values of h_d mean cancer cells are less able to withstand the effects of therapy and will die sooner.

For higher values of h_p, cancer cells require higher levels of local pro-growth signalling to proliferate, while cancer cells with lower values of h_p can divide despite lower local accumulation of *proliferation signal*. Cancer cells with very low h_p (and subsequently very low h_d) can proliferate in local conditions with very little *proliferation signal* and can potentially proliferate during therapy. These cells display the traits associated with drug-resistant cells.

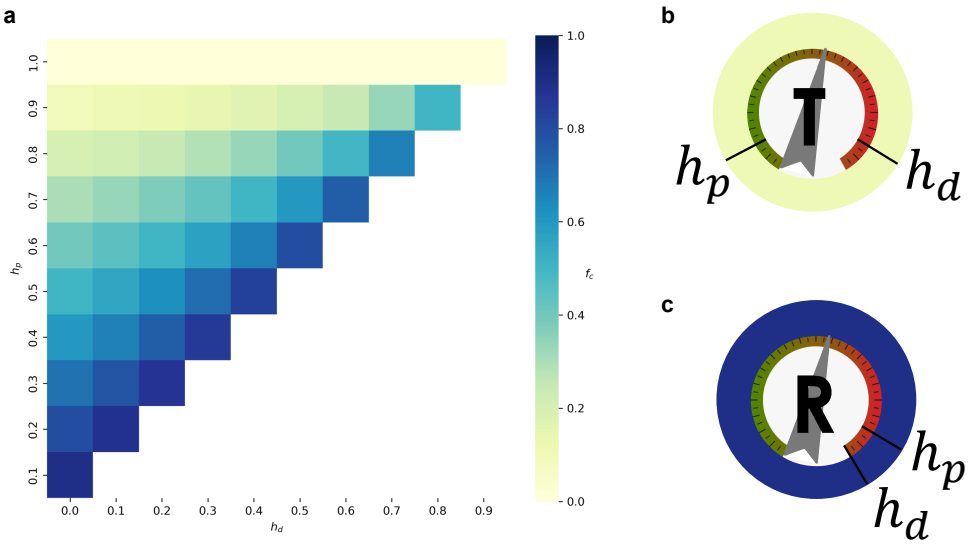

Figure 8.1: Fitness measure f_c as a function of h_d and h_p. a: Phenotypic landscape of cancer cells. Cancer cells with larger *quiescent windows* than *proliferative windows* (low values of f_c) are located towards the top left. These cells have lower h_d and higher h_p. Cancer cells with larger *proliferative windows* than *quiescent windows* (high values of f_c) are located towards the lower left. These cells have lower h_d and h_p. **b:** Representative cancer cell for phenotype with low f_c value. This cell has $h_d = 0.1$ and $h_p = 0.9$. Although this cell can tolerate drug treatment for longer than the initial phenotype, it does so in a quiescent state and can only proliferate in conditions where the local accumulation of *proliferation signal* is high (drug-tolerant phenotype). **c:** Representative cancer cell for phenotype with high f_c value. This cell has $h_d = 0$ and $h_p = 0.1$. This cell is drug tolerant and can proliferate in conditions where the local accumulation of *proliferation signal* is very low (drug-resistant phenotype).

We introduce a measure, f_c, that, for each cancer cell, is the fraction of its *proliferative window* over the *alive window* (quiescent + proliferative). We have:

$$f_c = \frac{1 - h_p}{1 - h_d}. \tag{8.1}$$

We show the phenotypic landscape in Figure 8.1**a**. Cancer cells that have low f_c have smaller *proliferative windows* and larger *quiescent windows*, we call drug-tolerant (Fig. 8.1**b**), while cancer cells with high f_c have a larger *proliferative windows* and smaller *quiescent windows*, we call drug-resistant (Fig. 8.1**c**).

8.2 Cost of phenotypic variation

We consider a trade-off for a cancer cell when it changes its phenotype. We assume an increase in cancer cell fitness, by either the increasing capacity to evade apoptosis (reducing h_d), or gaining greater proliferative potential (reducing h_p), comes with an associated cost [79, 81, 250, 254]. In a drug-naive tumour, the cost of resistance contains the expansion of resistant cells, which are outcompeted by their less resistant counterparts. Local TME conditions change during therapy, and these changes can result in different competition outcomes. Cells that are sensitive to therapy are mostly eliminated, reducing the competition for resistant cell population. Studies have shown that cancer cells that persist during therapy are either quiescent or slow cycling [73, 255]. We implement the cost of resistance by modifying the time it takes for a cancer cell to complete the cell cycle.

Let C_r be the cost multiplier applied to each individual cancer cells intermitotic time (I). We aim for cancer cells with the greatest proliferative potential, that is cancer cells with lowest h_d and h_p, to have the highest cost ($C_{max} > 1$). Conversely, the cancer cells with the least proliferative potential, those with highest h_d and h_p, are assigned the lowest cost ($C_{min} < 1$). For fixed h_d the cost decreases as h_p increases and for fixed h_p the cost decreases as h_d increases.

We let:

$$C_r = \frac{D}{(h_d + A)(h_p + A)}, \tag{8.2}$$

where A and D are constants to be found and $A, D > 0$. In Figure 8.2 we show the cost of resistance (C_r) over the phenotypic landscape.

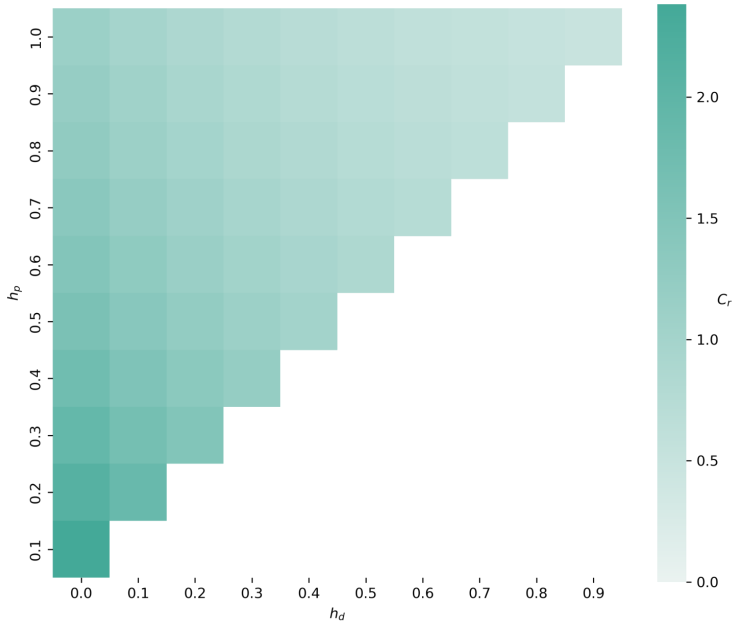

Figure 8.2: Cost as a function of h_d and h_p. We visualise the cost of resistance over the phenotypic landscape. Cancer cells with high h_d and h_p have the the shortest cell cycle. The cancer cells with the longest cell cycle are those with low h_d and h_p. For each h_d the cell cycle length decreases as h_p increases. For each h_p the cell cycle decreases as h_d increases. Cells with phenotypes better able to resist the effects of the drug have a longer cell cycles.

8.3 Calibration of parameters

To calibrate the cost we determine A, D (Eq. 8.2). We assume the initial cancer cell has thresholds $\hat{h_d}$ and $\hat{h_p}$ and no cost, that is $c_{init} = 1$. We use baseline values $\hat{h_d} = 0.2$ and $\hat{h_p} = 0.8$, corresponding to the phenotype of all cancer cells in the initial condition configuration which has been constructed in the homogeneous

case (Section 4.4). From Equation 8.2 we get:

$$1 = \frac{D}{(\hat{h_d} + A)(\hat{h_p} + A)} \implies D = (\hat{h_d} + A)(\hat{h_p} + A). \tag{8.3}$$

The cells with the lowest cost, $C_{min} < 1$, are cancer cells with the highest values of h_d and h_p. This phenotype has thresholds $h_d = 1 - \Delta r$ and $h_p = 1$. From Equation 8.2 we get:

$$C_{min} = \frac{D}{(1 - \Delta r + A)(1 + A)}. \tag{8.4}$$

We substitute the result of Equation 8.3 into Equation 8.4 to get:

$$C_{min} = \frac{(\hat{h_d} + A)(\hat{h_p} + A)}{(1 - \Delta r + A)(1 + A)}, \tag{8.5}$$

that we can write as a polynomial equation of degree two as follows:

$$(1 - C_{min})A^2 + (\hat{h_d} + \hat{h_p} + C_{min}(\Delta r - 2))A + \hat{h_d}\hat{h_p} + C_{min}(\Delta r - 1) = 0. \tag{8.6}$$

The value of A is a solution of Equation 8.6. For solutions to exist there are restrictions on the value of Δr. The details of these restrictions are presented in Appendix F.

While individual mechanisms that mediate cell-based resistance are known, how these come together *in-vivo* and progress along a resistance continuum is not fully understood [7, 211, 256]. Hence, we arbitrarily choose values of Δr and p_m while ensuring our choice of Δr complies with the restrictions we discuss in Appendix F.

The cells with the lowest values of h_d and h_p have the highest cost, C_{max}. This phenotype has thresholds $h_d = 0$ and $h_p = \Delta r$. We can determine the value of C_{max} using Equation 8.2, the result of Equation 8.3, and the calibrated value of

A. Our value of C_{max} agrees with *in-vitro* experimental data for melanoma cells undergoing targeted therapy [257].

Param.	Description	Value	Reference
c_d	clustering value	7	Model specific
Δr	phenotypic shift increment	0.1	Model specific abiding by the restrictions outlined in Appendix F
p_m	phenotypic shift probability	0.6	Model specific
$\hat{h_d}$	initial cancer cell threshold for death	0.2	Model specific
$\hat{h_p}$	initial cancer cell threshold for proliferation	0.8	Model specific
C_{init}	initial cancer cell cost multiplier	1	Model specific
C_{min}	cost multiplier of cancer cell with lowest f_c	0.5	(BNID 103994) [258]
A	cost parameter	$\frac{-1+\sqrt{233}}{20}$	Eq. 8.6
D	cost parameter	$\frac{139+9\sqrt{233}}{200}$	Eq. 8.3 with values h_d, h_p and A
C_{max}	cost multiplier of cancer cell with highest f_c	$\frac{139+9\sqrt{233}}{116}$	Eq. 8.2 with values h_d, h_p, A and D

Table 8.1: Model parameters associated with the incorporation of the cancer cell phenotypic landscape. Threshold and initial cost parameter values are chosen specific to our model. Experimental data informs the parameter value for the minimum cell cycle length from which the remaining parameter value associated with the cost are derived. All other parameter values are chosen specific to our model.

To allow for resistance to emerge via phenotypic variation we choose a higher clustering value (c_d), delaying the time to resurgence driven by EMDR. For all other model parameters, we choose our previously calibrated values (Tables 5.1 - 5.3 and Table 7.1). The newly defined model parameters are presented in Table 8.1.

8.4 Investigation of basic competition dynamics between phenotypes

We initially want to observe and evaluate the competition dynamics between two phenotypes, a sensitive type with a low f_c value ($h_d = 0.1$ and $h_p = 0.9$), we call the drug-tolerant phenotype (Fig. 8.1**b**), and the other resistant type with a high value of f_c ($h_d = 0$ and $h_p = 0.1$), we call the drug-resistant phenotype (Fig. 8.1**c**). We consider a small experiment, analogous to a scratch assay, to investigate competition dynamics between cells in the absence of cost of resistance, compared to dynamics when a cost of resistance is introduced. We consider these dynamics in three environments with homogeneous *proliferation signal* values at different values ($p = \{0.05, 0.6, 1\}$). On a 100×100 square lattice we construct the initial condition of our *in-silico* scratch assay by initialising 10×100 drug-tolerant cells, T, adjacent to the left boundary and 10×100 drug-resistant cells, R, adjacent to the right boundary.

When $p = 0.05$, for both the no cost and cost scenarios, the drug-tolerant phenotype die as the value of the *proliferation signal* is not sufficient for survival and the drug-resistant phenotype survive, albeit in a quiescent state (Fig. 8.3**a** and Fig. 8.3**d**). For $p = 0.6$, in both the no cost and cost scenario the drug-tolerant phenotype survive in a quiescent state as the *proliferation signal* is sufficient for the cells to be viable but not to proliferate. In the no cost scenario, the drug-resistant phenotype proliferate and fill the domain (Fig. 8.3**b**). However, when cost is applied, proliferation is slowed, and the drug-resistant phenotype fill less than half of the domain (Fig. 8.3**e**). Applying cost increases the cell cycle length, reducing the growth rate of the drug-resistant phenotype.

When the *proliferation signal* is sufficient to allow both the drug-tolerant phenotype and the drug-resistant phenotype to proliferate ($p = 1$), the cells proliferate at the same rate and meet in the middle in the no cost scenario (Fig. 8.3**c**). While the drug-tolerant phenotype expand faster than the drug-resistant phenotype when there is a cost of resistance and fill over half of the domain (Fig. 8.3**f**).

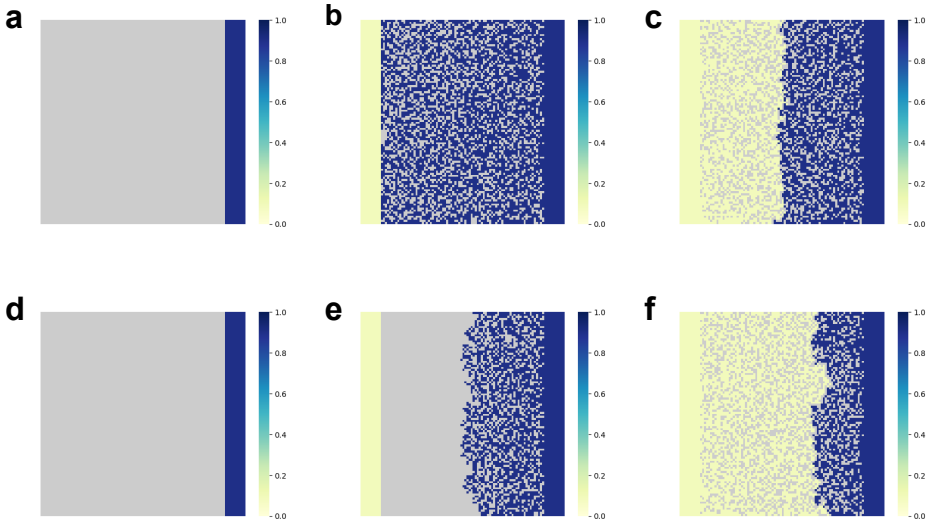

Figure 8.3: Competition between phenotypes in different local conditions. Spatial distribution of six different *in-silico* scratch assays. The cancer cells on the left are the drug-tolerant phenotype (Fig. 8.1**b**) while the cancer cells on the right are the drug-resistant phenotype (Fig. 8.1**c**). We consider the growth rates of the phenotypes where there is no cost of resistance (**a - c**) and where there is a cost (**d - f**). We consider three different levels of *proliferation signal* for the whole domain. **a:** No cost of resistance and $p = 0.05$. **b:** No cost of resistance and $p = 0.6$. **c:** No cost of resistance and $p = 1$. **d:** Cost of resistance and $p = 0.05$. **e:** Cost of resistance and $p = 0.6$. **f:** Cost of resistance and $p = 1$.

With our experiment we demonstrate that with our model that incorporates phenotypic variation of cancer cells we can capture competitive interactions between sensitive and resistant cells. These dynamics are important in adaptive therapies where the aim is to control tumour burden by exploiting the competition between sensitive and resistant populations (Section 2.2.3).

8.5 Continuous treatment

From detection ($t = 0$) the tumour will continue to grow without treatment (Fig. 8.4**a**). On day 9, we observe symmetric diffusion of cancer cells phenotypic variation (Fig. 8.4**b - c**). Cancer cells rapidly invade the homeostatic tissue and by day 75 we observe a shift towards faster proliferating phenotypes and the suppression of drug-resistant phenotype cancer cells (Fig. 8.4**b - c**). In the absence of treatment all cells are non-protected (Fig. 8.4**d**).

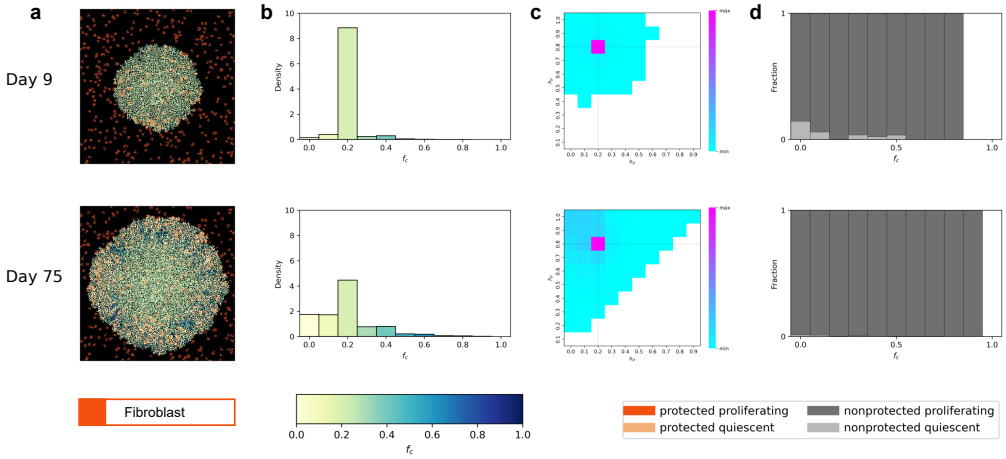

Figure 8.4: The phenotypic landscape for the untreated tumour. For a single simulation we show at day 9 and day 75: **a:** Spatial distribution; **b:** Distribution of cancer cell phenotype; **c:** Cancer cell density on the phenotypic landscape; and **d:** Fraction of cancer cells that are protected and proliferating, protected and quiescent, non-protected and quiescent or non-protected and proliferating by phenotype.

If the tumour is treated continuously with the inhibitor drug, by day 9 we observe the bulk of cancer cells become quiescent as the *proliferation signal* is brought below the proliferative threshold (Fig. 8.5**d**). By day 75 there is a reduction in tumour burden as the bulk of the quiescent cancer cells die (Fig. 8.5**a**) and residual disease forms where cancer cells are protected by the fibroblasts (Fig. 8.5**d**). We observe a shift in phenotypic variation of cancer cells towards lower h_d (drug-tolerant phenotype) as these cells remain viable in lower local *proliferation signal* levels and hence are more able to survive the

effects of the inhibitor drug (Fig. 8.5**c**). By day 185 we observe protected cancer cells proliferating into adjacent protective niches and tumour burden increasing (Fig. 8.5**a**). We see cancer cells with low h_p (drug-resistant phenotype R) emerge and proliferate despite the low local levels of *proliferation signal* (Fig. 8.5**a**). We observe a shift in phenotypic variation of cancer cells towards the drug-resistant phenotype (Fig. 8.5**b - c**) a cancer cell phenotype that can proliferate while non-protected (Fig. 8.5**d**). The resulting tissue is composed of two patterns of residual disease. Pockets of surviving, protected cancer cells of drug-tolerant phenotype located adjacent to fibroblasts, and larger clusters of non-protected cancer cells with drug-resistant phenotype that emerge from protective niches (Fig. 8.5**a**). Expansion of protected cancer cells and their phenotypic variation result in the tumour continuing to grow, although on a much longer timescale than that of the untreated tumour (Fig. 8.6**b**).

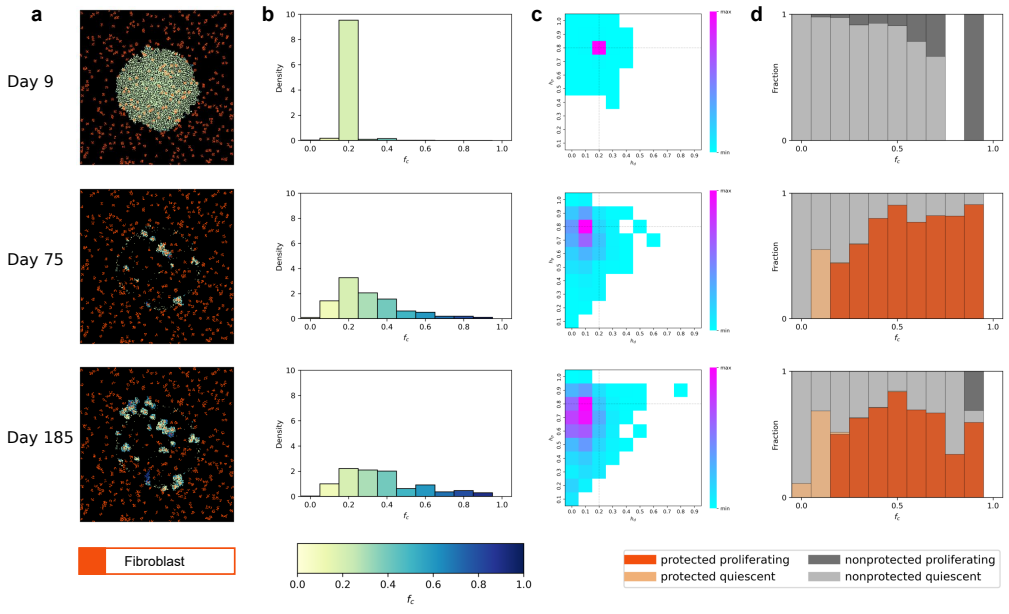

Figure 8.5: The phenotypic landscape for the continuously treated tumour. For a single simulation we show at day 9, day 75 and day 185: **a:** Spatial distribution; **b:** Distribution of cancer cell phenotype; **c:** Cancer cell density on the phenotypic landscape; and **d:** Fraction of cancer cells that are protected and proliferating, protected and quiescent, non-protected and quiescent or non-protected and proliferating by phenotype.

8.6 Intermittent treatment scheduling

In Section 6.2 we investigated using intermittent treatment schedules to exploit the transient and reversible nature of therapy triggered stromal activation for a homogeneous population of cancer cells using the stroma-activation dependent model. Similarly, we investigated introducing intermittent scheduling with the stroma-proximity dependent model, also with a homogeneous population of cancer cells (Section 7.2). In both models, by introducing breaks in treatment delivery, tumour burden could be modulated with similar patterns of residual disease. Our analysis indicates the emergence of residual disease depends on the diffusion dynamics of the molecularly targeted drug, determined by both the vessel density and treatment scheduling. In both models the treatment schedule of $\tau_T = 50$ days and $\tau_H = 20$ days produced the best trade-off between minimising relative tumour burden and limiting cumulative treatment days. We are interested in how intermittent treatment scheduling reshapes phenotypic variation.

We compare the outcomes of multiple replicates of different intermittent treatment regimes $\tau_T = \{30, 50, 70\}$ days with $\tau_H = \{10, 20, 30\}$ days over 500 days of therapy with phenotypic variation incorporated into the stroma-proximity dependent model. Again, we consider the tumour burden and the cumulative days of drug delivery, relative to the continuous treatment case (Fig. 8.6**a**). All intermittent treatment regimes result in a higher average tumour burden compared to continuous treatment. For $\tau_H > 10$ days we observe a breakdown of the non-linear correspondence between τ_T and relative tumour burden identified in the other models (Fig. 6.2**a** and Fig. 7.2**a**).

With a short holiday period ($\tau_H = 10$ days) there is no regrowth during the pause in treatment in the first two treatment cycles (Fig. 8.6**b**). In later treatment cycles we observe some growth during the treatment holiday periods when there is a shift in the phenotypic variation of the cancer cells that now allows for some proliferation (Fig. 8.6**b**). Without regrowth during the first few treatment holiday periods, as τ_T increases the relative tumour burden displays a decrease for $\tau_T < 50$ days and an increase for $\tau_T > 50$ days, which could be indicative of

a turning point similar to the previous results (Fig. 6.2**a** and Fig. 7.2**a**).

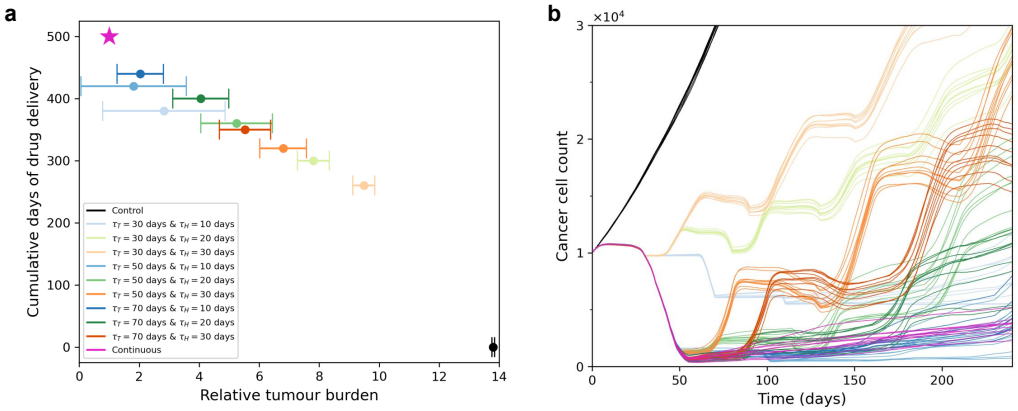

Figure 8.6: Intermittent treatment regime analysis with the cancer cell phenotypic variation included. a: Cumulative days of drug delivery (measured as the sum of drug delivery days over 500 days of therapy) against relative tumour burden (measured as the sum of total cancer cell count over the $t \in [0, 500]$ day window normalised to the continuous treatment case) for $\tau_T = \{30, 50, 70\}$ days for $\tau_H = \{10, 20, 30\}$ days and for no treatment. Results show the average of ten simulations of each schedule and includes 95% confidence intervals. The pink star indicates measures for continuous treatment. **b:** Tumour burden for $t \in [0, 240]$ days under no treatment, continuous treatment, and nine intermittent treatment schedules ($\tau_T = \{30, 50, 70\}$ days and $\tau_H = \{10, 20, 30\}$ days). Individual realisations are shown, with ten stochastic simulations conducted for both untreated and treated conditions. See Appendix E for animations of the spatial distribution, cancer cell phenotypic distribution, breakdown of cancer cell population by protection and proliferation status and the cancer cell phenotypic landscape for the tumour and the cancer cells that die for no treatment, the considered intermittent treatment regimes and continuous treatment.

Longer breaks in treatment ($\tau_H = \{20, 30\}$ days) allows for cancer cells to resume proliferation during the treatment holiday period. This period of proliferation increases the potential of phenotypic variation. With increased phenotypic variation within the cancer cell population there is a greater chance of a drug-resistant phenotype to emerge. Once treatment is resumed, this phenotype can continue to proliferate, without protection from fibroblasts, reducing the rate of cancer death during the treatment delivery period. Overtime the drug-resistant phenotype can become dominant and results in

treatment failure whereby the tumour continues to grow despite the effects of the drug (Fig. 8.6**b**). The resulting residual disease is comprised of regions of cancer cells with drug-tolerant phenotype located in regions of high vessel density (compare with Fig. 6.9) surrounded by a mass of cancer cells with drug-resistant phenotype (Fig. 8.7**a** day 240).

In order to carry out meaningful comparisons with the stroma-proximity dependent model we choose to focus on the intermittent treatment regime $\tau_T = 50$ days and $\tau_H = 20$ days. During the first drug delivery period there is a wave of bulk death and by day 49 we observe some cancer cells surviving by becoming protected by fibroblasts (Fig. 8.7**a**). The bulk of the protected cancer cells is able to proliferate (Fig. 8.7**d**). At this point there is not a significant shift in the phenotype of the cancer cells (Fig. 8.7**b - c**). There are some cancer cells that survive due to the local drug concentration not building up sufficiently during the first treatment period, these cells die in the next drug delivery period (Fig. 8.7**a** day 185).

Following the first drug delivery period, when the bulk death of cancer occurs and a small number of cancer cells survive, protected cancer cells become non-protected during the treatment holiday period. In following drug delivery periods, given the small clusters of residual disease and the timescale that the stromal protection operates on, a smaller fraction of cancer cells become protected (Fig. 8.7**d** day 185). The cancer cells that survive have shifted in the phenotypic landscape to a phenotype that is more resistant to the effects of the drug (Fig. 8.7**b - c** day 185). When the cancer cells return to a proliferative state during the drug holiday period, we see an expansion of cancer cells with drug-resistant phenotype and over successive cycles of treatment we see that by day 240, rebounding disease comprised of mostly these drug-resistant phenotype cancer cells (Fig. 8.7**a - c**). These are cancer cells that can proliferate without stromal protection (Fig. 8.7**d**).

We find the cancer cell population shifts to a drug-resistant phenotype during intermittent treatment. These results depend on our choice of parameters; further investigation of the parameter space may reveal combinations that

produce different outcomes. For example, if the timescale of stromal protection is fast enough to save cancer cells sooner in the drug delivery period it could shift the balance towards the drug-tolerant phenotype cancer cells and outcomes more comparable to the continuous treatment scenario.

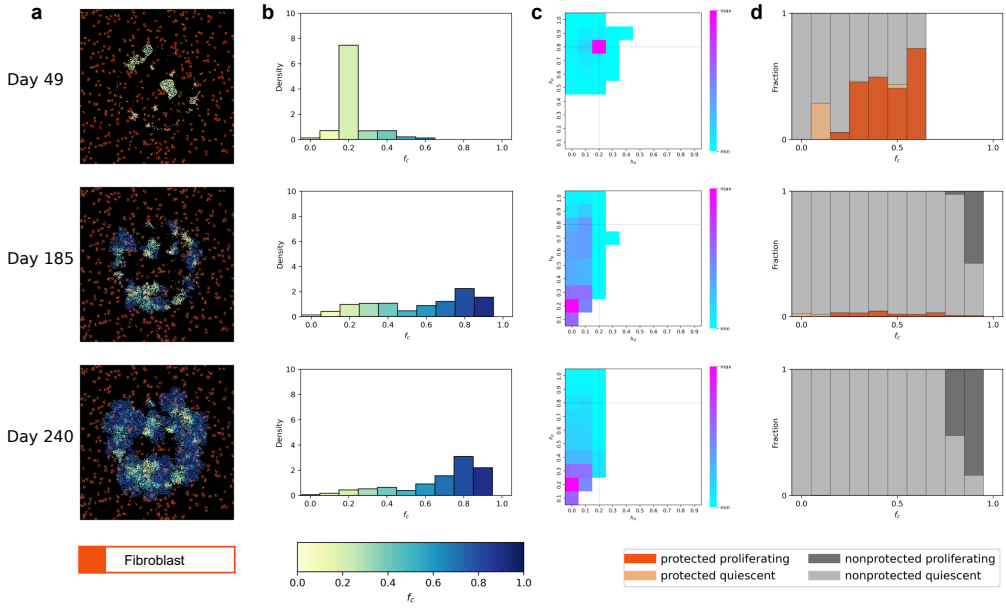

Figure 8.7: The phenotypic landscape for the tumour treated with intermittent treatment regime $\tau_T = 50$ days and $\tau_H = 20$ days. For a single simulation we show at day 49, day 185 and day 240: **a:** Spatial distribution; **b:** Distribution of cancer cell phenotype; **c:** Cancer cell density on the phenotypic landscape; and **d:** Fraction of cancer cells that are protected and proliferating, protected and quiescent, non-protected and quiescent or non-protected and proliferating by phenotype.

8.7 Drug diffusion dynamics can influence intratumoural competition

The underlying theory of the evolution-based treatment strategies is to exploit the competitive advantage drug sensitive cells have over drug resistant cells in a drug free environment [79, 81, 259]. However, with intermittent treatment regimes we observe the expansion of resistant cancer cell populations. With complex interactions operating at different spatial and temporal scales we attempt

to explain the role that the TME plays in phenotypic variation of cancer cells. We propose that drug diffusion dynamics is crucial in shaping the phenotypic variation of residual disease. To test this hypothesis, we remove the drug diffusion dynamics component of our model and instead impose $d(\mathbf{x}, t) = 1$ for all $\mathbf{x} \in \Omega$ during the drug delivery period and $d(\mathbf{x}, t) = 0$ for all $\mathbf{x} \in \Omega$ during the pause in treatment. Using these abrupt drug dynamics reduces the timescale at which cancer cells respond to treatment, hence bringing into focus the effect that changing environmental conditions have on the phenotypic landscape.

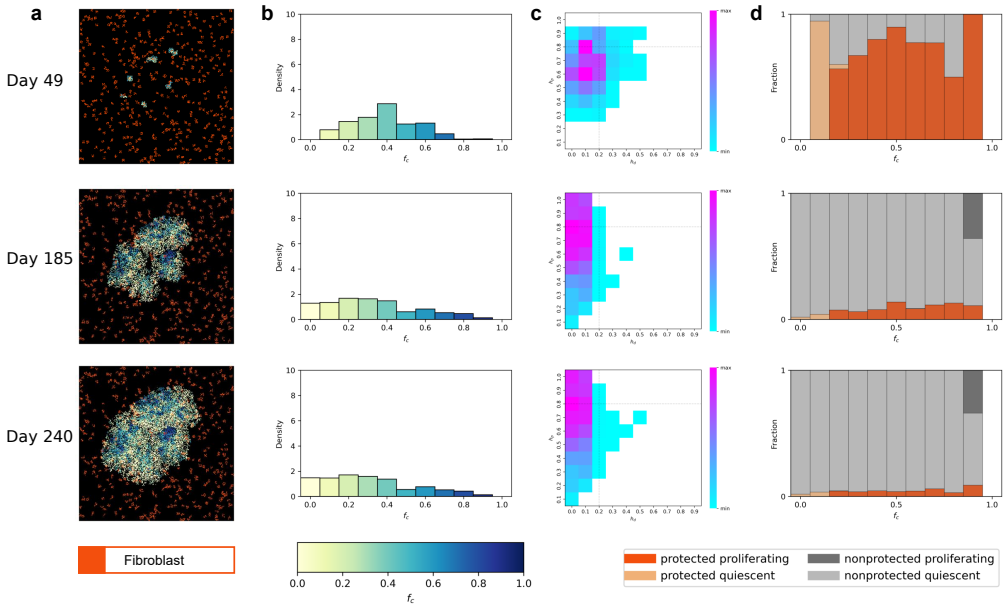

Figure 8.8: The phenotypic landscape for the tumour treated with intermittent treatment regime $\tau_T = 50$ days and $\tau_H = 20$ days with abrupt drug dynamics. For a single simulation we show at day 49, day 185 and day 240: **a:** Spatial distribution; **b:** Distribution of cancer cell phenotype; **c:** Cancer cell density on the phenotypic landscape; and **d:** Fraction of cancer cells that are protected and proliferating, protected and quiescent, non-protected and quiescent or non-protected and proliferating by phenotype.

Without the drug diffusion dynamics, the vasculature structure does not play a part in the emergence of residual disease. Hence, the locations where cancer cells are protected during the initial drug delivery period do not depend on the vessel density (Fig. 8.8**a** day 49). By day 49 we observe a shift in the phenotypic

variation of the cancer cells towards a drug-tolerant phenotype (Fig. 8.8 **b - c**). More cancer cells survive due to stromal protection than when drug diffusion dynamics are implemented (Fig. 8.8**d**). By day 185 there is more residual disease compared to when drug diffusion dynamics are implemented (Fig. 8.8**a**). When the drug is abruptly removed, surviving cancer cells can return to a proliferative state quicker, resulting in more growth during the drug holiday period. With the faster return to a proliferative state during the drug holiday period, cancer cells with drug-tolerant phenotype can proliferate sooner, outcompeting the cancer cells with a drug-resistant phenotype (Fig. 8.8 **b - c**). The increased growth during the drug delivery window also allows for cancer cells to proliferate into locations where they can be protected by fibroblasts once the drug delivery is started again, resulting in a larger fraction of cancer cells becoming protected (Fig. 8.8**d** day 185 and day 240). Over subsequent drug delivery cycles cancer cells with drug-resistant phenotype are constrained by the faster proliferating cancer cells with drug-tolerant phenotype (Fig. 8.8**b - c** day 240). This results in more residual disease by day 240 compared to when drug diffusion dynamics are included (Fig. 8.8**a**) and considerably greater residual disease than when treatment is administered continuously (Fig. 8.5**a**).

In Figure 8.9 we compare the longitudinal distribution of cancer cells for four cases, the untreated tumour, continuous treatment and two intermittent treatment regimes, the first with the drug diffusing in and out of the domain through the vessel sites and the other with abrupt drug dynamics. For the untreated tumour we show cancer cell distribution by their f_c over the duration of treatment ($t \in [0, 100]$ days). For the treated tumours we show cancer cell distribution by their f_c over the duration of treatment, discarding the initial wave of bulk cancer cell death ($t \in [50, 500]$ days). We also quantify within each phenotype f_c the share of protected or non-protected, and proliferating or quiescent cancer cells over the same time period.

Cancer cells in the untreated tumour are non-protected and proliferating (Fig. 8.9**a**). There is a slight shift to faster proliferating low f_c phenotypes. When treated continuously, most cancer cells have lower f_c (Fig. 8.9**b**). While the bulk of proliferating cancer cells are protected, the only non-protected cells that

proliferate are those with a high f_c (Fig. 8.9**c**). Since most proliferating cancer cells are protected with low f_c they make up the bulk of the tumour mass (Fig. 8.5**a** day 185).

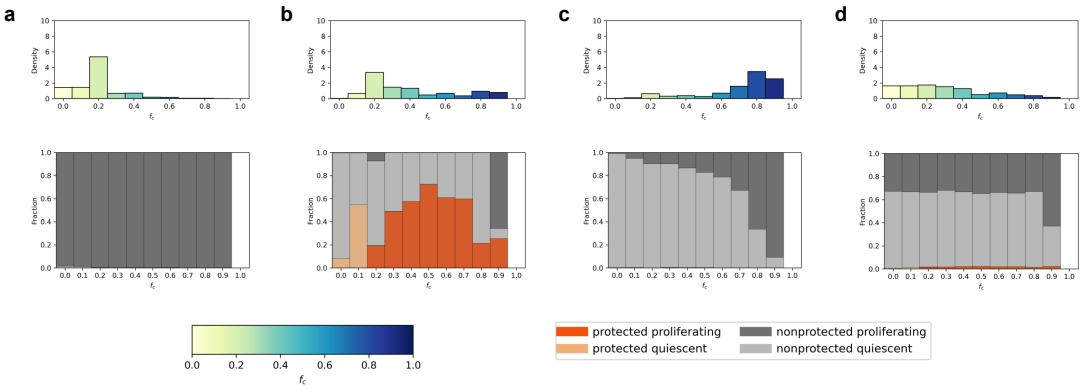

Figure 8.9: Longitudinal distribution of cancer cell phenotype for untreated, continuous and intermittent treatment. We show the longitudinal distribution of cancer cells by phenotype (upper) and share of each phenotype that are protected and proliferating, protected and quiescent, non-protected and quiescent or non-protected and proliferating (lower) over ten simulations for four different treatment cases. **a:** The untreated tumour for $t \in [0, 100]$ days **b:** Continuous treatment for $t \in [50, 500]$ days. **c:** Intermittent treatment regime $\tau_T = 50$ days and $\tau_H = 20$ days for $t \in [50, 500]$ days. **d:** Intermittent treatment regime $\tau_T = 50$ days and $\tau_H = 20$ days with abrupt drug dynamics for $t \in [50, 500]$ days.

When the drug diffuses into and out of the domain through the vessel sites during the intermittent treatment schedule the bulk of surviving cancer cells are those with higher values of f_c and the fraction of protected cancer cells is very low (Fig. 8.9**c**). We observe a larger fraction of cancer cells with high f_c are proliferative while non-protected (drug-resistant phenotype) compared with those with lower values of f_c. Since most proliferating cancer cells are non-protected and drug-resistant phenotype, they make up the bulk of the tumour mass (Fig. 8.7**a** day 240).

With abrupt drug dynamics the timescale of protection during the drug delivery period, and the timescale of recovery to a proliferative state during the drug holiday period operate faster than when the drug diffuses in the domain.

During the intermittent treatment schedule with abrupt drug dynamics the bulk of surviving cancer cells are those with lower f_c and while the fraction of protected cancer cells is also very low, it is higher than when the drug dynamics include diffusion (Fig. 8.9**d**). With more cancer cells with lower f_c that are proliferating while protected during the drug delivery period and returning to a proliferative state quicker in the drug holiday period, they make up the bulk of the tumour mass (Fig. 8.8**a** day 240).

8.8 Discussion

In this chapter, we extended our stroma-proximity dependent model (Chapter 7) to incorporate phenotypic variation of cancer cells. Using this extended model, we captured the phenomenon of sensitive cancer cells outcompeting resistant cancer cells in the untreated tumour. When treatment was applied, our model captured the shift towards drug-tolerant phenotypes, followed by a shift towards drug-resistant phenotypes. We explored the potential of using breaks in treatment to modulate tumour burden. Our results suggested that any benefits of introducing breaks in treatment to exploit the transient and reversible nature of therapy triggered stromal protection are lost when cell-based mechanisms of resistance are present. Although intermittent regimes resulted in higher amounts of residual disease we found that surviving cancer cells phenotypic variation is shaped by the TME.

Our results highlighted the crucial role that drug diffusion dynamics play in the emergence and shape of residual disease. Slower build up of local drug concentrations during the drug delivery period increased the timescale of EMDR and resulted in lower TME-driven cancer survival. Slower dissipation of local drug concentrations during the drug holiday periods increased the timescale of cancer cell recovery, resulting in selection of cancer cells that can proliferate in lower local *proliferation signal* conditions. Eventually, over successive treatment cycles, most cancer cells were drug-resistant. When the local drug dynamics were abrupt, the timescale of EMDR was quicker during the drug delivery period, resulting in more protected cancer cells during

treatment delivery. The timescale of cancer cell recovery was quicker when local drug concentration was abruptly removed during the drug holiday period. Since cancer cells with lower f_c and shorter cell cycles returned to a proliferative state faster, they outcompeted cancer cells with higher f_c and longer cell cycles.

Chapter 9

Conclusion

The aim of this thesis was to investigate interactions between the tumour and the TME that contribute to the emergence of drug resistance while undergoing treatment with a molecularly targeted therapy. While molecularly targeted therapies provide alternative treatment options for cancer patients, with the benefit of lower toxicity than cytotoxic therapies, their success has not been as positive as anticipated due to residual disease and the emergence of resistance. The development of resistance to molecularly targeted therapies is multifactorial, driven by not only the evolution of cell-based mechanisms but also by environmental mechanisms. The dual nature of the relationship between the tumour and the TME includes both competition for space (cancer - stroma) and unidirectional cooperation through cues essential for survival (cancer - reactive stroma). We initially focussed on the interactions between the tumour and the TME that drive the emergence of residual disease from the start of treatment, known as EMDR. We then incorporated cell-based mechanisms of resistance and investigated the complex dynamics that emerge. Mechanisms that drive the onset of resistance to molecularly targeted therapies operate across different temporal and spatial scales: the timescale of cellular processes, the temporal and spatial scale of drug diffusion, and the spatial scale of short-range cell-to-cell crosstalk and interactions. We used a multiscale modelling technique to capture and analyse how all these scales come together.

In Chapter 2 we briefly discussed the development of cancer therapies, focussing on systemic treatments. We highlighted the ambition to develop cancer-specific therapies from the earliest pharmaceutical approaches to contemporary targeted therapies. We discussed molecularly targeted therapies in more detail, explaining how aberrantly activated pathways in cancer, that lead to uncontrolled proliferation and enhanced survival, are targeted with inhibitor drugs. We emphasised that the inevitable emergence of resistance is the main driver of treatment failure across all modes of therapy, then focussed on resistance to molecularly targeted therapies. The role of the TME in the emergence of resistance is discussed in detail (specifically the role CAFs play), providing the necessary biological context that informs our mathematical modelling. We provided an outline of mathematical oncology models in Chapter 3; progressing from simple models of growth, within both deterministic and stochastic modelling frameworks, to advanced modelling frameworks that combine deterministic and stochastic techniques, allowing the complex system of a tumour and its TME to be modelled at multiple scales.

We introduced the first of our multiscale models in Chapter 4, the stroma-activation dependent model. We adopted a hybrid-discrete-continuum model to describe the dynamics of cells acting as individual agents, coupled with the reaction-diffusion dynamics of drug and signalling molecule concentrations. We provided details of the construction of our experimentally calibrated, irregularly vascularised *in-silco* tissue. This tissue, that the tumour grows within and interacts with, was crucial to our investigation of EMDR. Within this tissue we grew a tumour that we used as the initial condition for our *in-silico* experimentation. Our model was rigorously calibrated and validated against *in-vitro* and *in-vivo* experimental data in Chapter 5. We used Approximate Bayesian Computation to calibrate cancer cell growth parameters with drug-naive mouse xenograft model data and cancer cell death parameters to drug treated mouse xenograft model data for a NSCLC cell line. We used data upon cessation of treatment for the same treated mouse xenograft models, to validate our calibrated model.

In Chapter 6 we showed that our calibrated stroma-activation dependent model

captures the dynamics of EMDR, including the initial response to treatment followed by the resurgence of disease. This resistance is in part driven by paracrine signalling from proximal stroma activated by the tumour in response to drug treatment. We investigated intermittent treatment schedules with the aim of exploiting EMDR reversibility to modulate tumour burden. When the treatment was withdrawn the stromal response reversed, and in the absence of the inhibitor drug the tumour resumed growth from the few remaining cells in the survival niches. When treatment recommenced, there was a diminished response, indicating resistance mechanisms were at play. Our *in-silico* results showed that removal of paracrine signalling from the activated stroma during the holiday period can be used to modulate tumour growth. However, the long-term benefits of the introduction of drug holidays was only appreciated over an intermittent treatment schedule composed of several treatment cycles since factors that contributed the formation of residual disease (cancer cell proliferation and stroma activation/deactivation) are governed by the gradual dynamics of diffusible signalling molecules, and drug delivery and clearance. As a test-case for our investigation of the spatial attributes of emergent niches of residual disease we used an intermittent drug delivery regime that maintained tumour burden in the long-term. We showed how heterogeneity of local tissue conditions drives different responses to treatment and shape residual disease. We characterised the niches where cancer cells survive the course of intermittent treatment with targeted therapies using our extensive investigation of longitudinal occupancy and neighbourhood distribution, as well as vessel density analysis.

We observed poor treatment outcomes in both regions of low vessel density and regions of high vessel density, indicating a non-linear relationship between vessel density and treatment outcome. The nature of the resistance and the pattern of residual disease differed between these regions, both of which can occur in a heterogeneous TME. With low vessel density, resistance was attributed to poor perfusion of the drug, while resistance in regions with high vessel density was attributed to high stroma activation (EMDR). Within our *in-silico* tissue, with its irregular, experimentally calibrated, vessel distribution, we identified three

distinct niches. In persistence niches, where drug perfusion was insufficient to cause bulk death due to low vessel density, we characterised residual disease as clusters of dormant cancer cells that rely only on autocrine signalling for survival. In survival niches, where vessel density is higher, the drug diffused and built up sufficiently to kill cancer cells quickly. However, this quick exposure to high drug concentrations triggers signalling from cancer cells experiencing stress to cue rescue from the stroma on a timescale that resulted in the formation of residual disease. This residual disease is characterised by active stroma infiltration, and reliance on paracrine signalling for survival. Finally, we observed eradication niches characterised by intermediate vessel density. In these regions, the timescale of drug diffusion being smaller than that of stroma activation resulted in a complete eradication of cancer.

Recent experimental studies indicate that during targeted therapy, all stroma is implicated in protection of cancer cells, regardless of activation processes. In light of this information we refined our model and presented a modified variant of the stroma-activated dependent model, the stroma-proximity dependent model in Chapter 7. In the stroma-proximity dependent model, cancer cells were protected by their proximity to fibroblasts (CAFs). We investigated the emergence of resistance and formation of residual disease using the stroma-proximity dependent model and we found that some intermittent treatment schedules modulated tumour burden. The resulting residual disease was located in both persistence and survival niches, indicating that, for the stroma-proximity dependent model, the dynamics of diffusible signalling molecules and drug delivery and clearance were also crucial to their formation. Additionally, we investigated the association between stroma dispersal and response to treatment. We found, in agreement with similar studies, an inverse relationship between stromal dispersion and time to disease resurgence, whereby tissue with a highly dispersed stroma results in higher levels of residual disease, reducing the time to disease progression. Conversely, sparsely dispersed stroma limits the locations that cancer cells can become protected, resulting in lower amounts of residual disease, prolonging the time to disease progression.

Our findings in Chapters 6 and 7 showed that knowledge of TME architecture

in terms of both the vascular and stromal structure is central to our ability to modulate EMDR. EMDR is only one component of the emergence of resistance to targeted therapies. While the residual disease in persistent niches was maintained in a quiescent state, survival niches provided safe havens for proliferating cancer cells while undergoing treatment. The survival of these cells, despite hostile conditions, provides opportunities for permanent acquired resistance to develop. In Chapter 8 we allowed phenotypic variation in cancer cells' response to environmental cues. With our phenotypic landscape incorporated into the stroma-proximity dependent model (presented in Chapter 7) we captured the formation of residual disease driven by EMDR followed by a shift in the phenotypic variation of cancer cells towards a drug-tolerant phenotype and eventually to a drug-resistant phenotype when treatment is administered continuously. Our investigation of intermittent treatment schedules in Chapters 6 and 7 that only included EMDR drivers of resistance, resulted in some regimes being successful at modulating tumour burden. However, when cell-based mechanisms were also considered, intermittent treatment schedules offered no benefit over continuous treatment. With our chosen parameters, intermittent treatment schedules resulted in treatment failure on a quicker timescale than continuous treatment and residual disease was largely comprised of drug-resistant cancer cells. While our investigation of the parameter space is incomplete, we do demonstrate that the model predicts different outcomes when drug concentration dynamics operate on a much quicker timescale. In this case the intermittent treatment schedule failed on a quicker timescale than gradual molecular diffusion dynamics and the resulting residual disease was comprised mostly of drug-tolerant cancer cells. Our results suggest that the timescales of the diffusible molecules can affect cancer cell phenotypic variation.

While the mechanisms that drive resistance to molecularly targeted therapies are not fully understood, they are known to be complex and multifactorial. In this thesis we attempt to unpick these mechanisms. First, we focussed on initial drivers of resistance mediated by the TME by considering two alternative hypotheses for stroma driven resistance motivated by independent experimental

studies. Regions of residual disease were consistent across models, indicating that TME architecture is crucial to the formation of residual disease irrespective of the specific mechanism for stroma-driven resistance. In light of these results, we then extended our modelling framework by incorporating cell-based mechanisms of resistance and investigated the patterns of residual disease that resulted when both environmentally-mediated and cell-based mechanisms of resistance are at play.

In summary our study was primarily concerned with the spatial attributes that promote the emergence of survival niches when undergoing intermittent treatment with molecularly targeted therapies. We established that the creation of survival niches depends on the interplay of local drug concentration and cell-to-cell crosstalk. Local drug concentration depends on both the drug supply (duration of administration) and the physical configuration of drug delivery (vessel distribution). In regions that receive high concentrations of the inhibitor drug, the tumour is under a greater degree of stress. This triggers cues for stromal assistance to aid with survival that are not evident in regions where the tumour is experiencing less stress. While we showed that residual disease that emerges via EMDR could be modulated by introducing breaks in treatment, these breaks only allowed for more opportunity for drug-tolerant or drug-resistant phenotypes to evolve when cell-based resistance mechanisms were included. The shift in the phenotypic variation of the cancer cell population also depended on the timescale of drug diffusion dynamics. With slower timescales drug-resistant cells outcompeted drug-tolerant cells while quicker timescales enabled drug-tolerant cancer cells to outcompete drug-resistant cells. Our analysis highlights the importance of considering how the spatial features of tumours and their immediate microenvironment can synergise to drive drug resistance.

9.1 Future directions

Mathematical models are ubiquitous in cancer research. They allow for inexpensive, quick and easily modifiable *in-silico* hypothesis testing and

experimentation. Technological advances are allowing the development of sophisticated patient-specific calibrated mathematical models to become a reality. While our model is parsimonious in nature, it is rigorously calibrated with *in-vitro* and *in-vivo* experimental data and lends itself to *in-silico* hypothesis testing and experimentation on resistance mechanisms in solid metastatic tumours. The predictive capability of our model can be improved further by further collaboration between clinicians, experimental biologists, and mathematicians. With an interdisciplinary approach, greater insight can be gained into up-to-date treatment protocols, the feasibility of proposed treatment regimes in the clinic, and the underlying biology of cancer and its response to treatment in the laboratory. These insights can better inform the inputs, assumptions and validation of the mathematical models.

Often treatment plans include multiple modes of treatment with carefully calibrated schedules. Our model could be extended to include more than one mode of therapy or therapeutic drug, including surgery, radiotherapy, cytotoxic agents, immunotherapy drugs, and multiple molecularly targeted therapies that target both cancer and stroma. Instead of intermittent treatment schedules we could consider adaptive therapy scheduling, where real-time patient response can inform drug administration protocols.

While we introduced phenotypic variation in the cancer cell population, we only considered a particular phenotype of CAF. Our models can be generalised or extended to investigate interactions between the tumour and other CAF phenotypes and/or cell types in the TME. The passive/inactivated stroma compartment consists of all cells in the microenvironment, some of which can engage in crosstalk with cancer cells. For example, we could include CAF phenotypes that occupy distinct locations in relation to the tumour and vary in function to the CAFs we considered. Additionally, we could include immune cells that can exhibit the same dual role of promoting cancer survival while also competing for space and resources.

Our choice of a static vasculature is based on the assumption that early-stage growth of a metastatic tumour is avascular. Although our initial tumour size is

within reported bounds for avascular tumours, it does exceed the minimum size of tumours that have undergone angiogenesis [260, 261]. Given the mathematical tractability of our models is significantly simplified with static vasculature, we argue our assumption is a reasonable compromise while acknowledging that a dynamic vasculature, whereby vessels appear and disappear through compression and angiogenesis processes, could affect model outcomes. Compression of blood vessels in survival niches could reduce local drug concentrations sufficiently to slow the timescale of stromal activation/protection resulting in lower levels of residual disease. Conversely, the creation of blood vessels in eradication niche could increase local drug concentration sufficiently to allow for stromal activation/protection to rescue cancer cells within a timescale that allows for residual disease to form.

We have assumed a simplified TME, with a 2D representation of vasculature running perpendicular to the tissue, and neglected both angiogenesis and ECM remodelling, all of which affect drug diffusion dynamics. Our model can potentially be extended to incorporate more complex vasculature (non-perpendicular, dynamic or 3D) or ECM-driven drug protection mechanisms (non-homogeneous spatial diffusion). Similarly, we could extend the models to include angiogenesis, allowing for the investigation of the complex dynamics in tumours characterised by a dynamic vasculature, and potential inclusion of vascular treatments, such as therapies that target angiogenesis. Finally, we ignore the extensive cancer cell turnover that occurs in tumours. Crucially, this turnover can affect the competition between cancer cell phenotypes in both drug-naive and treated tumours. Extending our models to include cancer cell birth-death processes could improve the accuracy of our predictions when we consider the emergence of resistance to molecularly targeted therapies within an evolutionary context.

In this thesis we found that structural features of the TME were crucial in the formation and shape of emergent residual disease. Our work highlights the importance of including spatial features when modelling a tumours response to therapy, contributing to the ever-expanding arsenal of modelling-based investigations of drug resistance in cancer.

Bibliography

[1] Milne, A., Marusyk, A., Maini, P.K., Anderson, A.R.A. & Picco, N. The role of environmentally mediated drug resistance in facilitating the spatial distribution of residual disease. *Commun Biol* **8(1)**, 1189 (2025).

[2] Brown, J.S., Amend, S.R., Austin, R.H., Gatenby, R.A., Hammarlund, E.U. & Pienta K.J. Updating the Definition of Cancer. *Mol Cancer Res* **21(11)**, 1142-1147 (2023).

[3] Zhong, L. et al. Small molecules in targeted cancer therapy: advances, challenges, and future perspectives. *Sig Transduct Target Ther* **6(1)**, 201 (2021).

[4] Bedard, P.L., Hyman, D.M., Davids, M.S. & Siu, L.L. Small molecules, big impact: 20 years of targeted therapy in oncology. *Lancet* **395(10229)**, 1078-1088 (2020).

[5] Min, H.-Y. & Lee, H.-Y. Molecular targeted therapy for anticancer treatment. *Exp Mol Med* **54(10)**, 1670-1694 (2022).

[6] Rizzolio, S., Giordano, S., & Corso, S. The importance of being CAFs (in cancer resistance to targeted therapies). *J Exp Clin Cancer Res* **41(1)**, 319 (2022).

[7] Desai, B. et al. Multifactorial stroma-mediated resistance is a major contributor to residual disease under targeted therapies in lung cancers. Preprint at https://www.researchsquare.com/article/rs-6264377 (2025).

[8] Meads, M.B., Gatenby, R.A. & Dalton, W.S. Environment-mediated drug resistance: a major contributor to minimal residual disease. *Nat Rev Cancer* **9(9)**, 665-674 (2009).

[9] Liang, X. et al. Characteristics and molecular mechanism of drug-tolerant cells in cancer: a review. *Front Oncol* **13**, 1177466 (2023).

[10] Hirata, E. et al. Intravital imaging reveals how BRAF inhibition generates drug-tolerant microenvironments with high integrin β1/FAK signaling. *Cancer Cell* **27(4)**, 574-588 (2015).

[11] Klemm, F. & Joyce, J.A. Microenvironmental regulation of therapeutic response in cancer. *Trends Cell Biol* **25(4)**, 198-213 (2015).

[12] Aktipis, C.A. et al. Cancer across the tree of life: cooperation and cheating in multicellularity. *Philos Trans R Soc Lond B Biol Sci* **370(1673)**, 20140219 (2015).

[13] Trigos, A.S., Pearson, R.B., Papenfuss, A.T. & Goode, D.L. How the evolution of multicellularity set the stage for cancer. *Br J Cancer* **118(2)**, 145-152 (2018).

[14] Doonan, J.H. & Sablowski, R. Walls around tumours - why plants do not develop cancer. *Nat Rev Cancer* **10(11)**, 794-802 (2010).

[15] Ujvari, B., Gatenby, R.A. & Thomas, F. The evolutionary ecology of transmissible cancers. *Infect Genet Evol* **39**, 293-303 (2016).

[16] Odes, E.J. et al. Earliest hominin cancer: 1.7-million-year-old osteosarcoma from Swartkrans Cave, South Africa. *South African Journal of Science* **112(7-8)**, 1-5 (2016).

[17] Aufderheide, A.C., Rodriguez-Martin, C. & Langsjoen, O. *The Cambridge Encyclopedia of Human Paleopathology* (Cambridge University Press, Cambridge, 1998).

[18] Hajdu, S.I. A note from history: landmarks in history of cancer, part 1. *Cancer* **117(5)**, 1097-1102 (2011).

[19] Mukherjee, S. *The Emperor of All Maladies: A Biography of Cancer* (Scribner, New York, 2010).

[20] Wyld, L., Audisio, R.A. & Poston, G.J. The evolution of cancer surgery and future perspectives. *Nat Rev Clin Oncol* **12(2)**, 115-124 (2015).

[21] Oelschlaeger, T.A. Bacteria as tumor therapeutics? *Bioeng Bugs* **1(2)**, 146-147 (2010).

[22] Dobosz, P. & Dzieciątkowski, T. The intriguing history of cancer immunotherapy. *Front Immunol* **10**, 2965 (2019).

[23] Despeignes, V. Observation concernant un cas de cancer de l'estomac traitè par les rayons Röntgen. *Lyon Med J* **82**, 428-430 (1896).

[24] Leszczynski, K. & Boyko, S. On the controversies surrounding the origins of radiation therapy. *Radiother Oncol* **42(3)**, 213-217 (1997).

[25] Thariat, J., Hannoun-levi, J., Sun Myint, A., Vuong, T. & Gérard, J. Past, present, and future of radiotherapy for the benefit of patients. *Nat Rev Clin Oncol* **10(1)**, 52-60 (2013).

[26] Bernier, J., Hall, E.J. & Giaccia, A. Radiation oncology: a century of achievements. *Nat Rev Cancer* **4(9)**, 737-747 (2004).

[27] DeVita, V.T. & Chu, E. A History of Cancer Chemotherapy. *Cancer Res* **68(21)**, 8643-8653 (2008).

[28] Krumbhaar, E.B. & Krumbhaar, H.D. The blood and bone marrow in yellow gas (mustard gas) poisoning. Changes produced in bone marrow in fatal cases. *J Med Res* **40**, 497-507 (1919).

[29] Goodman, L.S., Wintrobe, M.M., Dameshek, W., Goodman, M.J., Gilman, A. & McLennan, M.T. Use of methyl-bis(beta-chloroethyl)amine hydrochloride and tris(beta-chloroethyl)amine hydrochloride for Hodgkin's disease, lymphosarcoma, leukemia and certain allied and miscellaneous disorders. *JAMA* **132(2)**, 126-132 (1946).

[30] Farber, S., Diamond, L.K., Mercer, R.D., Sylvester, R.F. & Wolff, J.A. Temporary remissions in acute leukemia in children produced by folic acid antagonist, 4-aminopteroyl-glutamic acid (aminopterin). *N Engl J Med* **238(23)**, 787-793 (1948).

[31] Miller, D.R. A tribute to Sidney Farber - the father of modern chemotherapy. *Br J Haematol* **134(1)**, 20-26 (2006).

[32] Wright, J.C., Prigot, A., Wright, B.P., Weintraub, S. & Wright, L.T. An evaluation of folic acid antagonists in adults with neoplastic diseases: a study of 93 patients with incurable neoplasms. *J Natl Med Assoc* **43(4)**, 211-240 (1951).

[33] Sonkin, D., Thomas, A. & Teicher, B.A. Cancer treatments: past, present, and future. *Cancer Genet* **286**, 18-24 (2024).

[34] Singh, R.K., Kumar, S., Prasad, D.N. & Bhardwaj, T.R. Therapeutic journey of nitrogen mustard as alkylating anticancer agents: Historic to future perspectives. *Eur J Med Chem* **151**, 401-433 (2018).

[35] Gonen, N. & Assaraf, Y.G. Antifolates in cancer therapy: structure, activity and mechanisms of drug resistance. *Drug Resist Updat* **15(4)**, 183-210 (2012).

[36] Dasari, S. & Tchounwou, P.B. Cisplatin in cancer therapy: molecular mechanisms of action. *Eur J Pharmacol* **740**, 364-378 (2014).

[37] Hanahan, D. & Weinberg, R.A. Hallmarks of cancer: the next generation. *Cell* **144(5)**, 646-674 (2011).

[38] Hardin, J. & Bertoni, G. *Becker's world of the cell.* Ninth edition (Pearson Education, global edition, 2018).

[39] Glaviano, A. et al. PI3K/Akt/mTOR signalling transduction pathway and targeted therapies in cancer. *Mol Cancer* **22(1)**, 138 (2023).

[40] Vara, J.A.F., Casado, E., de Castro, J., Cejas, P., Belda-Iniesta, C. & González-Barón, M. PI3K/Akt signalling pathway and cancer. *Cancer Treat Rev* **30(2)**, 193-204 (2004).

[41] Yuryev, A & Wennogle, L.P. The RAF family: an expanding network of post-translational controls and protein-protein interactions. *Cell Res* **8(2)**, 81-98 (1998).

[42] Matallanas, D. et al. Raf family kinases: old dogs have learned new tricks. *Genes Cancer* **2(3)**, 232-260 (2011).

[43] Zhang, W. & Liu, H. MAPK signal pathways in the regulation of cell proliferation in mammalian cells. *Cell Res* **12(1)**, 9-18 (2002).

[44] Molina, J.R. & Adjei, A.A. The Ras/Raf/MAPK pathway. *J Thorac Oncol* **1(1)**, 7-9 (2006).

[45] Lavoie, H., Gagnon, J. & Terrien, M. ERK signalling: a master regulator of cell behaviour, life and fate. *Nat Rev Mol Cell Biol* **21(10)**, 607-632 (2020).

[46] Weinberg, R.A. *The biology of cancer* Second edition (Garland Science, New York, 2014).

[47] Padhy, L.C., Shih, C., Cowing, D., Finkelstein, R. & Weinberg, R.A. Identification of a phosphoprotein specifically induced by the transforming DNA of rat neuroblastomas. *Cell* **28(4)**, 865-871 (1982).

[48] Schechter, A.L. et al. The *neu* oncogene: an *erb*-B-related gene encoding a $185,000 - M_r$ tumour antigen. *Nature* **312(5994)**, 513-516 (1984).

[49] Gajria, D. & Chandarlapaty, S. HER2-amplified breast cancer: mechanisms of trastuzumab resistance and novel targeted therapies. *Expert Rev Anticancer Ther* **11(2)**, 263-275 (2011).

[50] Kirouac, D.C., et al. HER2+ cancer cell dependence on PI3K vs. MAPK signaling axes is determined by expression of EGFR, ERBB3 and CDKN1B. *PL0S Comput Biol* **12(4)**, e1004827 (2016).

[51] Maadi, H., Soheilifar, M.H., Choi, W.-S., Moshtaghian, A. & Wang, Z. Trastuzumab mechanism of action; 20 years of research to unravel a dilema. *Cancers* **13(14)**, 3540 (2021).

[52] Pottier, C. et al. Tyrosine kinase inhibitors in cancer: breakthrough and challenges of targeted therapy. *Cancers* **12(3)**, 731 (2020).

[53] El-Tanani, M. et al. The impact of the BCR-ABL oncogene in the pathology and treatment of chronic myeloid leukemia. *Pathol Res Pract* **254**, 155161 (2024).

[54] Deininger, M., Buchdunger, E. & Druker, B.J. The development of imatinib as a therapeutic agent for chronic myeloid leukemia. *Blood* **105(7)**, 2640-2653 (2005).

[55] Bixby, D. & Talpaz, M. Seeking the causes and solutions to imatinib-resistance in chronic myeloid leukemia. *Leukemia* **25(1)**, 7-22 (2011).

[56] Alves, R. et al. Resistance to Tyrosine Kinase Inhibitors in Chronic Myeloid Leukemia - From Molecular Mechanisms to Clinical Relevance. *Cancers* **13(19)**, 4820 (2021).

[57] Wu, F. et al. Signaling pathways in cancer-associated fibroblasts and targeted therapy for cancer. *Sig Transduct Target Ther* **6(1)**, 218 (2021).

[58] Lee, J.J. et al. Stromal response to hedgehog signaling restrains pancreatic cancer progression. *Proc Natl Acad Sci U S A* **111(30)**, E3091-E3100 (2014).

[59] Rhim, A. et al. Stromal elements act to restrain, rather than support, pancreatic ductal adenocarcinoma. *Cancer Cell* **25(6)**, 735-747 (2014).

[60] Bhome, R. et al. Exosomal microRNAs derived from colorectal cancer-associated fibroblasts: role in driving cancer progression. *Aging (Albany NY)* **9(12)**, 2666 (2017).

[61] Shi, Y. et al. Targeting LIF-mediated paracrine interaction for pancreatic cancer therapy and monitoring. *Nature* **569(7754)**, 131-135 (2019).

[62] Tape, C. et al. Oncogenic KRAS regulates tumor cell signaling via stromal reciprocation. *Cell* **165(4)**, 910-920 (2016).

[63] Cords, L. et al. Cancer-associated fibroblast phenotypes are associated with patient outcome in non-small cell lung cancer. *Cancer Cell* **42(3)**, 396-412 (2024).

[64] Mathieson, L., Koppensteiner, L., Dorward, D.A., O'Connor, R.A. & Akram, A.R. Cancer-associated fibroblasts expressing fibroblast activation protein and podoplanin in non-small cell lung cancer predict poor clinical outcome. *Br J Cancer* **130(11)**, 1758-1769 (2024).

[65] Bartoschek, M. et al. Spatially and functionally distinct subclasses of breast cancer-associated fibroblasts revealed by single cell RNA sequencing. *Nat Commun* **9(1)**, 5150 (2018).

[66] Öhlund, D. et al. Distinct populations of inflammatory fibroblasts and myofibroblasts in pancreatic cancer. *J Exp Med* **214(3)**, 579-596 (2017).

[67] Steele, N. et al. Inhibition of hedgehog signaling alters fibroblast composition in pancreatic cancer. *Clin Cancer Res* **27(7)**, 2023-2037 (2021).

[68] Xia, Z. & De Wever, O. The plasticity of cancer-associated fibroblasts. *Trends Cancer* (2025).

[69] Biffi, G. et al. IL1-induced JAK/STAT signaling is antagonized by TGFβ to shape CAF heterogeneity in pancreatic ductal adenocarcinoma. *Cancer Discov* **9(2)**, 282-301 (2019).

[70] Elyada, E. et al. Cross-species single-cell analysis of pancreatic ductal adenocarcinoma reveals antigen-presenting cancer-associated fibroblasts. *Cancer Discov* **9(8)**, 1102-1123 (2019).

[71] Cabanoz, H.F. & Hata, A.N. Emerging insights into targeted therapy-tolerant persister cells in cancer. *Cancers (Basel)* **13(11)**, 2666 (2021).

[72] Vander Velde, R. et al. Resistance to targeted therapies as a multifactorial, gradual adaptation to inhibitor specific selective pressures. *Nat Commun* **11(1)**, 2393 (2020).

[73] Sharma, S.V. et al. A chromatin-mediated drug-tolerant state in cancer cell populations. *Cell* **141(1)**, 69-80 (2010).

[74] Lee, J.C., Jang, S.H., Lee, K.Y. & Kim, Y.C. Treatment of non-small cell lung carcinoma after failure of epidermal growth factor receptor tyrosine kinase inhibitor. *Cancer Res Treat* **45(2)**, 79-85 (2013).

[75] Soda, M. et al. Identification of the transforming EML4-ALK fusion gene in non-small-cell lung cancer. *Nature* **448(7153)**, 561-566 (2007).

[76] Lei, Y., Lei, Y., Shi, X. & Wang, J. EML4-ALK fusion gene in non-small cell lung cancer. *Oncol lett* **24(2)**, 277 (2022).

[77] Yamada, T. et al. Paracrine receptor activation by microenvironment triggers bypass survival signals and ALK inhibitor resistance in EML4-ALK lung cancer cells. *Clin Cancer Res* **18(13)**, 3592-3602 (2012).

[78] Aktipis, C.A. & Nesse, R.M. Evolutionary foundations for cancer biology. *Evol Appl* **6(1)**, 144-159 (2013).

[79] Gatenby, R.A., Silva, A.S., Gillies, R.J. & Frieden, B.R. Adaptive therapy. *Cancer Res* **69(11)**, 4894-4903 (2009).

[80] Zhang, J., Cunningham, J.J., Brown, J.S. & Gatenby, R.A. Integrating evolutionary dynamics into treatment of metastatic castrate-resistant prostate cancer. *Nat Commun* **8(1)**, 1816 (2017).

[81] Gallaher, J.A., Enriquez-Navas, P.M., Luddy, K.A., Gatenby, R.A. & Anderson, A.R.A. Spatial heterogeneity and evolutionary dynamics modulate time to recurrence in continuous and adaptive cancer therapies. *Cancer Res* **78(8)**, 2127-2139 (2018).

[82] Staňková, K., Brown, J.S., Dalton, W.S. & Gatenby, R.A. Optimizing cancer treatment using game theory: a review. *JAMA Oncol* **5(1)**, 96-103 (2019).

[83] Frei III, E.M.I.L. et al A comparative study of two regimens of combination chemotherapy in acute leukemia. *Blood* **13(12)**, 1126-1148 (1958).

[84] Basin, S.L. The Fibonacci sequence as it appears in nature. *Fibonacci Q* **1(1)**, 53-56 (1963).

[85] Schuster, S., Fichtner, M. & Sasso, S. Use of Fibonacci numbers in lipidomics - Enumerating various classes of fatty acids. *Sci Rep* **7(1)**, 39821 (2017).

[86] Persaud-Sharma, D. & O'Leary, J.P. Fibonacci Series, Golden Proportions, and the Human Biology. *Austin J Surg* **2(5)**, 1066 (2015).

[87] Boman, B.M., Dinh, T.-N., Decker, K., Emerick, B., Raymond, C. & Schleiniger, G. Why do Fibonacci Numbers Appear in Patterns of Growth in Nature? *Fibonacci Q* **55(5)**, 30-41 (2017).

[88] Euler, L. *Introduction to the analysis of the infinite.* (Book 1 translated by Blanton, J.D.) (Springer-Verlag, New York, 1988).

[89] Malthus, T.R. (n.d.). *An Essay on the Principle of Population.* (Retrieved from Project Gutenberg.) (J. Johnson in St Paul's Church-yard, London, 1798).

[90] Verhulst, P.-F. Notice on the law that a population follows in its growth. (Translated by Delphenich, D.H.) *Corr math phys* **10**, 113-121 (1838).

[91] Laird, A.K. Dynamics of tumor growth. *Br J Cancer* **18(3)**, 490-502 (1964).

[92] Wilson, N., Drapaca, C.S., Enderling, H., Caudell, J.J. & Wilkie, K.P. Modelling Radiation Cancer Treatment with a Death-Rate Term in Ordinary and Fractional Differential Equations. *Bull Math Biol* **85(6)**, 47 (2023).

[93] Hamed, S.S., Straubinger, R.M. & Jusko, W.J. Pharmacodynamic modeling of cell cycle and apoptotic effects of gemcitabine on pancreatic adenocarcinoma cells. *Cancer Chemother Pharmacol* **72(3)**, 553-563 (2013).

[94] Bouhaddou, M. et al. Predicting in vivo efficacy from in vitro data: quantitative systems pharmacology modeling for an epigenetic modifier drug in cancer. *Clin Transl Sci*, **13(2)**, 419-429 (2020).

[95] Wanika, L., Evans, N.D., Johnson, M., Tomkinson, H. & Chappell, M. J. In vitro PK/PD modeling of tyrosine kinase inhibitors in non-small cell lung cancer cell lines. *Clin Transl Sci* **17(3)**, e13714 (2024).

[96] Lotka, A.J. Contribution to the theory of periodic reactions. *J Phys Chem* **14(3)**, 271-274 (1910).

[97] Lotka, A.J. *Elements of Physical Biology.* (Williams & Wilkins Company, Baltimore, 1925).

[98] Volterra, V. Variations and Fluctuations of the Number of Individuals in Animal Species living together. *J Conseil* **3(1)**, 3-51 (1928).

[99] Rosenzweig, M.L. & MacArthur, R.H. Graphical representation and stability conditions of predator-prey interactions. *Am Nat* **97(895)**, 209-223 (1963).

[100] Hijar Islas, A.C., Milne, A., Eizaguirre, C. & Huang, W. Parasite-mediated predation determines infection in a complex predator-prey-parasite system. *Proc R Soc B Biol Sci* **291(2021)**, 20232468 (2024).

[101] Freischel, A.R. et al. Frequency-dependent interactions determine outcome of competition between two breast cancer cell lines. *Sci Rep* **11(1)**, 4908 (2021).

[102] Bayer, P., Gatenby, R.A., McDonald, P.H., Duckett, D.R., Staňková, K. & Brown, J.S. Coordination games in cancer. *PLoS ONE* **17(1)**, e0261578 (2022).

[103] Turing, A.M. The chemical basis of morphogenesis. *Philos Trans R Soc Lond B Biol Sci* **237(641)**, 37-72 (1952).

[104] Meinhardt, H. Models of biological pattern formation: common mechanism in plant and animal development. *Int J Dev Biol* **40(1)**, 123-134 (1996).

[105] Kondo, S. & Asai, R. A reaction-diffusion wave on the skin of the marine angelfish *Pomacanthus*. *Nature* **376(6543)**, 765-768 (1995).

[106] Sick, S, Reinker, S., Timmer, J. & Schlake, T. WNT and DKK Determine Hair Follicle Spacing Through a Reaction-Diffusion Mechanism. *Science* **314(5804)**, 1447-1450 (2006).

[107] Maini, P., Woolley, T.E., Baker, R.E., Gaffney, E.A. & Lee, S.S. Turing's model for biological pattern formation and the robustness problem. *Interface Focus* **2(4)**, 487-496 (2012).

[108] Mayneord, W.V. On a Law of Growth of Jensen's Rat Sarcoma. *Am J Cancer* **16(4)**, 841-846 (1932).

[109] Araujo, R.P. & McElwain, D.L.S. A History of the Study of Solid Tumour Growth: The Contribution of Mathematical Modelling. *Bull Math Biol* **66(5)**, 1039-1091 (2004).

[110] Greenspan, H.P. Models for the growth of a solid tumor by diffusion. *Stud Appl Math* **51(4)**, 317-340 (1972).

[111] Tomlin, C.J. & Axelrod, J.D. Biology by numbers: mathematical modelling in developmental biology. *Nat Rev Genet* **8(5)**, 331-340 (2007).

[112] Moreira, J. & Deutsch, A. Cellular automaton models of tumor development: a critical review. *ACS* **5(2-3)**, 247-267 (2002).

[113] Benzekry, S. et al. Classical Mathematical Models for Description and Prediction of Experimental Tumor Growth. *PLoS Comput Biol* **10(8)**, e1003800 (2014).

[114] Colyer, B., Bak, M., Basanta, D. & Noble, R. A seven-step guide to spatial, agent-based modelling of tumour evolution. *Evol Appl* **17(5)**, e13687 (2024).

[115] Anderson, A.R.A., Chaplain, M.A.J. & Rejniak, K.A. *Single-Cell-Based Models in Biology and Medicine.* (Birkh$\acute{}$auser, Basel, 2007).

[116] Altrock, P.M., Liu, L.L. & Michor, F. The mathematics of cancer: integrating quantitative models. *Nat Rev Cancer* **15(12)**, 730-745 (2015).

[117] Basanta, D., Scott, J.G., Fishman, M.N., Ayala, G., Hayward, S.W. & Anderson, A.R.A. Investigating prostate cancer tumour–stroma interactions: clinical and biological insights from an evolutionary game. *Br J Cancer* **106(1)**, 174-181 (2012).

[118] Beerenwinkel, N., Schwarz, R.F., Gerstung, M. & Makowetz, F. Cancer Evolution: Mathematical Models and Computational Inference. *Syst Biol* **64(1)**, e1-e25 (2015).

[119] Chamseddine, I.M. & Rejniak, K.A. Hybrid modeling frameworks of tumor development and treatment. *WIREs Syst Biol Med* **12(1)**, e1461 (2020).

[120] Brady, R. & Enderling, H. Mathematical Models of Cancer: When to Predict Novel Therapies, and When Not to. *Bull Math Biol* **81(10)**, 3722-3731 (2019).

[121] Hamis, S. et al. Spatial cumulant models enable spatially informed treatment strategies and analysis of local interactions in cancer systems. *J Math Biol* **86(5)**, 68 (2023).

[122] Gatenby, R.A. Models of Tumor-Host Interaction as Competing Populations: Implications for Tumor Biology and Treatment. *J Theor Biol* **176(4)**, 447-455 (1995).

[123] Qi, T., Vincent, B.G. & Cao, Y. A multispecies framework for modeling adaptive immunity and immunotherapy in cancer. *PLoS Comput Biol* **19(4)**, e1010976 (2023).

[124] Spencer, S.L., Berryman, M.J., García, J.A., & Abbott, D. An ordinary differential equation model for the multistep transformation to cancer. *J Theoret Biol* **231(4)**, 515-524 (2004).

[125] Ribba, B. et al. A Tumor Growth Inhibition Model for Low-Grade Glioma Treated with Chemotherapy or Radiotherapy. *Clin Cancer Res* **18(18)**, 5071-5080 (2012).

[126] Picco, N., Sahai, E., Maini, P.K. & Anderson, A.R.A. Integrating models to quantify environment-mediated drug resistance. *Cancer Res* **77(19)**, 5409-5418 (2017).

[127] Gerlee, P. The Model Muddle: In Search of Tumor Growth Laws. *Cancer Res* **73(8)**, 2407-2411 (2013).

[128] Norton, L. A Gompertzian model of human breast cancer growth. *Cancer Res* **48(24 Part 1)**, 7067-7071 (1988).

[129] Marušić, M, Bajzar, Ž. & Vuk-Pavlovic, S. Tumor growth *in vivo* and as multicellular spheroids compared by mathematical models. *Bull Math Biol* **56(4)**, 617-631 (1994).

[130] Yin, A., Moes, D.J.A.R., van Hasselt, J.G.C., Swen, J.J. & Guchelaar, H.J. A Review of Mathematical Models for Tumor Dynamics and Treatment Resistance Evolution of Solid Tumors. *CPT Pharmacometrics Syst Pharmacol* **8(10)**, 720-737 (2019).

[131] McDonald, T.O., Cheng, Y.-C., Graser, C., Nicol, P.B., Temko, D. & Michor, F. Computational approaches to modelling and optimizing cancer treatment. *Nat Rev Bioeng* **1(10)**, 695-711 (2023).

[132] Belkhir, S., Thomas, F. & Roche, B. Darwinian Approaches for Cancer Treatment: Benefits of Mathematical Modeling. *Cancers* **13(17)**, 4448 (2021).

[133] Chaplain, M.A.J. Avascular Growth, Angiogenesis and Vascular Growth in Solid Tumours: The Mathematical Modelling of the Stages of Tumour Development. *Math Comput Model* **23(6)**, 47-87 (1996).

[134] Chaplain, M.A.J. & Lolas, G. Mathematical modelling of cancer invasion of tissue: dynamic heterogeneity. *Netw Heterog Media* **1(3)**, 399-439 (2006).

[135] Gatenby, R.A. & Gawlinski, E.T. A Reaction-Diffusion Model of Cancer Invasion. *Cancer Res* **56(24)**, 5745-5753 (1996).

[136] Hormuth II, D.A. et al. A mechanically coupled reaction-diffusion model that incorporates intra-tumoural heterogeneity to predict *in vivo* glioma growth. *J R Soc Interface* **14(128)**, 20161010 (2017).

[137] Shyntar, A., Patel, A., Rhodes, M., Enderling, H. & Hillen, T. The Tumor Invasion Paradox in Cancer Stem Cell-Driven Solid Tumors. *Bull Math Biol* **84(12)**, 139 (2022).

[138] Wang, S.E. et al. A mathematical model quantifies proliferation and motility effects of TGF-β on cancer cells. *Comput Math Methods Med* **10(1)**, 71-83 (2009).

[139] Fisher, R.A. The wave of advance of advantageous genes. *Ann Eugen* **7(4)**, 355-369 (1937).

[140] Sánchez-Garduño, F. & Maini, P.K. Traveling Wave Phenomena in Some Degenerate Reaction-Diffusion Equations. *J Differ Equ* **117(2)**, 281-319 (1995).

[141] Hamel, F. & Nadirashvili, N. Travelling Fronts and Entire Solutions of the Fisher-KPP Equation in $\mathbb{R}^N$. *Arch Rational Mech Anal* **157(2)**, 91–163 (2001).

[142] Perumpanani, A.J., Sherratt, J.A., Norbury, J., & Byrne, H.M. A two parameter family of travelling waves with a singular barrier arising from the modelling of extracellular matrix mediated cellular invasion. *Phys D: Nonlinear Phenom*, **126(3-4)**, 145-159 (1999).

[143] Swanson, K.R., Bridge, C., Murray, J.D. & Alvord, E.C.Jr. Virtual and real brain tumors: using mathematical modeling to quantify glioma growth and invasion. *J Neurol Sci* **216(1)**, 1-10 (2003).

[144] Strobl, M.A.R., Krause, A.L., Damaghi, M., Gillies, R., Anderson, A.R.A. & Maini, P.K. Mix and Match: Phenotypic Coexistence as a Key Facilitator of Cancer Invasion. *Bull Math Biol* **82(1)**, 15 (2020).

[145] Johnston, S.T., Shah, E.T., Chopin, L.K., McElwain, D.L.S. & Simpson, M.J. Estimating cell diffusivity and cell proliferation rate by interpreting IncuCyte ZOOM™assay data using the Fisher-Kolmogorov model. *BMC Syst Biol* **9(1)**, 38 (2015).

[146] Ward, J.P. & King, J.R. Mathematical modelling of avascular-tumour growth. *IMA J Math Appl Med Biol* **14(1)**, 39-69 (1997).

[147] Martin, N.K., Gaffney, E.A., Gatenby, R.A. & Maini, P.K. Tumour-stromal interactions in acid-mediated invasion: A mathematical model. *J Theor Biol* **267(3)**, 461-470 (2010).

[148] Fiandaca, G., Delitala, M. & Lorenzi, T. A Mathematical Study of the Influence of Hypoxia and Acidity on the Evolutionary Dynamics of Cancer. *Bull Math Biol* **83(7)**, 83 (2021).

[149] Gillespie, D.T. Exact stochastic simulation of coupled chemical reactions. *J Phys Chem* **81(25)**, 2340-2361 (1977).

[150] Warne, D.J., Baker, R.E. & Simpson, M.J. Simulation and inference algorithms for stochastic biochemical reaction networks: from basic concepts to state-of-the-art. *J R Soc Interface* **16(151)**, 20180943 (2019).

[151] Simoni, G., Reali, F., Priami, C., & Marchetti, L. Stochastic simulation algorithms for computational systems biology: Exact, approximate, and hybrid methods. *WIREs Syst Biol Med* **11(6)**, e1459 (2019).

[152] Feller, W. Die Grundlagan der Volterraschen Theorie des Kampfes ums Dasein in wahrscheinlichkeitstheoretischer Behandlung. *Acta Biotheor* **5**, 11-40 (1939).

[153] Baake, E. & Wakolbinger, A. Feller's Contributions to Mathematical Biology. in *The Selected Papers of William Feller* (eds. Schilling, R.L., Vondracek, Z. & Woyczynski, W.A.) (Springer-Verlag, Heidelberg, 2015).

[154] Wette, R., Katz, I.N. & Rodin, E.Y. Stochastic Processes for Solid Tumor Kinetics I. Surface-Regulated Growth. *Math Biosci* **19(3-4)**, 231-255 (1974).

[155] Kendall, D.G. Birth-and-death processes, and the theory of carcinogenesis. *Biometrika* **47(1-2)**, 13-21 (1960).

[156] Lakatos, E. et al. Evolutionary dynamics of neoantigens in growing tumors. *Nat Genet* **52(10)**, 1057-1066 (2020).

[157] Shrestha, P. Ghoreyshi, Z.S. & George, J.T. How modulation of the tumor microenvironment drives cancer immune escape dynamics. *Sci Rep* **15(1)**, 7308 (2025).

[158] Gatenbee, C.D. et al. Immunosuppressive niche engineering at the onset of human colorectal cancer. *Nat Commun* **13(1)**, 1798 (2022).

[159] Mumenthaler, S.M. et al. The Impact of Microenvironmental Heterogeneity on the Evolution of Drug Resistance in Cancer Cells. *Cancer Inform* **14(Suppl 4)**, 19-31 (2015).

[160] Kumar, N., Cramer, G.M., Dahaj, S.A.Z., Sundaram, B., Celli, J.P. & Kulkarni, R.V. Stochastic modeling of phenotypic switching and chemoresistance in cancer cell populations. *Sci Rep* **9(1)**, 10845 (2019).

[161] Goldie, J.H. & Coldman, A.J. A mathematical model for relating the drug sensitivity of tumors to their spontaneous mutation rate. *Cancer Treat Rep* **63(11-12)**, 1727-1733 (1979).

[162] Komarova, N. Stochastic modeling of drug resistance in cancer. *J Theor Biol* **239(3)**, 351-366 (2006).

[163] Li, A., Kibby, D. & Foo, J. A comparison of mutation and amplification-driven resistance mechanisms and their impacts on tumor recurrence. *J Math Biol* **87(4)**, 59 (2023).

[164] Qi, A.-S., Zheng, X., Du, C.-Y. & An, B.-S. A cellular automaton model of cancerous growth. *J Theor Biol* **161(1)**, 1-12 (1993).

[165] Basanta, D., Ribba, B., Watkin, E., You, B. & Deutsch, A. Computational analysis of the influence of the microenvironment on carcinogenesis. *Math Biosci* **229(1)**, 22-29 (2011).

[166] MA, M., Kim, J.Y., Pan, C.H. & Kim, E. The impact of the spatial heterogeneity of resistant cells and fibroblasts on treatment response. *PLoS Comp Biol* **18(3)**, e1009919 (2022).

[167] Gerlee, P. & Nelander, S. The Impact of Phenotypic Switching on Glioblastoma Growth and Invasion. *PLoS Comput Biol* **8(6)**, e1002556 (2012).

[168] Tari, H. et al. Quantification of spatial subclonal interactions enhancing the invasive phenotype of pediatric glioma. *Cell Rep* **40(9)**, 111283 (2022).

[169] Fu, X. et al. Spatial patterns of tumour growth impact clonal diversification in a computational model and the TRACERx Renal study. *Nat Ecol Evol* **6(1)**, 88-102 (2021).

[170] Pugh, K. Jones, R.D.O., Powathil, G. & Hamis, S. Simulations probe the role of space in the interplay between drug-sensitive and drug-resistant cancer cells. *J Theor Biol* **602-603**, 112048 (2025).

[171] Eden, M. A two-dimensional growth process. *Proc.* 4^{th} *Berkeley Sympos Math Statist and Prob* **4**, 223-239 (1961).

[172] Waclaw, B., Bozic, I., Pittman, M.E., Hruban, R.H., Vogelstein, B. & Nowak, M.A. A spatial model predicts that dispersal and cell turnover limit intratumour heterogeneity. *Nature* **525(7568)**, 261-264 (2015).

[173] Lewinsohn, M.A., Bedford, T., Müller, N.F. & Feder, A.F. State-dependent evolutionary models reveal modes of solid tumour growth. *Nat Ecol Evol* **7(4)**, 581-596 (2023).

[174] Komarova, N.L. Spatial Stochastic Models for Cancer Initiation and Progression. *Bull Math Biol* **68(7)**, 1573-1599 (2006).

[175] Durrett, R. & Moseley, S. Spatial Moran models I. Stochastic tunneling in the neutral case. *Ann Appl Probab* **25(1)**, 104 (2015).

[176] Durrett, R., Foo, J. & Leder, K. Spatial Moran models, II: cancer initiation in spatially structured tissue. *J Math Biol* **72(5)**, 1369-1400 (2016).

[177] Noble, R. et al. Spatial structure governs the mode of tumour evolution. *Nat Ecol Evol* **6(2)**, 207-217 (2022).

[178] Mahdipour-Shirayeh, A., Kaveh, K., Kohandel, M. & Sivaloganathan, S. Phenotypic heterogeneity in modeling cancer evolution. *PLoS One* **12(10)**, e0187000 (2017).

[179] Kostiou, V., Hall, M.W., Jones, P.H. & Hall, B.A. Simulations reveal that different responses to cell crowding determine the expansion of p53 and Notch mutant clones in squamous epithelia. *J R Soc Interface* **18(183)**, 20210607 (2021).

[180] Chisholm, R.H. et al. Emergence of Drug Tolerance in Cancer Cell Populations: An Evolutionary Outcome of Selection, Nongenetic Instability, and Stress-Induced Adaptation. *Cancer Res* **75(6)**, 930-939 (2015).

[181] Murray, P.J., Edwards, C.M., Tindall, M.J., & Maini, P.K. Classifying general nonlinear force laws in cell-based models via the continuum limit. *Phys Rev E* **85(2)**, 021921 (2012).

[182] Dyson, L., Maini, P.K. & Baker, R.E. Macroscopic limits of individual-based models for motile cell populations with volume exclusion. *Phys Rev E* **86(3)**, 031903 (2012).

[183] Hillen, T., & Painter, K.J. A user's guide to PDE models for chemotaxis. *J Math Biol*, **58(1)**, 183-217 (2009).

[184] Stevens, A. The derivation of chemotaxis equations as limit dynamics of moderately interacting stochastic many-particle systems. *SIAP* **61(1)**, 183-212 (2000).

[185] Champagnat, N. & Méléard, S. Invasion and adaptive evolution for individual-based spatially structured populations. *J Math Biol* **55(2)**, 147-188 (2007).

[186] Johnston, S.T., Baker, R.E., McElwain, D.S. & Simpson, M.J. Co-operation, competition and crowding: a discrete framework linking Allee kinetics, nonlinear diffusion, shocks and sharp-fronted travelling waves. *Sci Rep* **7(1)**, 42134 (2017).

[187] Deroulers, C., Aubert, M., Badoual, M. & Grammaticos, B. Modeling tumor cell migration: from microscopic to macroscopic models. *Phys Rev E* **79(3)**, 031917 (2009).

[188] Buttenschoen, A., Hillen, T., Gerisch, A. & Painter, K.J. A space-jump derivation for non-local models of cell-cell adhesion and non-local chemotaxis. *J Math Biol* **76(1)**, 429–456 (2018).

[189] Byrne, H.M. & Drasdo, D. Individual-based and continuum models of growing cell populations: a comparison. *J Math Biol* **58(4)**, 657-687 (2009).

[190] Engblom, S., Wilson, D.B. & Baker, R.E. Scalable population-level modelling of biological cells incorporating mechanics and kinetics in continuous time. *R Soc Open Sci* **5(8)**, 180379 (2018).

[191] Cornell, S.J., Suprunenko, Y.F., Finkelshtein, D., Somervuo, P. & Ovaskainen, O. A unified framework for analysis of individual-based models in ecology and beyond. *Nat Commun* **1(1)0**, 4716 (2019).

[192] Motsch, S. & Peurichard, D. From short-range repulsion to Hele-Shaw problem in a model of tumor growth. *J Math Biol* **76(1)**, 205–234 (2018).

[193] Chaplain, M.A.J., Lorenzi, T. & Macfarlane, F.R. Bridging the gap between individual-based and continuum models of growing cell populations. *J Math Biol* **80(1)**, 343–371 (2020).

[194] Stéphanou, A. & Volpert, V. Hybrid Modelling in Biology: a Classification Review. *Math Model Nat Phenom* **11(1)**, 37-48 (2016).

[195] Anderson, A.R.A., Sleeman, B.D., Young, I.M. & Griffiths, B.S. Nematode movement along a chemical gradient in a structurally heterogeneous environment. 2. theory. *Fundam Appl Nematol* **20(2)**, 165-172 (1997).

[196] Anderson, A.R.A. & Chaplain, M.A.J. Continuous and discrete mathematical models of tumor-induced angiogenesis. *Bull Math Biol* **60(5)**, 857-899 (1998).

[197] Plank, M.J. & Sleeman, B.D. Lattice and non-lattice models of tumour angiogenesis. *Bull Math Biol* **66(6)**, 1785–1819 (2004).

[198] Powathil, G.G., Gordon, K.E., Hill, L.A. & Chaplain, M.A.J. Modelling the effects of cell-cycle heterogeneity on the response of a solid tumour to chemotherapy: biological insights from a hybrid multiscale cellular automaton model. *J Theor Biol* **308**, 1-19 (2012).

[199] Macnamara, C.K., Caiazzo, A., Ramis-Conde, I. & Chaplain, M.A.J. Computational modelling and simulation of cancer growth and migration within a 3D heterogeneous tissue: The effects of fibre and vascular structure. *J Comput Sci* **40**, 101067 (2020).

[200] Schaller, G. & Meyer-Hermann, M. Multicellular tumor spheroid in an off-lattice Voronoi-Delaunay cell model. *Phys Rev E Stat Nonlin Soft Matter Phys* **71(5)**, 051910 (2005).

[201] Alarcón, T., Byrne, H.M. & Maini, P.K. A cellular automaton model for tumour growth in inhomogeneous environment. *J Theor Biol* **225(2)**, 257-274 (2003).

[202] Jagiella, N., M'uller, B., M'uller, M., Vignon-Clementel, I.E. & Drasdo, D. Inferring Growth Control Mechanisms in Growing Multi-cellular Spheroids of NSCLC Cells from Spatial-Temporal Image Data. *PLoS Comput Biol* **12(2)**, e1004412 (2016).

[203] Grogan, J.A. et al. Predicting the influence of microvascular structure on tumor response to radiotherapy. *TBME* **64(3)**, 504-511 (2016).

[204] Hamis, S., Yates, J., Chaplain, M.A.J. & Powathil, G.G. Targeting Cellular DNA Damage Responses in Cancer: An In Vitro-Calibrated Agent-Based Model Simulating Monolayer and Spheroid Treatment Responses to ATR-Inhibiting Drugs. *Bull Math Biol* **83(10)**, 103 (2021).

[205] Oliver, S., Williams, M., Jolly, M.K., Gonzalez, D. & Powathil, G. Exploring the role of EMT in ovarian cancer progression using a multiscale mathematical model. *npj Syst Biol Appl* **11(1)**, 36 (2025).

[206] Bishop, R.T. et al. The bone ecosystem facilitates multiple myeloma relapse and the evolution of heterogeneous drug resistant disease. *Nat Commun* **15(1)**, 2458 (2024).

[207] Rejniak, K.A. & Anderson, A.R.A. Hybrid models of tumor growth. *WIREs Syst Biol Med* **3(1)**, 115-125 (2011).

[208] Lowengrub, J.S. et al. Nonlinear modelling of cancer: bridging the gap between cells and tumours. *Nonlinearity* **23(1)**, R1-R9 (2010).

[209] Roose, T., Chapman, S.J. & Maini, P.K. Mathematical Models of Avascular Tumor Growth. *SIREV* **49(2)**, 179-208 (2007).

[210] Shaffer, S.M. et al. Rare cell variability and drug-induced reprogramming as a mode of cancer drug resistance. *Nature* **546(7658)**, 431-435 (2017).

[211] França, G.S. et al. Cellular adaptation to cancer therapy along a resistance continuum. *Nature* **631(8022)**, 876-883 (2024).

[212] Song, Y. et al. Efficacy and Safety of Gefitinib as Third-line Treatment in NSCLC Patients With Activating EGFR Mutations Treated With First-line Gefitinib Followed by Second-line Chemotherapy: A Single-Arm, Prospective, Multicenter Phase II Study. *Am J Clin Oncol* **42(5)**, 432-439 (2019).

[213] Becker, A. et al. Retreatment with erlotinib: Regain of TKI sensitivity following a drug holiday for patients with NSCLC who initially responded to EGFR-TKI treatment. *Eur J Cancer* **47(17)**, 2603-2606 (2011).

[214] Maynard, R.L., Downes, N. & Finney, B. *Histological Techniques: An Introduction for Beginners in Toxicology* First edition (Royal Society of Chemistry, Cambridge, 2014).

[215] Miti, T., Desai, B., Miroshnychenko, D., Basanta, D. & Marusyk, A. Dissecting the spatially restricted effects of microenvironment-mediated resistance on targeted therapy responses. *Cancers* **16(13)**, 2405 (2024).

[216] Fisher, D.T. et al. Intraoperative intravital microscopy permits the study of human tumour vessels. *Nat Commun* **7(1)**, 10684 (2016).

[217] Robertson-Tessi, M., Gillies, R.J., Gatenby, R.A. & Anderson, A.R.A. Impact of metabolic heterogeneity on tumor growth, invasion, and treatment outcomes. *Cancer Res* **75(8)**, 1567-1579 (2015).

[218] Dewhirst, M. et al. Morphologic and hemodynamic comparison of tumor and healing normal tissue microvasculature. *Int J Radiat Oncol Biol Phys* **17(1)**, 91-99 (1989).

[219] Flaumenhaft, R. & Rifkin, D.B. The extracellular regulation of growth factor action. *Mol Biol Cell* **3(10)**, 1057-1065 (1992).

[220] Cilfone, N.A., Kirschner, D.E. & Linderman, J.J. Strategies for efficient numerical implementation of hybrid multi-scale agent-based models to describe biological systems. *Cel Mol Bioeng* **8(10**, 119-136 (2015).

[221] Süli, E. Numerical solution of partial differential equations. *Princeton Companion to Applied Mathematics*, Higham, N.J.. 306 - 319 (Princeton University Press, Princeton and Oxford, 2015).

[222] Madzvamuse, A. & Maini, P.K. Velocity-induced numerical solutions of reaction-diffusion systems on continuously growing domains. *J Comput Phys* **225(1)**, 100-119 (2007).

[223] Bravo, R.R. et al. Hybrid automata library: a flexible platform for hybrid modeling with real-time visualization. *PLoS Comput Biol* **16(3)**, e1007635 (2020).

[224] Damaghi, M. et al. The harsh microenvironment in early breast cancer selects for a Warburg phenotype. *Proc Natl Acad Sci U S A* **118(3)**, e2011342118 (2021).

[225] Masud M.A., Kim, J.Y. & Kim, E. Modeling the effect of acquired resistance on cancer therapy outcomes. *Comput Biol Med* **162**, 107035 (2023).

[226] Miroshnychenko, D. et al. Stroma-mediated breast cancer cell proliferation indirectly drives chemoresistance by accelerating tumor recovery between chemotherapy cycles. *Cancer Res* **83(22)**, 3681-3692 (2023).

[227] Strobl, M. et al. Spatial structure impacts adaptive therapy by shaping intra-tumoral competition. *Commun Med* **2(1)**, 46 (2022).

[228] West, J., Schenck, R.O., Gatenbee, C., Robertson-Tessi, M. & Anderson, A.R.A. Normal tissue architecture determines the evolutionary course of cancer. *Nat Commun* **12(1)**, 2060 (2021).

[229] Bartha, F. A., Juhász, N., Marzban, S., Han, R. & Röst, G. In silico evaluation of paxlovid's pharmacometrics for SARS-CoV-2: a multiscale approach. *Viruses* **14(5)**, 1103 (2022).

[230] Marzban, S., Han, R., Juhász, N. & Röst, G. A hybrid PDE-ABM model for viral dynamics with application to SARS-CoV-2 and influenza. *R Soc Open Sci* **8(11)**, 210787 (2021).

[231] Pruett, L.J., Taing, A.L., Singh, N.S., Peirce, S.M. & Griffin, D.R. Insilico optimization of heparin microislands in microporous annealed particle hydrogel for endothelial cell migration. *Acta Biomater* **148**, 171-180 (2022).

[232] Mantzaris, N.V., Webb, S. & Othmer, H.G. Mathematical modeling of tumor-induced angiogenesis. *J Math Biol* **49(2)**, 111-187 (2004).

[233] Melicow, M.M. The three steps to cancer: a new concept of cancerigenesis. *J Theor Biol* **94(2)**, 471-511 (1982).

[234] Alberts, B. et al. *Molecular biology of the cell.* Sixth edition (Garland science, New York, 2014).

[235] Calabresi, P., Schein, P.S. & Rosenberg, S.A. *Medical Oncology: Basic Principles and Clinical Management of Cancer* (MacMillan, New York, 1985).

[236] Misell, L.M., Hwang, E.S., Au, A., Esserman, L. & Hellerstein, M.K. Development of a novel method for measuring in vivo breast epithelial cell proliferation in humans. *Breast Cancer Res Treat* **89(3)**, 257-264 (2005).

[237] Bartzatt, R. *Horizons in Cancer Research Volume 60 Chapter 12 Pharmaceutical Properties and Drug Likeness of Anticancer Drugs Administered for the Clinical Treatment of Lung Cancer* (NOVA, New York, 2005).

[238] Erickson, H.P. Size and shape of protein molecules at the nanometer level determined by sedimentation, gel filtration, and electron microscopy. *Biol Proced Online* **11(1)**, 32 (2009).

[239] Pluen, A. et al. Role of tumor–host interactions in interstitial diffusion of macromolecules: cranial vs. subcutaneous tumors. *Proc Natl Acad Sci U S A* **98(8)**, 4628-4633 (2001).

[240] Toni, T., Welch, D., Strelkowa, N., Ipsen, A. & Stumpf, M.P. Approximate Bayesian computation scheme for parameter inference and model selection in dynamical systems. *J R Soc Interface* **6(31)**, 187-202 (2009).

[241] Sisson, S.A., Fan, Y., & Beaumont, M. *Handbook of approximate Bayesian computation* (Chapman & Hall/CRC, Florida, 2018).

[242] Beaumont, M.A. Approximate bayesian computation. *Annu Rev Stat Appl* **6(1)**, 379-403 (2019).

[243] Tavaré, S., Balding, D.J., Griffiths, R.C. & Donnelly, P. Inferring coalescence times from DNA sequence data. *Genetics* **145(2)**, 505-518 (1997).

[244] Pritchard, J.K., Seielstad, M.T., Perez-Lezaun, A. & Feldman, M.W. Population growth of human Y chromosomes: a study of Y chromosome microsatellites. *MBE* **16(12)**, 1791-1798 (1999).

[245] Beaumont, M.A., Zhang, W. & Balding, D.J. Approximate Bayesian computation in population genetics. *Genetics* **162(4)**, 2025-2035 (2002).

[246] Sunnåker, M., Busetto, A.G., Numminen, E., Corander, J., Foll, M. & Dessimoz, C. Approximate bayesian computation. *PLoS Comput Biol* **9(1)**, e1002803 (2013).

[247] Marjoram, P., Molitor, J., Plagnol, V., & Tavaré, S. Markov chain Monte Carlo without likelihoods. *PNAS* **100(26)**, 15324-15328 (2003).

[248] Sisson, S.A., Fan, Y. & Tanaka, M.M. Sequential monte carlo without likelihoods. *PNAS* **104(6)**, 1760-1765 (2007).

[249] Lambert, B., MacLean, A.L., Fletcher, A.G., Combes, A.N., Little, M.H. & Byrne, H.M. Bayesian inference of agent-based models: a tool for studying kidney branching morphogenesis. *J Math Biol* **76(7)**, 1673-1697 (2018).

[250] Kaznatcheev, A., Peacock, J., Basanta, D., Marusyk, A. & Scott, J.G. Fibroblasts and alectinib switch the evolutionary games played by non-small cell lung cancer. *Nat Ecol Evol* **3(3)**, 450-456 (2019).

[251] Czarnecka, A.M., Bartnik, E., Fiedorowicz, M. & Rutkowski, P. Targeted therapy in melanoma and mechanisms of resistance. *Int J Mol Sci* **21(13)**, 4576 (2020).

[252] Yanagisawa, N. et al. Stromogenic prostatic carcinoma pattern (carcinomas with reactive grade 3) in needle biopsies predicts biochemical recurrence-free survival in patients after radical prostatectomy. *Hum Pathol* **38(11)**, 1611-1620 (2007).

[253] Mesker, W.E. et al. The carcinoma-stromal ratio of colon carcinoma is an independent factor for survival compared to lymph node status and tumor stage. *Anal Cell Pathol* **29(5)**, 387-398 (2007).

[254] Smalley, I. et al. Leveraging transcriptional dynamics to improve BRAF inhibitor responses in melanoma. *EBioMedicine* **48**, 178-190 (2019).

[255] He, J., Qiu, Z., Fan, J., Xie, X., Sheng, Q. & Sui, X. Drug tolerant persister cell plasticity in cancer: A revolutionary strategy for more effective anticancer therapies. *Sig Transduct Target Ther* **9(1)**, 209 (2024).

[256] Russo, M. et al. Cancer drug-tolerant persister cells: from biological questions to clinical opportunities. *Nat Rev Cancer* **24(10)**, 694-717 (2024).

[257] Fallahi-Sichani, M. et al. Adaptive resistance of melanoma cells to RAF inhibition via reversible induction of a slowly dividing de-differentiated state. *Mol Syst Biol* **13(1)**, 905 (2017).

[258] Milo, R., Jorgensen, P., Moran, U., Weber, G. & Springer, M. BioNumbers—the database of key numbers in molecular and cell biology. *Nucleic Acids Res* **38(1)**, D750-D753 (2010).

[259] West, J. et al. A survey of open questions in adaptive therapy: Bridging mathematics and clinical translation. *Elife* **12**, e84263 (2023).

[260] Folkman, J. What is the evidence that tumors are angiogensis dependent?. *JNCI* **82(1)**, 4-7 (1990).

[261] Gasparini, G., Longo, R., Toi, M., & Ferrara, N. Angiogenic inhibitors: a new therapeutic strategy in oncology. *Nat Rev Clin Oncol* **2(11)**, 562-577 (2005).

[262] Tzedakis, G., Tzamali, E., Marias, K. & Sakkalis, V. The importance of neighborhood scheme selection in agent-based tumor growth modeling. *Cancer Inform* **14**, CIN.S19343 (2015).

[263] Voelkl, B. et al. Reproducibility of animal research in light of biological variation. *Nat Rev Neurosci* **21(7)**, 384-393 (2020).

[264] von Kortzfleisch, V.T. et al. Improving reproducibility in animal research by splitting the study population into several 'mini-experiments'. *Sci Rep* **10(1)**, 16579 (2020).

[265] Kilkenny, C., Browne, W., Cuthill, I.C., Emerson, M. & Altman, D.G. Animal research: reporting in vivo experiments: the ARRIVE guidelines. *Br J Pharmacol* **160(7)**, 1577-1579 (2010).

[266] Percie du Sert, N. et al. The ARRIVE guidelines 2.0: Updated guidelines for reporting animal research. *PLoS Biol* **18(7)**, e3000410 (2020).

[267] Smith, A.J., Clutton, R.E., Lilley, E., Hansen, K.E.A. & Brattelid, T. PREPARE: guidelines for planning animal research and testing. *Lab Anim* **52(2)**, 135-141 (2017).

Appendix A

Exploration of Mechanisms of Activation and Deactivation Dynamics for Cancer Associated Fibroblasts

Alternative hypotheses to the activation and deactivation mechanisms assumed in the model are considered.

Stromal activation hypotheses:

A1) Contact-mediated activation: crosstalk is limited to the tumour-stroma interface (chosen mechanism for the main model).

A2) Non-contact mediated activation: crosstalk acts on a larger range i.e. not limited to interactions in the Moore Neighbourhood.

Stromal deactivation hypotheses:

D1) Active stroma cells deactivate upon loss of condition for activation, i.e. drug concentration falling below h_r (chosen mechanism for the main model).

D2) Active stroma undergoes stochastic death with probability p_T, i.e. active stroma is subject to turnover. Here the reactive stroma acts in a wound healing, immune response fashion, intervening to rescue the cancer under drug treatment, and dying after fulfilling this role.

With four models we investigate combinations of the hypotheses stated above. We compare the main model M1 (A1, D1) with the three additional models emerging from other combinations of activations and deactivation hypotheses: M2 (A1,D2), M3 (A2,D2), and M4 (A2,D1).

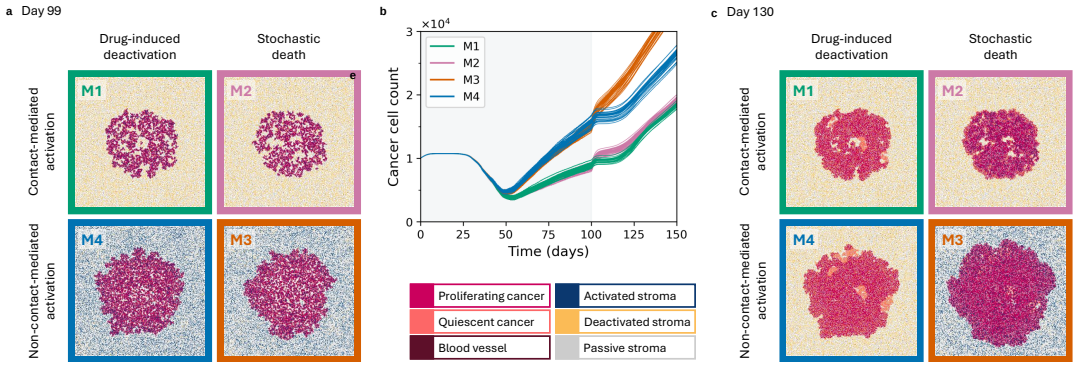

Figure A.1: Comparison of different types of activation and deactivation mechanisms for CAFs. Models M1 (A1,D1), M2 (A1,D2), M3 (A2,D2), and M4 (A2,D1) are considered over 150 days with treatment regime $\tau_T = 100$ days and $\tau_H = 50$ days. **a:** Spatial distributions for a single simulation of each model at day 99, just prior to the end of treatment. **b:** Tumour burden for $t \in [0, 150]$ days. Individual realisations are shown, with 30 stochastic simulations conducted for each model. **c:** Spatial distributions for a single simulation of each model at day 130, after the treatment has stopped.

We first compare the effects of different activation mechanisms on tumour dynamics under treatment. Non-contact-mediated activation (A2) results in greater tumour burden (Fig. A.1**b**), over 100 days of treatment. Stromal activation across the whole domain results in cancer cells proliferating into activated regions having a greater chance of survival from the paracrine assistance. Conversely, contact-mediated activation (A1) limits paracrine assistance, hence survival, to the tumour periphery. This results in reduced and less densely packed growth (Fig. A.1**a**). While different deactivation

mechanisms considered do not have a significant effect on the treatment period, there is a clear separation of dynamics when treatment is stopped (Fig. A.1**b**). Stochastic death (D2) operates independently of the dynamics of drug leaving the tissue and stromal deactivation takes much longer. The residual activated stroma continue to provide paracrine assistance further into the drug holiday period (Fig. A.1**c**), enhancing the tumour regrowth. Regrowth is further augmented with on-contact-mediated activation (A2), compared to contact-mediated activation (A1). This is due to cancer cells proliferating into 'primed' regions of activated stroma outside of the tumour boundary, receiving additional paracrine assistance.

Appendix B

Cancer Cell Motility

The cells in our model that we describe in Chapter 4 do not move. While this simplifying assumption improves model efficiency and reduces the complexity of our spatial analysis, it is not realistic because cancer cells are motile, resulting in invasion and metastasis. We extend our model by introducing cancer cell motility. Since we are interested how cancer cell motility affects the formation of residual disease and including cell motility significantly increases the complexity of the model implementation, we do not allow stroma cells to move.

We introduce $m(\mathbf{x}, t)$ as tumour cell density. Cancer cell movement resembles an unbiased random walk; hence, we assume a flux of $J = -D_m \nabla m$. This together with the conservation of tumour cell density equation allows us to determine the following PDE that governs cancer cell motility:

$$\frac{\partial m}{\partial t} = \overbrace{D_m \nabla^2 m(\mathbf{x}, t)}^{\text{random motility}}, \tag{B.1}$$

where D_m is the motility coefficient.

For the discretization of Equation B.1 we use the well-established technique introduced by Anderson *et al.* [195] and extend the direction of movement to the Moore neighbourhood as presented by Tzedakis *et al.* [262].

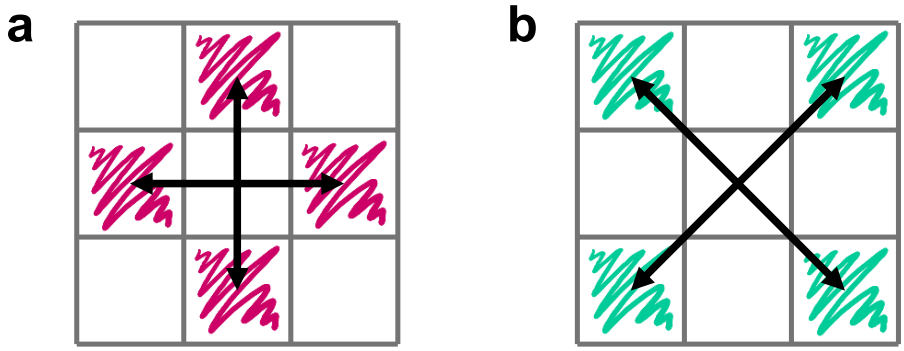

Figure B.1: Construction of Moore neighbourhood. a: The first von Neumann neighbourhood $\mathcal{H}^v$. **b:** The rotated von Neumann neighbourhood $\mathcal{H}^{\bar{v}}$.

To determine the direction of movement of a cancer cell during the movement phase we derive the set of probabilities of a cell to pick a position in the Moore neighbourhood, from the discretisation of the continuous PDE Equation B.1. We construct a Moore neighbourhood from two von Neumann neighbourhoods, the first being the von Neumann neighbourhood of the cell, denoted by $\mathcal{H}^v$. The second is a rotated von Neumann neighbourhood aligned with the diagonals of the Moore neighbourhood, denoted by $\mathcal{H}^{\bar{v}}$ (Fig. B.1). A parameter a is introduced as the probability that cell movement will occur in the first von Neumann neighbourhood. We use $a\mathcal{H}^v + (1-a)\mathcal{H}^{\bar{v}} = 1$ to write our FTCS numerical scheme from Equation B.1. We get:

$$m_{i,j}{}^{q+1} = P_0 m_{i,j}{}^q + \left[aP_v\mathcal{H}^v + (1-a)P_{\bar{v}}\mathcal{H}^{\bar{v}}\right], \tag{B.2}$$

where:

$$\mathcal{H}^v = m_{i-1,j}{}^q + m_{i,j-1}{}^q + m_{i+1,j}{}^q + m_{i,j+1}{}^q, \tag{B.3}$$

and:

$$\mathcal{H}^{\bar{v}} = {m_{i-1,j+1}}^q + {m_{i-1,j-1}}^q + {m_{i+1,j-1}}^q + {m_{i+1,j+1}}^q. \tag{B.4}$$

The coefficients P_0, P_v and $P_{\bar{v}}$ are taken to be proportional to the probabilities of the direction of cancer cell movement. The probability that a cancer cell remains stationary is complementary to the probability that a cancer cell will move; hence we can write $P_0 = 1 - 4\left[aP_v + (1-a)P_{\bar{v}}\right]$. We have P_v and $P_{\bar{v}}$ as follows:

$$P_v = \frac{\Delta t D_d}{(\Delta x)^2}, \tag{B.5}$$

and:

$$P_{\bar{v}} = \frac{\Delta t D_d}{2(\Delta x)^2}. \tag{B.6}$$

To ensure the stability of this explicit numerical scheme we need to impose a constraint on Δt. Since $P_0 \geq 0$ we can write:

$$1 - 4\left[aP_v + (1-a)P_{\bar{v}}\right] \geq 0, \tag{B.7}$$

which, with the substitution of Equation B.5 and Equation B.6 and some manipulation, we can write as:

$$\Delta t \leq \frac{(\Delta x)^2}{2(a+1)D_m}. \tag{B.8}$$

For our parameter values (Tables 5.1 - 5.3), $D_m = 10^{-9}$ cm^2 day^{-1}, and $a = \frac{2}{3}$ computational efficiency is significantly reduced (becoming impractical) and the complexity of spatial analysis of residual disease increased. Given that, in our small *in-silco* study, we observe similar patterns of EMDR mediated residual disease at tissue level as the case where we neglect cancer cell motility (Fig. B.2**b** and Fig. 6.4**b**), we argue that it is appropriate to not allow cancer cell movement for the purposes of our analysis.

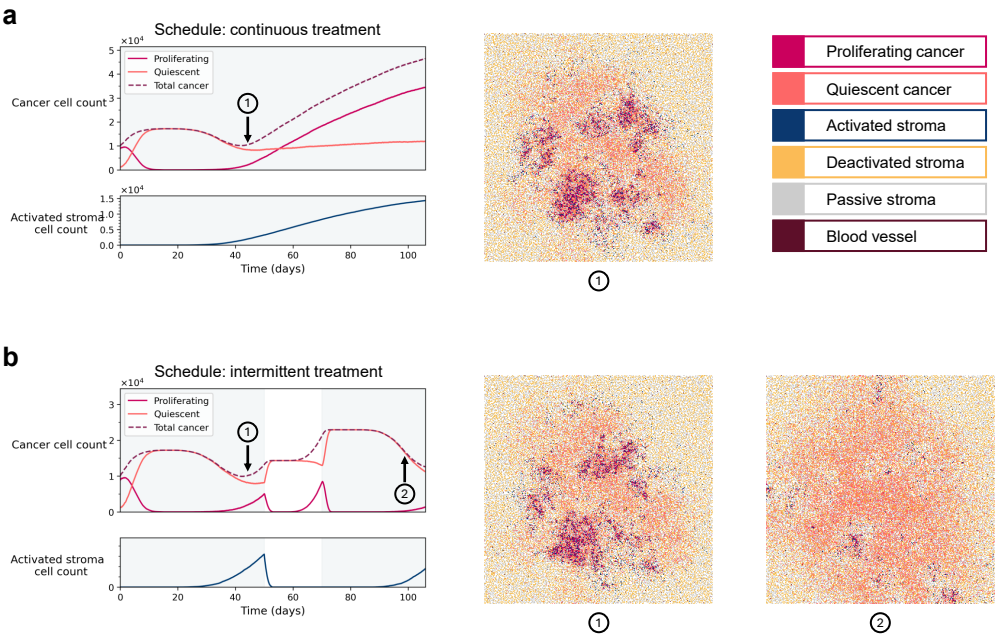

Figure B.2: Including cancer cell motility. **a:** Timecourse of a single representative simulation of continuous treatment over 105 days showing cancer cell populations and activated stroma populations. Spatial distribution of cells at day 44. **b:** Timecourse of a single representative simulation of intermittent treatment regime ($\tau_T = 50$ days, $\tau_H = 20$ days) over 105 days showing cancer cell populations and activated stroma populations. Spatial distribution of cells at days 44 and 99. While there is overall more residual disease which is more dispersed in Ω, the regions where residual disease is driven by EMDR correspond to the same regions as those in the model without cancer cell motility (Fig. 6.4**b**). Results are with parameter values $p_0 = 0.21$, $\beta = 0.59$ day^{-1}, $\gamma = 2.44$ day^{-1} cell^{-1} and $\delta = 3.17$ day^{-1}. Other parameter values are listed in Tables 5.1 - 5.3.

Appendix C

Further Details of *In-vivo* Experimental Setup

Cell line

EML4-ALK+ H3122 NSCLC cell line were obtained from the Lung Cancer Center of Excellence Cell Line depository at the H. Lee Moffitt Cancer Center. A STR repeats based test was used to authenticate cell lines. For each experiment, a separate frozen vial from an early passage was expanded to generate sufficient numbers of cells for injections and tested for mycoplasma contamination.

Xenograft tumour model

Xenograft studies were performed by subcutaneous bilateral implantation of 5E6 tumour cells/injection suspended 100 μl of 1 : 1 RPMI / BME type 3 (R&D Systems $\#36 - 320 - 1002P$) into 4 to 6 week-old NOD-scid IL2Rgnull (NSG) mice of both sexes. The animals were produced at the institute with breeders purchased from Jackson Laboratory. Treatment was initialized 3 weeks post implantation, at which point the tumour diameter reached $3 - 4$ mm. Pharmacological grade Alectinib was dissolved in water and administered via daily oral gavage (7 dats week^{-1}) at 25 mg kg^{-1} in 100 μl volume. Tumour

growth was monitored by weekly electronic caliper measurements. Tumour volumes were calculated assuming spherical shape. All the xenograft studies were performed as per the approved procedures of IACUC protocol $\#IS00005557$ of the H. Lee Moffitt Cancer Center. Animals were maintained under AAALAC-accredited specific pathogen-free housing vivarium and veterinary supervision following standard guidelines for temperature and humidity, with a 12-hour light / 12-hour dark cycle. Tumour diameter measurements were maintained under the maximal tumour diameter measurement (20 mm) permitted by the IACUC of the H. Lee Mofitt Cancer Center. We have complied with all relevant ethical regulations for animal use.

Appendix D

Exploring the Heterogeneity of Xenograft Models

It is expected that there is variation in results when using xenograft models within and across experiments [263, 264]. Using individual live animals introduces heterogeneity, while factors such as environmental conditions, experimental design and choice of equipment account also account for variability. Additionally, the individual experimentalist is innately unreliable and perhaps contributes significantly to variation within and across experiments. Despite guidelines being developed that address these issues and their impacts on experimental reproducibility, variability remains to be a problem [264, 265, 266, 267].

The *in-vivo* experimental data we use to calibrate our model consists of two cohorts (vehicle control and drug treated) of five xenografts, each with subcutaneous tumours injected into their left and right flanks. Although the guidelines and procedures designed to reduce variability were followed, there is considerable variability in the data, including between the left and right tumours in the same xenograft and some tumours that reduce in size (Fig. D.1**a** for the vehicle control cohort). We could not reliably calibrate our model using ABC to all the replicates at the same time as we were unable to infer reasonable marginal posterior distributions for p_0 and β for one chosen value of ϵ (Fig.

D.1**b**).

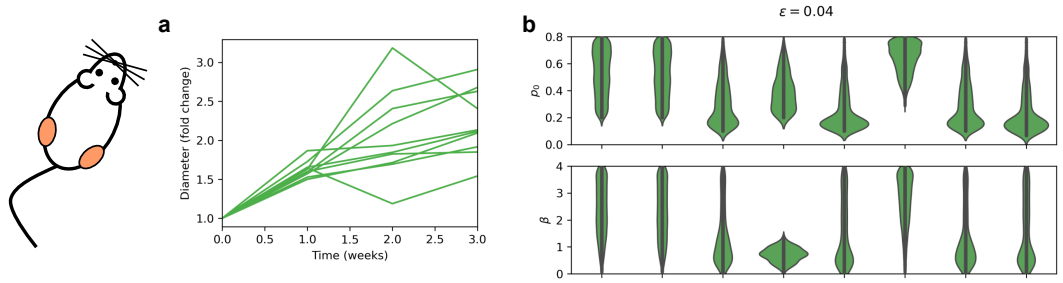

Figure D.1: Xenograft replicate data. a: Tumour diameter fold change over the 3 week *in-vivo* experiment for the vehicle control cohort. There is reasonable variation between the tumour diameter fold change measurements, particularly in the measurements for weeks 2 and 3. Additionally, for specific replicates tumour diameter fold change measurements reduce in size, inconsistent with the experimental set up. **b:** Marginal posterior distributions for p_0 and β obtained by ABC with $N = 10^4$ and $\epsilon = 0.04$ for individual replicates (here $n = 8$ as no posterior was able to be inferred for the threshold value chosen for two of the replicates).

Calibrating our model to individual replicates required us to use a different threshold (some of very different order) each time we implemented the ABC model. In Figure D.2 we show for six chosen replicates, the diameter fold change time series for *in-vivo* experimental data for the vehicle control replicates (*black* line) compared to the *in-silico* tumours (***green*** time series for parameter regimes corresponding to the (p_0, β) posterior distribution and the corresponding joint and marginal posterior distributions for p_0 and β obtained by ABC. The position of the joint posterior distributions varies in the prior distribution space, indicating there could be multiple choices of p_0 and β that produce *in-silco* model outputs consistent with *in-vivo* experimental results.

As an alternative we consider calibrating our model with an individual replicate rather than with the average across replicates that we use for our main parameter calibration. We choose the replicate whose posterior is most different to the posterior based on the average of the replicates (Fig. D.1**b**). The point estimates we choose are $p_0 = 0.29$ and $\beta = 2.8$. This value of β is much higher than the value chosen for the main results in the thesis. These point estimates are then used to calibrate parameter δ following the same processes described in Section 5.3.4.

We choose $\delta = 15$ as our point estimate and use this together with our chosen point estimate for β to choose an appropriate γ using the method described in Section 5.3.5. Here we choose $\gamma = 9.21$.

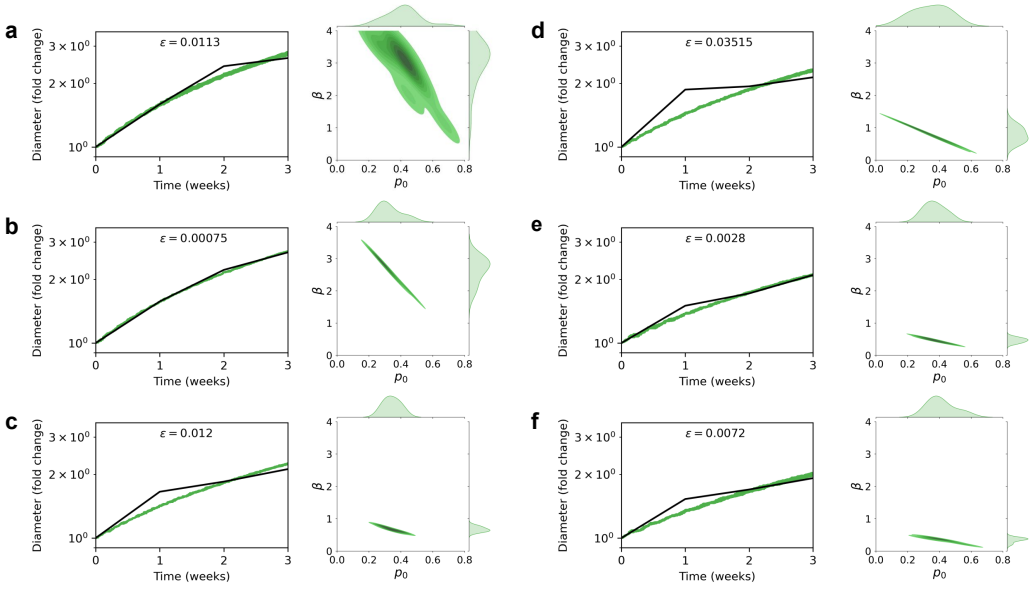

Figure D.2: Calibration with individual xenograft replicates. For six chosen replicates (**a - f**) the diameter fold change for *in-vivo* experimental data for chosen vehicle control replicate (***black***) time series and *in-silico* tumours (***green***) time series (right) for parameter regimes corresponding to the (p_0, β) joint and marginal posterior distributions shown (left). The joint and marginal posterior distributions for p_0 and β are obtained by ABC with $N = 10^4$ for different acceptance thresholds; **a:** $\epsilon = 0.0113$; **b:** $\epsilon = 0.00075$; **c:** $\epsilon = 0.012$; **d:** $\epsilon = 0.03515$; **e:** $\epsilon = 0.0028$; and **f:** $\epsilon = 0.0072$.

With these parameter values we investigate the treatment schedule landscape and find that qualitatively, the results do not differ between the high β regime compared to the low β regime presented in the main part of the thesis (Fig. D.3). These qualitatively consistent results across parameter values indicates to the robustness of our model. It is interesting to note that the residual disease in the high β regime is lower than in the low β regime. While these results are counterintuitive, given the higher autocrine signalling provided by the cancer cells, the much higher δ required to overcome this results in faster timescale of cancer death in relation to stromal activation and results in reduced residual

disease.

Given the relatively large space of acceptable parameter choices for p_0 and β (Fig. D.2), and the results of this exploration of xenograft heterogeneity (Fig. D.3), we argue our choice of using an average of the xenograft replicates to calibrate our model is appropriate.

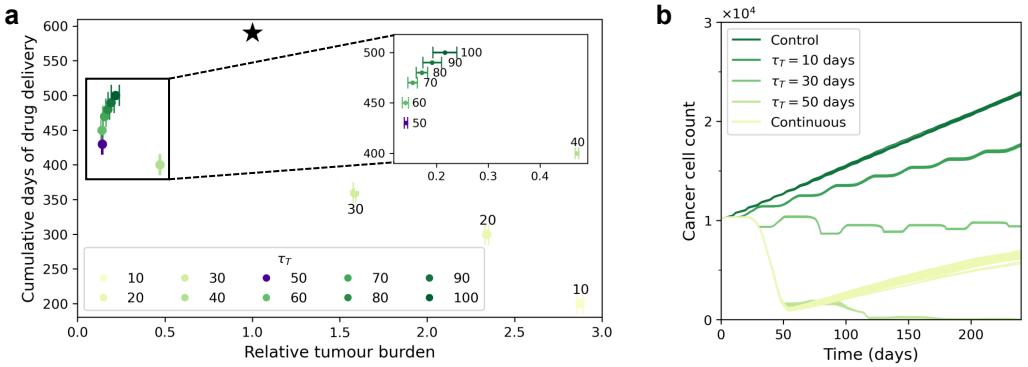

Figure D.3: Intermittent treatment regime analysis for parameter choice $p_0 = 0.29$, $\beta = 2.8$, $\delta = 15$ and $\gamma = 9.21$. a: Cumulative days of drug delivery (measured as the sum of drug delivery days over 590 days of therapy) against relative tumour burden (measured as the sum of total cancer cell count over the $t \in [0, 590]$ day window normalised to the continuous treatment case) for $\tau_T = \{10, 20, 30, 40, 50, 60, 70, 80, 90, 100\}$ days for $\tau_H = 20$ days. Results show the average of 30 simulations of each schedule and includes 95% confidence intervals. The star indicates measures for continuous treatment. Relative tumour burden initially decreases as cumulative days of drug delivery increases, but from $\tau_T = 50$ days the relative tumour burden increases. **b:** Tumour burden for $t \in [0, 240]$ days under no treatment, continuous treatment, and three intermittent treatment schedules ($\tau_T = \{10, 30, 50\}$ days and $\tau_H = 20$ days). Individual realisations are shown, with 30 stochastic simulations conducted for both untreated and treated conditions. As the length of the treatment period τ_T of intermittent treatment increases a reduction in tumour burden is observed.

Appendix E

Animations

The following animations can be viewed at **this link**:

- No treatment.
- Continuous treatment.
- Intermittent treatment regime with $\tau_T = 10$ days, $\tau_H = 20$ days.
- Intermittent treatment regime with $\tau_T = 20$ days, $\tau_H = 20$ days.
- Intermittent treatment regime with $\tau_T = 30$ days, $\tau_H = 20$ days.
- Intermittent treatment regime with $\tau_T = 40$ days, $\tau_H = 20$ days.
- Intermittent treatment regime with $\tau_T = 50$ days, $\tau_H = 20$ days.
- Intermittent treatment regime with $\tau_T = 60$ days, $\tau_H = 20$ days.
- Intermittent treatment regime with $\tau_T = 70$ days, $\tau_H = 20$ days.
- Intermittent treatment regime with $\tau_T = 80$ days, $\tau_H = 20$ days.
- Intermittent treatment regime with $\tau_T = 90$ days, $\tau_H = 20$ days.
- Intermittent treatment regime with regime $\tau_T = 100$ days, $\tau_H = 20$ days.
- *proliferation signal* and drug concentrations for survival and eradication niches for intermittent treatment regime with $\tau_T = 50$ days, $\tau_H = 20$ days.

The following animations can be viewed at **this link**:

- Phenotypic landscape no treatment.
- Phenotypic landscape continuous treatment.
- Phenotypic landscape intermittent treatment regime with $\tau_T = 30$ days, $\tau_H = 10$ days.
- Phenotypic landscape intermittent treatment regime with $\tau_T = 30$ days, $\tau_H = 20$ days.
- Phenotypic landscape intermittent treatment regime with $\tau_T = 30$ days, $\tau_H = 30$ days.
- Phenotypic landscape intermittent treatment regime with $\tau_T = 50$ days, $\tau_H = 10$ days.
- Phenotypic landscape intermittent treatment regime with $\tau_T = 50$ days, $\tau_H = 20$ days.
- Phenotypic landscape intermittent treatment regime with $\tau_T = 50$ days, $\tau_H = 20$ days.
- Phenotypic landscape intermittent treatment regime with $\tau_T = 70$ days, $\tau_H = 10$ days.
- Phenotypic landscape intermittent treatment regime with $\tau_T = 70$ days, $\tau_H = 20$ days.
- Phenotypic landscape intermittent treatment regime with $\tau_T = 70$ days, $\tau_H = 30$ days.
- Phenotypic landscape with abrupt drug diffusion dynamics intermittent treatment regime with $\tau_T = 50$ days, $\tau_H = 20$ days.

Appendix F

Restrictions on Δr

Equation 8.6 has at least one positive real solution if the discriminant is non-negative. We have:

$$0 \leq (\hat{h_d} + \hat{h_p} + C_{min}(\Delta r - 2))^2 - 4(1 - C_{min})(\hat{h_d}\hat{h_p} + C_{min}(\Delta r - 1)). \quad \text{(F.1)}$$

With a bit of manipulation, we can write Equation F.1 as a polynomial equation of degree two in Δr as follows:

$$0 \leq a\Delta r^2 + b\Delta r + c, \quad \text{(F.2)}$$

where:

$$a = {C_{min}}^2, \quad \text{(F.3)}$$
$$b = 2C_{min}(\hat{h_d} + \hat{h_p} - 2), \quad \text{(F.4)}$$
$$c = 4C_{min}(1 + \hat{h_d}\hat{h_p} - (\hat{h_d} + \hat{h_p})) + (\hat{h_d} - \hat{h_p})^2. \quad \text{(F.5)}$$

Calculating the discriminant explicitly gives:

$$b^2 - 4ac = 16{C_{min}}^2(1 - C_{min})(1 - h_d)(1 - h_p). \tag{F.6}$$

Since $C_{min} < 1$ and $h_d, h_p \in [0, 1]$, we have that the discriminant $b^2 - 4ac > 0$, ensuring the existence of two distinct real solutions for parameter Δr. Finally, given that $a > 0$, we have the following restrictions on the value of parameter Δr:

$$\Delta r \leq \frac{-b - \sqrt{b^2 - 4ac}}{2a}, \text{ and } \Delta r \geq \frac{-b + \sqrt{b^2 - 4ac}}{2a}. \tag{F.7}$$